SPRINGER BRIEFS IN APPLIED SCIENCES AND TECHNOLOGY · NANOTHERANOSTICS

Sophie Laurent · Céline Henoumont
Dimitri Stanicki · Sébastien Boutry
Estelle Lipani · Sarah Belaid
Robert N. Muller · Luce Vander Elst

MRI Contrast Agents
From Molecules to Particles

Springer

SpringerBriefs in Applied Sciences and Technology

Nanotheranostics

More information about this series at http://www.springer.com/series/13040

Sophie Laurent · Céline Henoumont
Dimitri Stanicki · Sébastien Boutry
Estelle Lipani · Sarah Belaid
Robert N. Muller · Luce Vander Elst

MRI Contrast Agents

From Molecules to Particles

Springer

Sophie Laurent
General, Organic and Biomedical Chemistry
NMR and Molecular Imaging Laboratory
University of Mons
Mons
Belgium

and

Center for Microscopy and Molecular Imaging (CMMI)
Gosselies
Belgium

Céline Henoumont
General, Organic and Biomedical Chemistry
NMR and Molecular Imaging Laboratory
University of Mons
Mons
Belgium

Dimitri Stanicki
General, Organic and Biomedical Chemistry
NMR and Molecular Imaging Laboratory
University of Mons
Mons
Belgium

Sébastien Boutry
Center for Microscopy and Molecular Imaging (CMMI)
Gosselies
Belgium

Estelle Lipani
General, Organic and Biomedical Chemistry
NMR and Molecular Imaging Laboratory
University of Mons
Mons
Belgium

Sarah Belaid
General, Organic and Biomedical Chemistry
NMR and Molecular Imaging Laboratory
University of Mons
Mons
Belgium

Robert N. Muller
General, Organic and Biomedical Chemistry
NMR and Molecular Imaging Laboratory
University of Mons
Mons
Belgium

and

Center for Microscopy and Molecular Imaging (CMMI)
Gosselies
Belgium

Luce Vander Elst
General, Organic and Biomedical Chemistry
NMR and Molecular Imaging Laboratory
University of Mons
Mons
Belgium

and

Center for Microscopy and Molecular Imaging (CMMI)
Gosselies
Belgium

ISSN 2191-530X ISSN 2191-5318 (electronic)
SpringerBriefs in Applied Sciences and Technology
ISSN 2197-6740 ISSN 2197-6759 (electronic)
Nanotheranostics
ISBN 978-981-10-2527-3 ISBN 978-981-10-2529-7 (eBook)
DOI 10.1007/978-981-10-2529-7

Library of Congress Control Number: 2016954704

Printed on acid-free paper

This Springer imprint is published by Springer Nature
The registered company is Springer Nature Singapore Pte Ltd.
The registered company address is: 152 Beach Road, #22-06/08 Gateway East, Singapore 189721, Singapore

Contents

Chapter 1
Interest of Nanomaterials in Medicine

Abstract This introduction highlights the importance of nanomaterials in biomedical applications. The use of different nanosystems in the medical field has conducted researchers to develop numerous synthetic ways.

Since few decades, nanotechnology is a growing interesting area of research. Fabrications of nanomaterials such as nanoparticles, clusters, nanotubes, nanowires or nanorods are the main domains investigated in nanotechnology. In October 2011, the European Commission officially defined the term "nanomaterial" as followed: "A natural, incidental or manufactured material containing particles, in an unbound state or as an aggregate or as an agglomerate and where, for 50 % or more of the particles in the number size distribution, one or more external dimensions is in the size range 1–100 nm" [1].

As the size decreases to nanoscale, nanomaterials exhibit extraordinary physical and chemical properties different from the bulk species, which can be attributed to their dimensional anisotropy and size. An important aspect is the increased ratio of surface area to volume, making possible new quantum mechanical effects where the electronic properties of solids are altered. In addition, their optical properties, such as fluorescence, depend on the particle diameter. For example, ZnO nanowires show nonlinear optical properties while the bulk ZnO shows linear optical properties [2] or Au nanorods can be used for optothermal therapy [3] while Au nanocages can be used for controlled release of drugs [4]. These excellent properties provide potential advantages in a wide range of applications including magnetic nanoparticles or multicolor optical coding based lab-on-chip technology [5, 6], visualization of cellular structures or tracking movements [7], controlled drug delivery, medical imaging technology.

Nanotechnology plays an important role in both medical research and clinical diagnostics/therapy, as nanomaterials are commonly within the same size scale than biological entities like cells, DNA and proteins. Properties of nanomaterials, including size, shape, chemical composition, surface structure and potential, aggregation and agglomeration, and solubility, can greatly influence their interactions with biomolecules and cells. For example, quantum dots (QDs) with

S. Laurent et al., *MRI Contrast Agents*, Nanotheranostics,
DOI 10.1007/978-981-10-2529-7_1

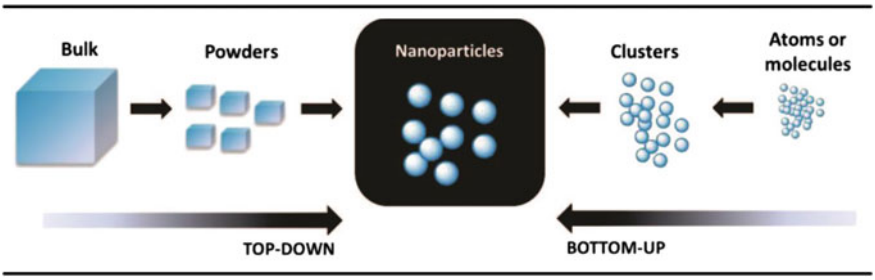

Fig. 1.1 Scheme of top-down and bottom-up approaches of the nanoparticle fabrication

size-tunable fluorescence emission have been employed to produce predominant images of tumor sites [8], or single-walled carbon nanotubes (SWCNTs) with diameters comparable to that of DNA show an impressive potential as high-efficiency delivery transporters for biomolecules into cells [9].

The discovery of the novel properties at the nanoscale has led to a great fascination for the nanoparticle fabrication. The manufacturing of the nanoparticles can be roughly categorized as either "top-down" or "bottom-up" approaches as depicted in Fig. 1.1. Top-down strategy refers to nanofabrication techniques consisting in the reduction of the size from bulk materials towards a nanometer size structure. The traditional methods of nanofabrication are principally gathered in the different methods of lithography [10–12]. This approach creates nanostructures with the expected shape and size with a high reproducibility. However, such processing is expensive and the lithography of nanostructures below 10 nm is often limited. In nanoparticle synthesis domain, researchers prefer the second approach "bottom-up" that provides a simple and powerful way to form colloidal suspensions. Contrarily to the top-down method, this approach is able to produce nanoparticles with dimensions below 10 nm. The synthesis process is not expensive. This process begins from the assembling of atoms or molecules to produce bigger entities. Many properties of nanomaterials can be controlled as the size, the surface or the shape which confer them a great interest in the organic/inorganic synthesis field [13].

References

1. http://www.afsca.be/laboratories/labinfo/_documents/2014-02_labinfo11_en.pdf
2. Johnson JC, Yan H, Schaller RD et al (2002) Near-field imaging of non-linear optical mixing in single zinc oxide nanowires. Nano Lett 2:279–283
3. Yi DK (2011) A study of optothermal and cytotoxic properties of silica coated Au nanorods. Mater Lett 65:2319–2321
4. Yavuz MS, Cheng Y, Chen J et al (2009) Nanocages covered by smart polymers for controlled release with near-infrared light. Nat Mater 8:935–939

5. Funcrand R, Bancaud A, Escriba C et al (2011) Development of a flexible microfluidic system integrating magnetic micro-actuators for trapping biological species. Sens Actuators B Chem 160:1520–1528
6. Dongre C, van Weerd J, Besselink GAJ et al (2011) Modulation-frequency encoded multi-color fluorescent DNA analysis in an optofluidic chip. Lab Chip 11:679–683
7. Imura K, Okamoto H, Hossain MK et al (2006) Visualization of localized intense optical fields in single gold-nanoparticle assemblies and ultrasensitive Raman active sites. Nano Lett 6:2173–2176
8. Cai W, Shin DW, Chen K et al (2006) Peptide-labeled near-infrared quantum dots for imaging tumor vasculature in living subjects. Nano Lett 6:669–676
9. Kam NWS, O'Connell M, Wisdom JA, Dai H (2005) Carbon nanotubes as multifunctional biological transporters and near-infrared agents for selective cancer cell destruction. Proc Nat Acad Sci USA 102:11600–11605
10. Baek Y-K, Yoo SM, Kang T et al (2010) Large-scale highly ordered chitosan-core Au-shell nanopatterns with plasmonic tunability: a top-down approach to fabricate core–shell nanostructures. Adv Funct Mater 20(24):4273–4278
11. Rolland JP, Maynor BW, Euliss LE et al (2005) Direct fabrication and harvesting of monodisperse, shape-specific nanobiomaterials. J Am Chem Soc 127(28):10096–10100
12. Hulteen JC, Treichel DA, Smith MT et al (1999) Nanosphere lithography: size-tunable silver nanoparticle and surface cluster arrays. J Phys Chem B 103(19):3854–3863
13. Jeong U, Wang Y, Ibisate M, Xia Y (2005) Some new developments in the synthesis, functionalization, and utilization of monodisperse colloidal spheres. Adv Funct Mater 15 (12):1907–1921

Chapter 2
Magnetic Properties

Abstract The magnetic properties of a material are the basis of their applications. Specifically, the contrast agents that will be developed in Chaps. 4 and 5 use their magnetic properties to play their role in magnetic resonance imaging. It is thus important to describe briefly the different magnetisms.

The magnetic properties of a material are characterized by its magnetic susceptibility χ, which describes the ability of the material or substance to be magnetized by an external magnetic field H.

$$M = \chi H$$

The magnetization, M, represents the net magnetic moment per unit volume that is aligned parallel to the external magnetic field. The magnetism of the material comes from either electrons (electronic magnetism) or atomic nuclei (nuclear magnetism). However, the magnetization created by one electron being 657 higher than that created by one proton, electronic magnetism masks the nuclear one. According to the behavior exhibited in the presence of a magnetic field, several classes of substances can be distinguished.

2.1 Diamagnetic Substances

The majority of atoms constituting tissues of the body are diamagnetic because they do not have unpaired electrons. The global electronic magnetic moment of each atom is zero. However, an external magnetic field Bo may slightly alter the orbital paths of the electrons in motion and low magnetization can then be detected in a direction opposite to the external field direction B_0. Diamagnetic agents are not used as contrast agents for their effects on T_1 and T_2 relaxation time. The consequence of diamagnetism is a very weak and negative susceptibility.

S. Laurent et al., *MRI Contrast Agents*, Nanotheranostics,
DOI 10.1007/978-981-10-2529-7_2

2.2 Paramagnetic Substances

Ions or molecules possessing unpaired electrons tend to move in the direction of the magnetic field and increase its effect, these compounds are called paramagnetic substances. The more unpaired electrons, the greater is the electron magnetic moment and the more important will be the paramagnetic properties. All transition metals (Cr^{2+}, Cr^{3+}, Mn^{2+}, Mn^{3+}, Fe^{2+}, Fe^{3+}) and lanthanides (Gd^{3+}, Dy^{3+}) have a significant number of unpaired electrons. The gadolinium ion, with seven free electrons, has a large magnetic moment. It was first chosen as the base of paramagnetic MRI contrast agents.

2.3 Ferromagnetic Substances

While paramagnetism is a property from the isolated ion, ferromagnetism is a property based on the cooperation of thousands of atoms in a paramagnetic crystal structure. Ferromagnetic compounds have regions or domains where there is an overall magnetization. Before being subjected to an external field, a ferromagnetic compound has no spontaneous magnetization: the different magnetic domains are oriented randomly. After application of an external field, the magnetic fields are oriented along the axis of the field and have a bulk magnetization describing a hysteresis curve (Fig. 2.1a). When the magnetic field B reaches a certain value, the saturation magnetization Ms is obtained and the magnetization stays constant. When B is stopped, the magnetization is maintained at Ms and then slowly decreases to the isothermal remanent magnetization. The coercive force (or coercivity) is the intensity of the applied magnetic field required to reduce the magnetization to zero after reaching the Ms.

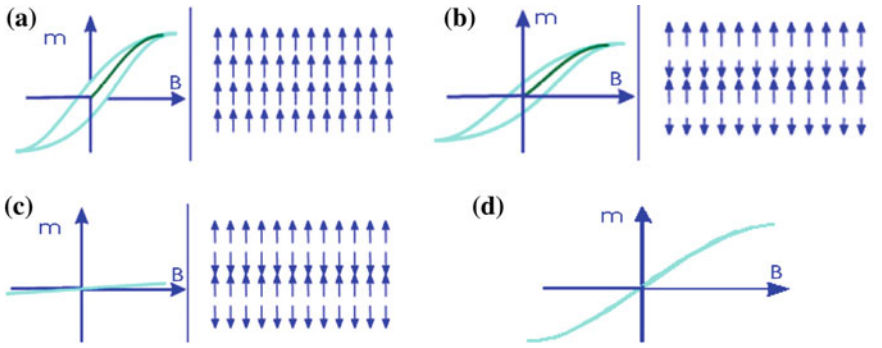

Fig. 2.1 Different kinds of magnetisms: magnetisation curves of **a** ferromagnetic **b** ferrimagnetic **c** antiferromagnetic **d** superparamagnetic material

2.4 Ferrimagnetic Substances

Ferrimagnetism is characterized by two sub-networks in which the spins are antiparallel. However, their magnetic moments are not equal and do not compensate completely (Fig. 2.1b).

2.5 Antiferromagnetic Substances

Antiferromagnetic materials are composed of ferromagnetic sub-networks whose magnetic moments are identical and of opposite directions (Fig. 2.1c). Therefore, in the absence of an external field, the resulting magnetization is zero. By heating above a characteristic temperature of the material (Neel temperature), the material becomes paramagnetic.

2.6 Superparamagnetic Substances

The concept of superparamagnetism is very close to that of ferromagnetism, the difference being the coherent strength of the magnetic domains. When the external magnetic field is stopped, different magnetic domains found a random orientation and their resultant is zero (Fig. 2.1d). The superparamagnetism appears when the crystal size becomes sufficiently small. The crystal becomes a single domain when the size is below a critical value. A single domain magnetic crystal has no hysteresis loop. A crystal is superparamagnetic when it demagnetizes completely when the field is removed. Suspensions of iron oxide nanoparticles smaller than 20 nm display superparamagnetic behavior at room temperature. The degree of alignment of magnetic moments depends of the temperature. The alignment decreases when the temperature increases and beyond a critical temperature, the magnetization becomes zero.

For magnetite and maghemite, this critical temperature is called Curie temperature T_c. For example, magnetite has a Curie temperature of 850 K [1]. At room temperature, magnetite particles smaller than 6 nm are superparamagnetic [2]. Their magnetic properties depend on their synthesis method and crystal morphology [3–6].

The bulk magnetite is a natural material in which the magnetic domains are divided in **Weiss domains** separated thanks to walls called **Bloch walls** [7]. Inside each domain, the magnetic moments possess uniform directions whereas the surrounding magnetic domains exhibit a different direction of magnetic moments (Fig. 2.2a). The disposition in magnetic domains optimizes the system energy [8].

If an external magnetic field (H) is applied, the Bloch walls move and induce an increase of the magnetic domains oriented in the same direction as the external magnetic field. Depending on the strength of the external magnetic field, the

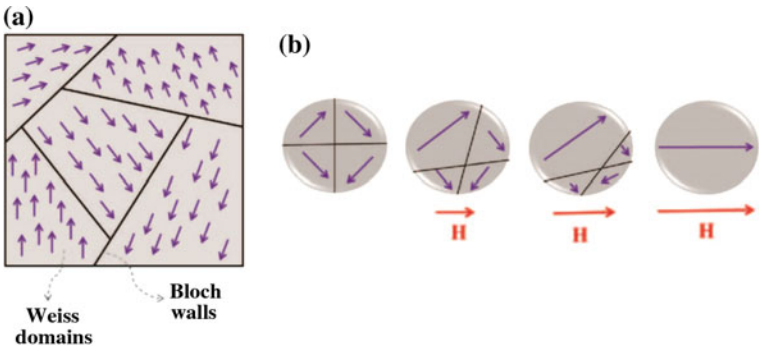

Fig. 2.2 **a** Organization of magnetic domains for ferromagnetic materials and **b** arrangement of Weiss domains as a function of applied magnetic field (H) with different intensities

predominant magnetic domains expanded much more compared to the other domains. A high magnetic field is required to completely remove the Bloch walls as shown in Fig. 2.2b. This phenomenon is at the origin of the remanent magnetization (M_r) and of the hysteresis observed [9, 10] during the measurement of magnetic moments as a function of applied magnetic field (Fig. 2.3).

Initially, the material is not magnetized (**a**) and the magnetic moment increases while an external magnetic field (H) is applied. The red curve (**b**) represents the first magnetization curve in which the Bloch walls move to promote the dominant direction of the magnetic domains present in ferromagnetic compounds as previously shown in Fig. 2.2b. The magnetic moment increases until reaching the

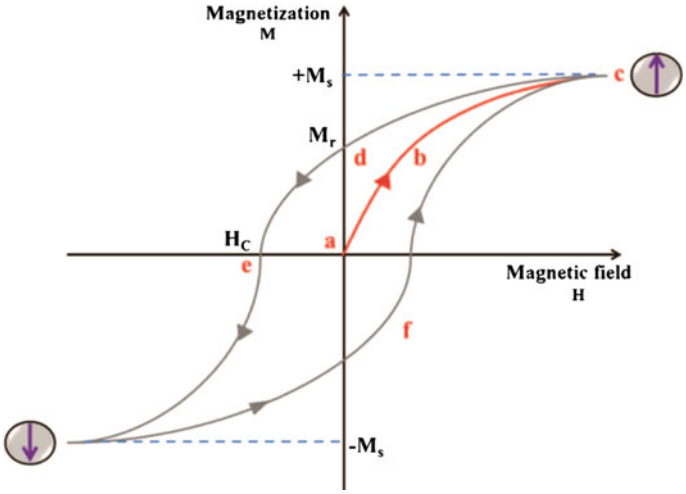

Fig. 2.3 Hysteresis curve of a ferromagnetic compound with the representation of the saturation magnetization (M_s), the coercive field (H_c) and the remanent magnetization (M_r)

saturation magnetization (M_s), corresponding to the state where all the magnetic moments are aligned with the external magnetic field (**c**). If the intensity of magnetic field is then reduced, the magnetic moment will decrease (**d**). At zero magnetic field, the magnetic moment is equal to a value corresponding to the remanent magnetization (M_r). This resulting magnetization is a fundamental characteristic of the ferromagnetic substances and it is due to the presence of domain structure [11]. To demagnetize the materials (**e**), it is necessary to apply an opposite magnetic field called coercive field (H_c). By a continuous increase of the magnetic field in opposite direction, the magnetic moment decreases to a minimum value ($-M_s$). At this point, an increase of H induces an enhancement of magnetization to the saturation magnetization; however, a larger value of H will be needed to reach a zero magnetization. The final curve describes the hysteresis cycle that is an important characteristic of the ferromagnetic compounds. It is important to determine the remanent magnetization and the coercive field. Both parameters depend on the nature and the size of the materials. On the contrary, the saturation magnetization does not depend on the material size and it is only influenced by chemical composition.

If the material size is small enough, the coercive field will become equal to zero and the remanent magnetization will disappear. Consequently, these materials react as a paramagnetic compound. However, the size of these magnetic substances must be small enough to form a single crystal domain in which these materials acquire uniform high magnetization with all the spins aligned in the same direction (Fig. 2.4). This phenomenon is called **superparamagnetism** and differs from paramagnetism. Indeed, the magnetic moments of these compounds are much larger than those of electrons responsible of paramagnetic behavior. To have superparamagnetic materials, the size must be less than a Weiss domain of the corresponding material bulk.

The magnetization curve of superparamagnetic materials is not defined by a hysteresis curve as observed for the ferromagnetic compounds. The curve is reversible with no remanence and no coercive field (Fig. 2.5).

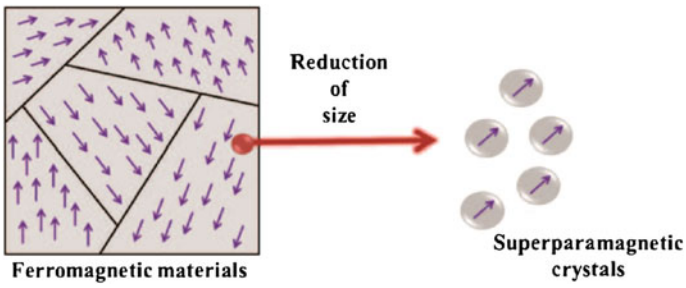

Fig. 2.4 Comparison between the multidomain structure of ferromagnetic materials and the singledomain of superparamagnetic crystals

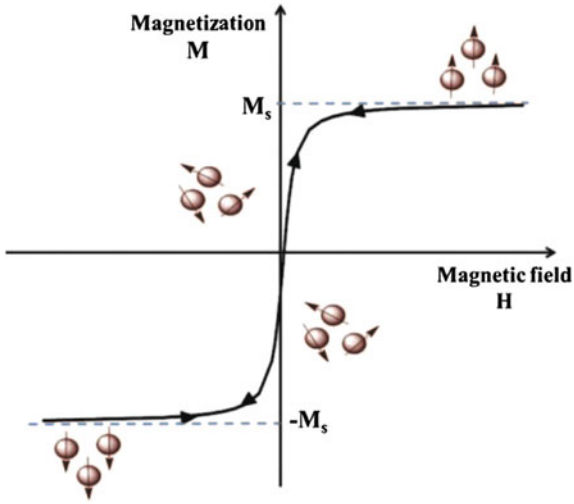

Fig. 2.5 Magnetization curve of superparamagnetic materials

The appearance of the magnetization curve of superparamagnetic materials can be defined as a Langevin function (L(α)) as follows:

$$L(\alpha) = \cosh\left(1 - \frac{1}{\alpha}\right) \quad with\, \alpha = \frac{\mu H}{k_b T}$$

Where μ is the particle magnetic moment, H is the external magnetic field, k_b is the Boltzmann constant and T is the temperature.

The net magnetization (M) is described as the saturation magnetization (M_s) multiplied by Langevin function (L(α)):

$$M = M_S L(\alpha)$$

The size and the saturation magnetization of superparamagnetic particles can be determined from the measurements of magnetization curve thanks to their fitting by Langevin function [12, 13]. For this, the assumptions are that all particles exhibit the same volume and that the saturation magnetization is considered as an average value.The superparamagnetism is a particular magnetic property widely exploited in the field of relaxometry and relaxing agents.

References

1. Schwertmann U (1988) Some properties of soil and synthetic iron oxides (Chapter 9). In: Stucki JW, Goodman BA, Schwertmann U (eds) Iron in soils and clay minerals, series c: mathematical and physical sciences, vol 217, pp 203–250 (NATO ASI series)

2. Sena SP, Lindley RA, Blythe HJ et al (1997) Investigation of magnetite thin films produced by pulsed laser deposition. J Magn Magn Mater 176(2–3):111–126
3. Kado T (2008) Structural and magnetic properties of magnetite-containing epitaxial iron oxide films grown on MgO (001) substrates. J Appl Phys 103(4):043902-1–043902-4
4. Qiu H, Pan L, Li L et al (2007) Microstructure and magnetic properties of magnetite thin films prepared by reactive sputtering. J Appl Phys 102(11):113913-1–113913-5
5. Margulies DT, Parker FT, Spada FE et al (1996) Anomalous moment and anisotropy behavior in Fe3O4 films. Phys Rev B 53(14):9175–9187
6. Margulies DT, Parker FT, Rudee ML et al (1997) Origin of the anomalous magnetic-behavior in single-crystal Fe3O4 films. Phys Rev Lett 79(25):5162–5165
7. Kittel C (1949) Physical theory of ferromagnetic domains. Rev Modern Phys 21(4):541–583
8. Weiss P (1907) L'hypothèse du champ moléculaire et la propriété ferromagnétique. J. Phys Théor Appl 6(1):661–690
9. Teja AS, Koh P-Y (2009) Synthesis, properties, and applications of magnetic iron oxide nanoparticles. Progress Cryst Growth Charact Mater 55(1–2):22–45
10. Schneider CS (2002) Role of reversible susceptibility in ferromagnetic hysteresis. J Appl Phys 91(10):7637–7639
11. Frenkel J, Doefman J (1930) Spontaneous and induced magnetisation in ferromagnetic bodies. Nature 126:274–275
12. Langevin P (1905) Magnétisme et théorie des électrons. Annales de Chimie et de Physique 5 (8):70–127
13. Chen DX, Sanchez A, Taboada E et al (2009) Size determination of superparamagnetic nanoparticles from magnetization curve. J Appl Phys 105(8):083924

Chapter 3
Imaging Probes

Abstract This chapter briefly describes the principle of nuclear magnetic resonance (NMR) and more particularly of magnetic resonance imaging (MRI). This is necessary to fully understand the importance of developing new MRI contrast agents.

Imaging technologies are the "spies of surgeons", as they allow to collect and process information of patients without chirurgical operation. Over the past decades, medical imaging technology has been developed at amazing speed, including radiography, ultrasonography, echocardiography, magnetic resonance imaging (MRI). X-ray is mostly used in radiography for its prominent penetration, while the cancer risk induced by X-ray irradiations increases anxiety of clinicians and patients [1, 2]. Therefore, MRI and optical imaging (OI) become growing interesting challenges. However, each imaging technology has its particular advantages and disadvantages, which prompts researchers to combine different technologies to form bi-functional or multi-functional imaging technologies. The need for multifunctional imaging probes has increased the interest for nanoparticles as platform where several fluorophores, biological vectors, radioisotopic molecules, MRI contrast agents, … can be grafted.

3.1 Magnetic Resonance Imaging (MRI)

MRI uses nonionizing radiation and has become an indispensable tool in clinical radiology, and more recently in experimental research. Compared to computer tomography (CT), MRI can also produce noninvasive and painless diagnosis of disease, but without cancer risk caused by X-ray radiation. After Felix Bloch and Edward Purcell (the Nobel Prize winners in 1952) discovered the magnetic resonance phenomenon independently in 1946, nuclear magnetic resonance (NMR) was developed and used for chemical and physical molecular analysis. In 1971 Raymond Damadian reported that the nuclear magnetic relaxation times of tumors

S. Laurent et al., *MRI Contrast Agents*, Nanotheranostics,
DOI 10.1007/978-981-10-2529-7_3

were different from those of tissues [3], which motivated scientists to consider magnetic resonance for the detection of disease. The 2003 Nobel Prize winners in physiology or medicine Paul Lauterbur and Sir Peter Mansfield used magnetic field gradients to determine spatial localization [4], which allowed rapid acquisition of 2D images and made MRI developing rapidly in clinical diagnosis.

There are two discrete energy states in a system of protons. In such a system the protons occupy the high or low state according to a defined probability, which is called Boltzmann distribution or Gibbs distribution. The ratio between numbers of particles N_i and N_j occupying the states possessing energy E_i and E_j, respectively, can be calculated as:

$$N_i/N_j = \exp(\Delta E/kT)$$

where $\Delta E = (E_j - E_i)$ is the energy difference between the two states, k and T are the Boltzmann constant and the absolute temperature, respectively. With the existence of an applied magnetic field B_0 and a radio frequency electromagnetic field B_1, ΔE will increase proportionally to B_0, following the equation:

$$\Delta E = h\nu = \frac{h(B_0 - B_e)\gamma}{2\pi}$$

where h is the Plank's constant, ν is the frequency of the B_0 field, B_e is a small magnetic field generated by the circulation of electrons of the molecule, and γ is the gyromagnetic ratio (a constant which is a property of the particular nucleus). Therefore, the difference of the protons in the low and high energy states will increase, and the NMR signal intensity increases with it, as the NMR intensity is directly dependent on the population difference. So strong magnetic field is commonly applied to enhance the NMR signal and to obtain larger signal-to noise ratio.

MRI uses the property of NMR to image nuclei of atoms inside the body. The intensity of the signal in each voxel depends on several intrinsic parameters, including the proton density, longitudinal (R_1) and transverse (R_2) NMR relaxation rates, and some extrinsic parameters, including magnetic field strength, pulse sequence, and the presence of contrast agents (CAs). The magnetic field is used to align the magnetization of atomic nuclei of ^{1}H in the body, and radio frequency magnetic fields are used to tune the alignment of this magnetization, which causes the nuclei to produce a rotating magnetic field detectable by the scanner. This process where the system discharges the excess energy and returns to the equilibrium state is called relaxation. Magnetic field gradients make nuclei at different locations to spin at different rates, which allow spatial information to be recovered with the help of Fourier analysis of the measured signal. By using magnetic field gradients in different directions, 2D images or 3D volumes can be obtained in any arbitrary orientation.

3.1.1 Classical Description of NMR—Description on the Macroscopic Scale

If we consider a spin packet experiencing the same applied magnetic field B_0 aligned on the z-axis, their motion may be described by a single precessing vector M, called the bulk magnetization (Fig. 3.1a). M is defined as the sum of the individual nuclear magnetic moments of the spin packet.

$$M = \sum_{i=1}^{N} \mu_i$$

$$|M| = \frac{\gamma h}{4\pi}(n_+ - n_-) \approx \frac{\gamma^2 h^2 |B_0| N_S}{16\pi^2 kT} \quad \left[Am^{-1}\right]$$

M is precessing around B_0 at the Larmor frequency. In order to simplify the analysis of its behavior, it is more convenient to introduce a new rotating reference system [x′, y′, z] called rotating frame. The new reference system is defined as rotating around the z axis of the coordinate system [x, y, z] at the Larmor frequency so that M appears as static (Fig. 3.1b).

In the rotating frame, M is defined by its longitudinal component (M_z) which is its projection on the z axis and by its transversal component (M_t) which is its projection in the xy plane (Fig. 3.1b).

The application of a radiofrequency pulse at the Larmor frequency induces a temporary transient magnetic field B_1 in the xy plane. The net magnetization is flipped from its equilibrium and spins are precessing around B_1. The flip angle (also called pulse angle) depends on the duration of the RF pulse and on the magnitude of B_1. A 90° pulse tips the M_0 magnetization by 90°, a two times longer radiofrequency results in a 180° pulse.

When the system is submitted to a radiofrequency wave at the Larmor frequency, spins are promoted to the higher energy state and the magnetization flips

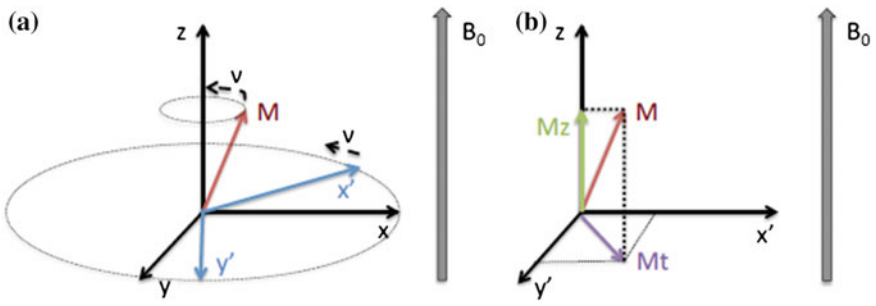

Fig. 3.1 Representation of the bulk magnetization (M) in a coordinate reference system. **a** Precession of M and of the new coordinate system [x′, y′, z] around z at the Larmor frequency (ν), **b** Representation of M in the rotating frame

away from its equilibrium position so that the longitudinal component of the net magnetization, M_z, is lower than M_0 (M at the equilibrium).

When stopping the excitation, the system progressively returns back to equilibrium, M_z grows up until it reaches its initial M_0 value (Fig. 3.2).

This phenomenon is called spin-lattice relaxation and depends on the T_1 relaxation time. T_1 is defined as the time needed to recover 63 % of the net magnetization value at the equilibrium after a 90° pulse.

The longitudinal component of the net magnetization at a time "t" after a 90° pulse can be expressed as an increasing exponential equation:

$$M_z(t) = M_0\left(1 - e^{-t/T_1}\right) \quad \left[Am^{-1}\right]$$

The transversal component $M_{x',y'}$ is defined as the projection of the M vector in the xy plane and is 0 at the equilibrium.

$$M_{x'y'} = \left| \underset{x}{\rightarrow} M_{x'} + \underset{y}{\rightarrow} M_{y'} \right| \quad \left[\mathrm{Am}^{-1}\right]$$

After excitation, the transverse magnetization decays because of the loss of phase coherence of the individual magnetic moments. The transversal relaxation is

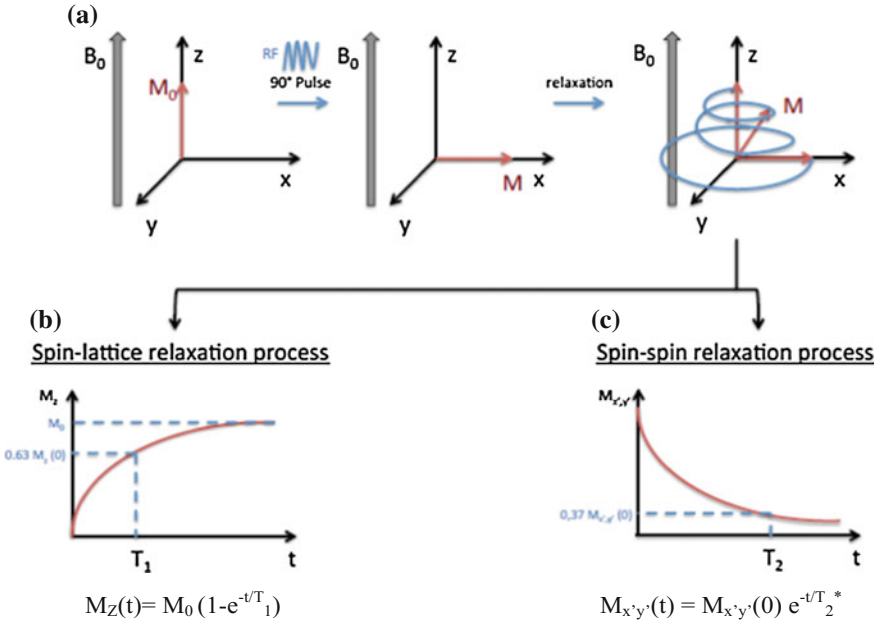

Fig. 3.2 Behavior of the bulk magnetization (M) after a 90° pulse (**a**). Description of the relaxation processes: the spin-lattice relaxation (**b**) and the spin-spin relaxation process (**c**)

depending on the time constant T_2 that is defined as the time needed to reduce the transversal magnetization component by 63 %. It is described by the following decreasing exponential equation:

$$M_{x'y'}(t) = M_{x'y'}(0)e^{-t/T_2} \quad \left[\mathrm{A}m^{-1}\right]$$

The transverse relaxation is mostly due to spin-spin interactions but is also depending on the magnetic field inhomogeneities that make spins precessing at different frequencies and on the surrounding environment (temperature, interferences with other molecules, microviscosity, …). Consequently, the time constant of the decay T_2^* is given by

$$\frac{1}{T_2^*} = \frac{1}{T_2} + \frac{1}{T_2^{inh}}$$

where T_2^{inh} is related to the inhomogeneities.

T_2 is always smaller or equal to T_1.

3.1.2 NMR Signal Acquisition

After a 90° pulse, the magnetization starts precessing in the xy plane and generates an electromagnetic signal that can be detected by a receiver coil placed in the xy plane (Fig. 3.3).

The recorded signal is the FID that is a signal decaying with an exponential time constant T_2^*.

In Fourier Transform NMR spectroscopy broad frequency pulses are used to excite all the spins present in the sample. The application of a mathematical treatment on the FID signal (Fourier transformation) leads to the creation of a frequency spectrum. This spectrum yields information on the quantity and Larmor frequencies of the nuclei present in the sample and consequently information concerning the chemical structure of the sample is provided.

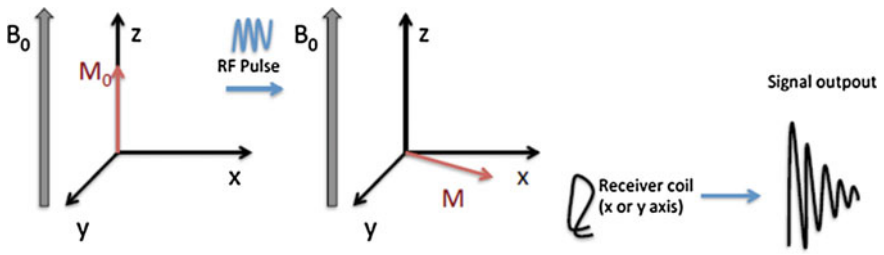

Fig. 3.3 NMR signal acquisition, registration of the FID signal thanks to a receiver coil placed on x or y axis

3.1.3 *Principle of MRI*

Magnetic resonance imaging is a non-invasive imaging technique based on the nuclear magnetic resonance phenomenon. It provides a cartography of the ^{1}H density in an object. As hydrogen constitutes approximately 63 % of the atoms of the human body, it is the most studied nucleus.

3.1.3.1 Spatial Coding

MRI requires the recording of the MR signal from each individual volume element (voxel). The spatial coding of the signal is achieved by the use of gradient fields which make the magnetic field intensity and consequently the Larmor frequency spatially dependent.

The first step of the acquisition is the excitation of a specific slice of the image object. This is made by imposing a gradient G_z to the main magnetic field B_0 (Fig. 3.4). The intensity of the resulting magnetic field increases along z and the resonant frequency (v) at the time t and at the position z is,

$$\upsilon(z,t) = \frac{\gamma}{2\pi}(|B_0| + G_z(t)z) \quad [Hz]$$

Then, the slice selection gradient is turned off and a gradient along the y-axis (called the phase encoding gradient) and a gradient along the x-axis (frequency encoding gradient) allow to record the signal from each voxel.

During examinations, the typical thickness of the excited slices is several millimeters. Gradient fields are in the order of μT and can be rapidly switched on and off to encode the spatial position of the NMR signal.

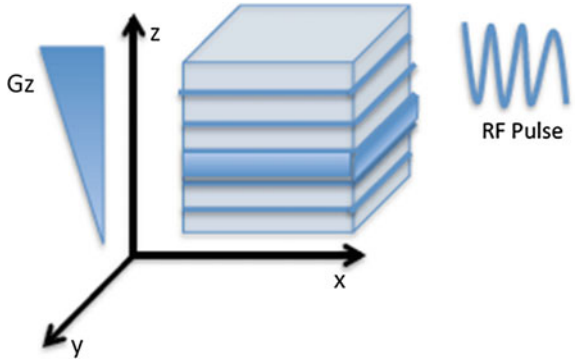

Fig. 3.4 Slice selection through the application of a magnetic field gradient along z (Gz)

3.1.3.2 Excitation Sequence

The spin echo sequence is one of the most commonly used imaging sequence that aims to improve the quality of the recorded signal while making it less susceptible to inhomogeneities.

The sequence consists of a 90° pulse that flips the magnetization out of its equilibrium. Because of inhomogeneities, spins begin to spread out leading to a weaker signal. To compensate this T_2^{inh} effect, the 90° pulse is followed after a defined time by a 180° refocusing excitation pulse that consists in flipping the dephasing spins in the transversal plane so that spins begin to rephase until a time called echo time (TE) at which the signal is maximum along x′ and is recorded (Fig. 3.5). The intensity of this signal depends on the TE and on the T_2 of the nuclei.

3.1.3.3 Contrast in MRI

Tissues are characterized by different proton densities, T_1 and T_2 relaxation times. These values are exploited to generate natural contrast on images.

Nevertheless, it is possible to improve the contrast by varying parameters such as the echo time (TE) and the repetition time (RT) leading to proton density, T_1 or T_2-weighting of the spin echo sequence.

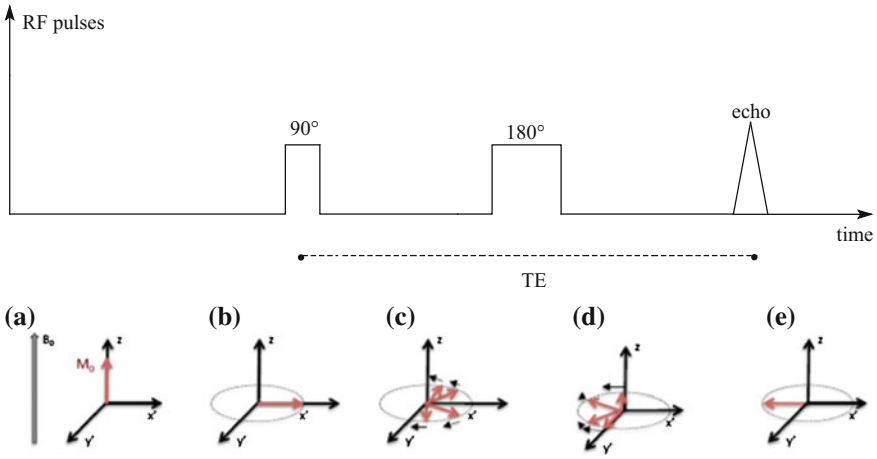

Fig. 3.5 Representation of a spin-echo sequence. **a** Bulk magnetization in the presence of a static magnetic field (B_0), after the application of a 90° pulse (**b**), spins start to loose phase coherence due to field inhomogeneities (**c**). The application of a 180° pulse makes them to flip in the x−y plane (**d**) and spins rephase until the TE (echo time) when the signal reaches its maximum and is measured (**e**)

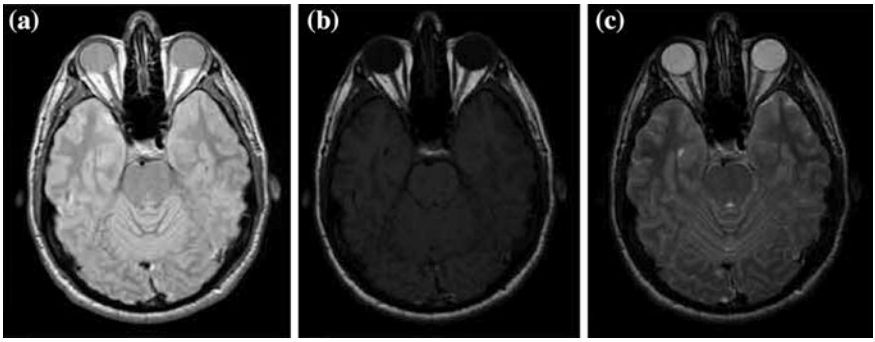

Fig. 3.6 Illustration of the TE and RT effect on the contrast of a transversal section of a human brain MR image. **a** Proton density weighted images (RT = 4 s, TE = 20 ms), **b** T_1-weighted image (RT = 500 ms, TE = 20 ms) and **c** T_2-weighted image (RT = 4 s, TE = 80 ms). *Source* http://www.thebarrow.org/Education_And_Resources/Barrow_Quarterly/205116

By setting $TE \ll T_2$ and $T_1 \ll RT$, the received signal is not affected by the relaxation phenomenon and the generated MRI image is mostly related to the proton density (Fig. 3.6a).

The differentiation between the T_1 relaxation times of tissues is emphasized if $RT < T_1$ (and $TE < T_2$) because the magnitude of the signal becomes T_1 dependent and images are T_1-weighted (Fig. 3.6b).

If $T_2 < TE$ (and $RT \gg T_1$), the sequence is mainly sensitive to T_2 relaxation times and images are T_2-weighted (Fig. 3.6c).

However, sometimes the contrast generated by the relaxation times and the differences in water content is not sufficient to discern diseased from healthy tissues. Then clinicians use compounds called contrast agents able to enhance the contrast in the area of interest where they accumulate.

3.2 MRI Contrast Agents

Multiple classifications are possible [5, 6]. Contrast agents can be classified according to their route of administration, their magnetic properties and thus their effect on the contrast, their size or their distribution in the body.

The mode of action of all MRI contrast agents is based on the reduction of T_1 and T_2 relaxation times of water protons. Two categories can be distinguished:

- T_1 agents, the main effect is a decrease of the longitudinal proton relaxation time. This relaxation time depends on the rate at which the proton transfers its excited energy to the surrounding medium.
- T_2 agents, the main effect is a decrease of the transverse proton relaxation time. T_2 depends on the rate at which protons are out of phase with each other.

T_1 and T_2 nuclear relaxation times are expressed in seconds. The relaxation rates (R_1 and R_2) are the reciprocal of relaxation time ($1/T_1$ and $1/T_2$) and are expressed in s^{-1}. The effect of a contrast agent on the relaxation rates is linearly proportional to its concentration. The essential property of contrast agents is their "relaxivity" (r_1 and r_2) defined as the contribution to the relaxation rate of water protons at a concentration of 1 mM ($s^{-1}mmol\ l^{-1}$). Relaxivity thus defines the efficiency of the contrast agent to increase the relaxation rate of surrounding protons. The r_2/r_1 ratio is sometimes used to indicate the magnitude of the T_2 effect compared to T_1 effect.

References

1. de Gonzalez AB, Darby S (2004) Risk of cancer from diagnostic X-rays: estimates for the UK and 14 other countries. Lancet 363:345–351
2. Harvey EB, Boice JD Jr, Honeyman M (1985) Prenatal x-ray exposure and childhood cancer in twins. N Engl J Med 312:541–545
3. Damadian RV (1971) Tumor detection by nuclear magnetic resonance. Science 171: 1151–1153
4. Lauterbur PC (1973) Image formation by induced local interactions: examples employing nuclear magnetic resonance. Nature 242:190–191
5. Laurent S, Vander Elst L, Muller RN (2006) Comparative study of the physicochemical properties of six clinical low molecular weight gadolinium contrast agents. Contrast Med Mol Imaging 1:128–137
6. Geraldes CF, Laurent S (2009) Classification and basic properties of contrast agents for magnetic resonance imaging. Contrast Med Mol Imaging 4:1–23

Chapter 4
Paramagnetic Gadolinium Complexes

Abstract The mechanism of action of the paramagnetic gadolinium complexes is briefly described, with an emphasis on the different parameters that can be tuned to increase their efficiency. An overview of the different classes of paramagnetic gadolinium chelates is then presented.

Contrast agents (CAs) for various kinds of imaging methods have been used for decades in diagnostic radiology and developmental biology [1]. The synthesis and applications of paramagnetic CAs were reported with a rapidly growing rate by scientists, and more than 30 % of all clinical MRI examinations use CAs [2]. Paramagnetic metal ion with unpaired electrons can act as the relaxation enhancement agents for MRI, by increasing the relaxation rates R_1 and R_2 of close-by spins. Such enhancements on R_1 and R_2 can be used to assess the efficiency of an MRI CA, following the equation:

$$R_i^{obs} = R_i^d + R_i^p \quad i = 1, 2$$

where R_i^{obs} is the observed solvent relaxation rate in the presence of a CA, and the subscripts d and p refer to diamagnetic and paramagnetic, respectively. The paramagnetic contribution is dependent on the concentration of CAs, in the form of r_i [M] where [M] is the concentration of CAs and r_i is the relaxivity, defined as the relaxation rate R_i increased per unit concentration of CAs. The origin of the paramagnetic contribution is usually divided into two components, inner-sphere (IS) and outer-sphere (OS) mechanisms:

$$R_i^p = R_i^{IS} + R_i^{OS} \quad i = 1, 2$$

where R_i^{IS} and R_i^{OS} refer to relaxation enhancement of the bulk solvent related to solvent molecules directly coordinated to the paramagnetic ion in the innersphere and relaxation enhancement of solvent molecules in the outer sphere, respectively (Fig. 4.1a, b) [3].

Lanthanide Gd(III) ion has been employed as the metal ion for MRI T_1 agents, for its high magnetic moment ($\mu^2 = 63\mu_B^2$) and symmetric electronic ground state

S. Laurent et al., *MRI Contrast Agents*, Nanotheranostics,
DOI 10.1007/978-981-10-2529-7_4

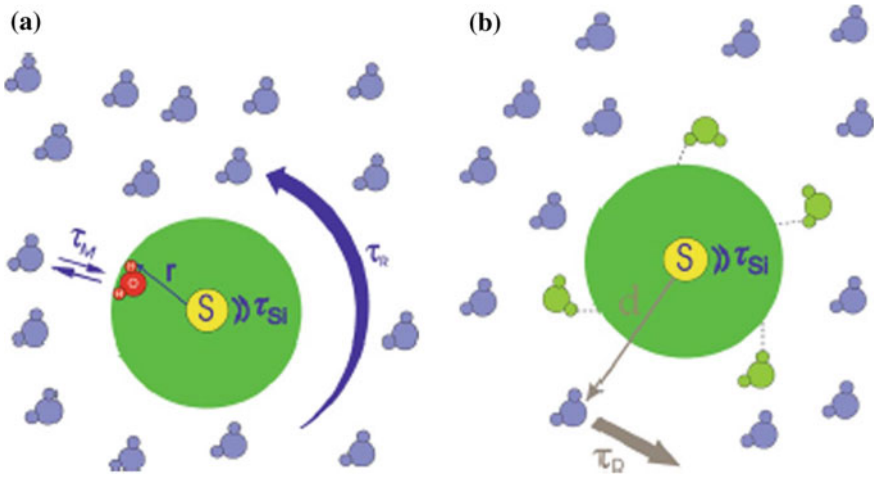

Fig. 4.1 Representation of the innersphere (**a**) and outersphere (**b**) contribution. Reproduced with permission of Ref. [3]

(S^8) [4]. Gd ions have a relatively long electronic relaxation (10^{-8} to 10^{-9} s) compared with other lanthanides, allowing efficient transfer of the magnetic information to the water molecules. These complexes have relaxivities r_1 and r_2 of the order of 3 to 10 s^{-1} mM^{-1} at 1.5 T. However, as the T_1 of the tissue is much higher than their T_2 (≈10 fold), the effect is much more marked on T_1 leading to an increase of the MRI signal (bright signal). These complexes are called positive contrast agents. The larger the T_1 weighting of the sequence, the greater the contrast will be. The T_1-weighted images may be obtained with short TR and TE compared to T_1 and T_2.

Gadolinium ion is, however, extremely toxic because its radius is close to that of the calcium ion and therefore Gd ion can replace it. Furthermore Gd ions are not stable at physiological pH and produce gadolinium hydroxide crystals that can form deposits and block vessels. To overcome these problems, the Gd ion is complexed by a linear polycarboxylate-type organic ligand, diethylenetriaminepentaacetic acid (DTPA) or macrocyclic tetra-azacyclododecanetetraacetic acid (DOTA) [34] (Fig. 4.2). Since Gd-DTPA (Magnevist®) was approved in 1988, around 10 kinds of Gd chelates have been approved or are in clinical trials as MRI CAs, and over 600 references on Gd(III) chelates appear every year.

The first six contrast agents (Gd-DTPA, Gd-DTPA-BMA, Gd-DTPA-BMEA, Gd-DOTA, Gd-HP-DO3A and Gd-BT-DO3A), called first generation products are administered at a dose 0.1 mmol/kg body weight in the form of an aqueous solution of 0.5 M in Gd. These complexes are distributed in the extracellular space, do not exhibit tissue specificity and are rapidly excreted renally.

The three last Gd complexes are part of the second generation of contrast agents. Gd-EOB-DTPA [5] and Gd-BOPTA [6] are hepatobiliary agents because they are specifically taken up by healthy hepatocytes and allow to highlight lesions in the

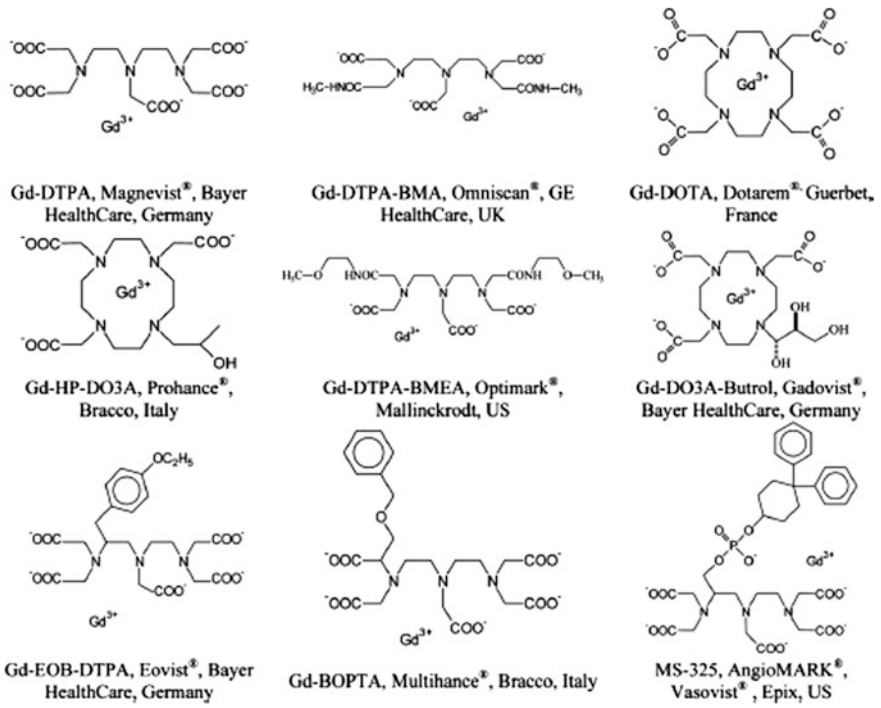

Fig. 4.2 Structure of approved Gd complexes as MRI contrast agents

liver. MS-325 [7] is an angiographic agent with a high affinity for human serum albumin (HSA) which gives it a high residence time in vessels.

4.1 Relaxation Mechanims of Gadolinium Complexes

For small gadolinium chelates, two main contributions can be distinguished in the relaxation mechanisms: the innersphere mechanism (IS) dealing with the water molecules bound to the first coordination sphere of the gadolinium ion and the outer-sphere mechanism (OS) concerning water molecules diffusing near the paramagnetic center.

For some chelates, an additional contribution defined as the second-sphere (SS) mechanism is necessary but this contribution is generally neglected.

Therefore, the effect of Gd chelate on the longitudinal water relaxation rate (R1p) is given by

$$R_1^P = R_1^{IS} + R_1^{OS}\left(+R_1^{SS}\right)$$

4.1.1 Innersphere Mechanism

The innersphere mechanism allows the propagation of the paramagnetic effect from the paramagnetic center to the bulk solution (Fig. 4.3). It is based on the chemical exchange of water molecule(s) in the first coordination sphere of the gadolinium ion and the water molecules constituting the bulk.

The innersphere contribution was described by Salomon-Bloembergen theory [8, 9] as an exchange of water molecules between two sites (Fig. 4.3) and is expressed by the following equation for solutions containing low concentrations of paramagnetic chelates.

$$R_1^{is} = fq\frac{1}{T_{1M} + \tau_M}$$

where f is the molar fraction of the paramagnetic agent, q is the number of water molecules coordinated to the first coordination sphere, T_{1M} is the longitudinal

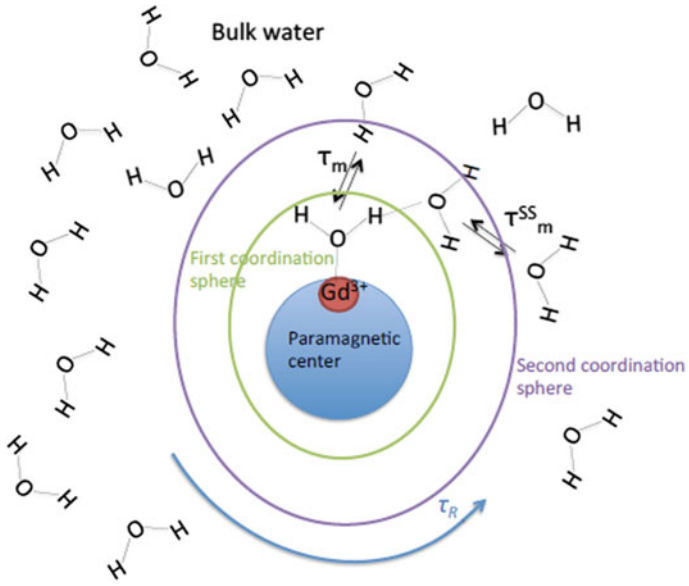

Fig. 4.3 Schematization of a paramagnetic complex with one innersphere water molecule, one second-sphere water molecule and several outersphere water molecules (bulk water molecules)

relaxation time of the coordinated water molecules and τ_M is the residence time of water in the first coordination sphere.

A dipolar mechanism governs the longitudinal relaxation rate of the water molecules coordinated to gadolinium chelates following the equation:

$$\frac{1}{T_{1M}} = \frac{1}{T_{1M}^{DD}} = \frac{2}{15}\left(\frac{\mu_0}{4\pi}\right)^2 \gamma_I^2 \gamma_S^2 \hbar^2 S(S+1)\frac{1}{r^6}\left[\frac{7\tau_{c2}}{1+(\omega_S\tau_{c2})^2} + \frac{3\tau_{c1}}{1+(\omega_I\tau_{c1})^2}\right]$$

where γ_I and γ_S are the nuclear (I) and the electron (S) gyromagnetic ratios, respectively ($\gamma_I = 2.675 \times 108$ rad s^{-1} T^{-1}, $\gamma_S = 1.76 \times 10^{11}$ rad s^{-1} T^{-1}), ω_S and ω_I are the Larmor pulsations of the electron and of the proton, respectively, r is the effective distance between the electron charge and the ^1H nucleus, τ_{ci} are the correlation times that modulates the interaction, with i = 1, 2.

These can be expressed by the equation:

$$\frac{1}{\tau_{ci}} = \frac{1}{\tau_R} + \frac{1}{\tau_M} + \frac{1}{\tau_{si}}$$

where τ_R is the rotational correlation time and τ_{S1} and τ_{S2} are the longitudinal and transverse relaxation times, respectively, of the impaired electrons. They can be expressed as,

$$\frac{1}{\tau_{S1}} = \frac{1}{5\tau_{SO}}\left[\frac{1}{1+\omega_S^2\tau_V^2} + \frac{4}{1+4\omega_S^2\tau_V^2}\right]$$
$$\frac{1}{\tau_{S2}} = \frac{1}{10\tau_{SO}}\left[3 + \frac{5}{1+\omega_S^2\tau_V^2} + \frac{2}{1+4\omega_S^2\tau_V^2}\right]$$

where τ_v is the relaxation time at zero field and depends on the tensor of the ZFS (zero field splitting).

4.1.2 Outer-Sphere Mechanism

The outer-sphere relaxation was described by Freed [10, 11] and comes from the dipolar interaction between the diffusing water molecules close to the gadolinium ion and the gadolinium ion itself. It is only governed by the relative motion of two entities and their distance of closest approach. The outer-sphere relaxation rate is given by the following equation:

$$R_I^{os} = \frac{32\pi}{405}\gamma_I^2\gamma_S^2\hbar^2 S(S+1)\frac{NA}{1000}\frac{[C]}{dD}[7j(\omega_S\tau_D) + 3j(\omega_I\tau_D)]$$

where $N_A$is the Avogadro number, [C] is the concentration of paramagnetic entities and τ_D is the time modulation characterizing the outersphere mechanism named the diffusion correlation time and expressed by equation:

$$\tau_D = \frac{d^2}{(D_I + D_S)} = d^2/D$$

where d is the distance of closest approach between the gadolinium ion and the ^1H nucleus of the diffusing water molecules and D_I and D_S are the molecular diffusion coefficients of water and of the paramagnetic entity, respectively.

$$j(\omega\tau_D) = \mathrm{Re}\left[\frac{1 + \frac{1}{4}(i\omega\tau_D + \tau_D/\tau_{S1})^{1/2}}{1 + (i\omega\tau_D + \tau_D/\tau_{S1})^{1/2} + \frac{4}{9}(i\omega\tau_D + \tau_D/\tau_{S1}) + \frac{1}{9}(i\omega\tau_D + \tau_D/\tau_{S1})^{3/2}}\right]$$

4.1.3 Second-Sphere Mechanism

Second-sphere mechanism concerns water molecule protons that are not directly coordinated to the paramagnetic centers but which interact with coordinated protons through hydrogen bonds for example. They constitute the second coordination sphere (Fig. 4.3).

$$R_1^{SS} = fq^{SS}\frac{1}{T_{1M}^{SS} + \tau_M^{SS}}$$

where q^{SS} is the number of water molecules in the second coordination sphere and τ_M^{ss}, their residence time.

If we define $\tau_{C1,2}^{SS} = \tau_{Ci}^{SS}$, the correlation times modulating the interaction are given by

$$\frac{1}{\tau_{Ci}^{SS}} = \frac{1}{\tau_R^{SS}} + \frac{1}{\tau_M^{SS}} + \frac{1}{\tau_{si}}$$

For gadolinium chelates, $1/T_{1M}^{SS}$ can be expressed as:

$$\frac{1}{T_{1M}^{SS}} = \frac{2}{15}\left(\frac{\mu_0}{4\pi}\right)^2 \gamma_I^2\gamma_S^2\hbar^2 S(S+1)\frac{1}{r_{SS}^6}\left[\frac{7\tau_{c2}^{SS}}{1 + (\omega_S\tau_{c2}^{SS})^2} + \frac{3\tau_{c1}^{SS}}{1 + (\omega_I\tau_{c1}^{SS})^2}\right]$$

where r^{SS} is the distance between the unpaired electron spins and the water protons constituting the second-sphere coordination and τ_R^{SS} is the reorientational time of the water molecule in the second sphere. The second-sphere mechanism can often be neglected.

4.1.4 Influence of the Different Parameters on the Innersphere and Outersphere Contributions

4.1.4.1 Innersphere Contribution

According to the theories developed by Solomon-Bloembergen-Morgan [8, 9, 12], the paramagnetic relaxivity of water protons due to the innersphere contribution depends on several parameters including those listed below.

Number of water coordinated molecules (q) The relaxation rate is proportional to the number of water molecules in the first coordination sphere of the metal ion. A higher q leads to a high relaxivity but is often accompanied by a low thermodynamic stability. The main contrast agents have a single coordinated water molecule.

Residence time of the coordinated water molecule (τ_M) This parameter plays an important role in the proton relaxivity because it modulates the efficiency of the exchange of the water molecules in the first coordination sphere with the bulk solvent water molecules. This factor can be extremely limiting for the observed relaxivity. Rapid exchange of the water coordinated molecule is therefore necessary to have a high relaxivity.

Rotational correlation time (τ_R) This parameter strongly influences the observed relaxivity between 0.5 and 3 T corresponding to the magnetic fields used in clinical MRI. An increase in the value of τ_R causes a marked improvement in the relaxivity values at these magnetic fields. Many studies have been focused on optimizing τ_R and have led to the production of contrast agents with higher molecular weight.

Electronic relaxation time (τ_{Si}) The choice of the Gd^{3+} ion is due to a high unpaired electron number but also to its larger electronic relaxation times, which allow a favorable interaction with the protons of the water coordinated molecule.

4.1.4.2 Outersphere Contribution

This mechanism comes from the freely diffusing water molecules in the vicinity of the paramagnetic center, which can therefore interact with the electron spin. This phenomenon is governed by the relative movement of two molecules and by their distance of smaller approach. The correlation time modulating this magnetic interaction is called the translational correlation time τ_D.

4.1.4.3 NMRD Profiles

Nuclear magnetic relaxation dispersion (NMRD) is a powerful tool that provides the evolution of the relaxivity as a function of the magnetic field [13, 14]. As the magnetic field has no influence on the chemical state of the sample, it is a valuable tool for the study of the interaction mechanisms and dynamic processes influencing the relaxation behavior.

NMRD profiles are recorded using the fast field cycling technique. The theoretical adjustment of these curves provides the efficiency of the contrast agent at a specific magnetic field and a good estimation of several parameters described above such as τ_R, τ_M, τ_V, q, …. Nevertheless, NMRD profiles are influenced by many parameters increasing the complexity of their analyses. Two additional techniques are generally used to probe some parameters: the EPR (Electron Paramagnetic Resonance) for τ_{Si} and ^{17}O NMR for τ_M and q.

The shape of the NMRD profiles of low molecular weight T_1 contrast agents is typical (Fig. 4.4).

4.2 Different Classes of Gadolinium Based MRI Contrast Agents

4.2.1 Vascular Contrast Agents

They are characterized by a long residence time in the vascular system, making them suitable for use in angiography. Two types of products are reported: the covalent complexes, obtained by grafting a low molecular weight contrast agent (<1000 Da) to a macromolecule (>10,000 Da) and the non-covalent complexes in which the small contrast agent binds non-covalently to endogenous

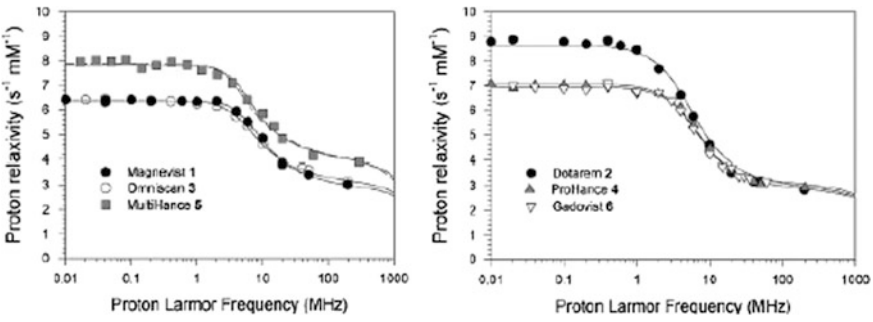

Fig. 4.4 NMRD profiles of several small commercial paramagnetic gadolinium chelates recorded at 37 °C. Reproduced with permission of Ref. [15]

macromolecules (such as HSA). Complexes of intermediate molecular weight (5–10 kDa), for example P792 [16] and P760 [17], are also developed for angiography.

Covalent complexes involve the grafting of a contrast agent, a derivative of Gd-DTPA or Gd-DOTA, on a synthetic or natural polymer, a protein, a dendrimer … [18]. The residence time of some of these macromolecular contrast agents in the body is long and their elimination is sometimes incomplete, increasing the risk of cellular uptake and dissociation of the complex.

Many studies on non-covalent complexes have allowed the development of Gd chelates with high affinity for HSA. Several researches have demonstrated the need for the presence of hydrophobic residues and negative charges to have high affinity. Among these molecules, Gd-EOB-DTPA [5], Gd-BOPTA [6] and MS-325 [7] have been involved in numerous works. In these non-covalent complexes, there is an equilibrium between the free form of the small Gd chelates and the complex bound to the macromolecule. This allows a rapid elimination through the kidneys and a low toxicity.

4.2.2 Smart Contrast Agents

The efficiency of these contrast agents depends on biochemical parameters such as pH [19], temperature [20], oxygen pressure [21], presence of an enzyme [22] or a metal ion (Ca^{2+}, Zn^{2+}, …) [23]. These activatable agents possess two distinct states. One state is *off* and corresponds to low contrast enhancement, while the other state, the *on* state, corresponds to high contrast enhancement. An activatable agent can be *switched* from one state to the other by the occurrence of a metabolic or physiological event. The design of this new class of agents exploits the fundamental means by which a paramagnetic species affects the intensity of an image acquired by MRI.

Some *switches* used to activate (or inactivate) Gd complexes are paramaters of the Solomon Bloembergen equations and include q, τ_R, and τ_M, which were described earlier. Increasing q or τ_R or decreasing τ_M to an optimal value leads to a decrease in T_1 resulting in higher contrast enhancement.

4.2.2.1 PH Sensitive

As reported by Aime et al. [24], Gd complexes with ionisable ligands which are derivatived from 1, 4, 7, 10- tetraazacyclododecane with three acetate oxygens and one phosphonate group on the fourth nitrogen can form ions pairs with poly-aminoacids like polyornithine or polyarginine which makes these entities sensitive to pH. Because pH is an important physiological indicator (as markers for abnormal tissue), many research groups have designed pH sensitive contrast agents. Mikawa et al. [25] developed a MRI contrast agent based on a micro environmental responsive polyion complex in the form of a mixture of two polymers. The complex

exhibits a fifty percent increase in relaxivity upon decreasing pH from 7 to 5. Aime and coworkers [26] have prepared a pH sensitive contrast agent with 30 Gd chelates and 114 ornithine residues. The chelates are conjugated to the amino acid chain via squaric esters. At low pH, the amines are protonated and do not interact with the squaric ester linkers. When the pH rises, the amine side chains become deprotonated and interact with the squaric ester residues. This interaction rigidifies the polymer creating an increase in τ_R, so an increase in relaxivity. Lowe et al. [27] synthesized a DO3A-derivative with sulfonamide nitrogen which at low pH is protonated and unable to chelate the paramagnetic ion. As a result, water access to this ion is restored creating a detectable signal. At a high pH the deprotonated amine chelates prevent water access and the MR signal is low. Hovland et al. [28] have prepared a DO3A compound with a tertiary amine-containing 2 long alkyl chains. When the amine is protonated (pH = 3–6) the relaxivity is low. Upon deprotonation (pH = 8–10), the agents form colloidal aggregates due to the higher lipophilicity. The aggregation causes an increase in τ_R and a subsequent increase in relaxivity. A Gd-DOTA-tetramide derivative has been prepared by Zhang et al. [29]. Its relaxivity increases when pH increases from 4 to 6 but decreases between 6 and 8.5 and is constant between 8.5 and 10.5 and then increases again. This usual pH dependence of the relaxivity could be accounted for by the presence of the uncoordinated phosphonate groups. The proton of the ionisable groups between 9 and 6 can catalyse the exchange of protons between the bound water molecule and the bulk by providing an efficient hydrogen bond network which could be disrupted at lower pH by protonation. Gd-DOTA-tetraamide bearing hydroxypyridyl substituent has exhibited 2 regions of enhanced relaxivity: a small enhancement at lower pH = 2–4 attributed to an increase in the prototropic exchange of the coordinated water molecule and a slightly larger enhancement at higher pH = 6–9 due to deprotonation of the ligand amide protons [30].

Aime et al. [31] have also synthesized a ternary complex between a Gd chelate and carbonate ions. The relaxivity of this complex can be affected by the saturation of its coordination sphere by 2 water molecules or a bidentate ligand such as hydrogenocarbonate. The relaxivity of the complex changes from 7.5 mM^{-1} s^{-1} at low pH to 1.9 mM^{-1} s^{-1} at high pH, reflecting the replacement of 2 water molecules in the first coordination sphere by a carbonate ion.

4.2.2.2 Metal Sensitives

Intracellular calcium plays an important role in muscular contraction, neuronal transduction, hormonal secretion. Li et al. [32, 33] have developed a contrast agent that can specifically detect Ca ions. In the absence of Ca^{2+}, the aromatic aminoacetates interact with the 2 Gd ions. In the presence of Ca^{2+}, the aromatic aminoacetates rearrange to bind Ca allowing water to bind directly to Gd. This increase in q number yields an increase in relaxivity. This mechanism is reversible (Fig. 4.5).

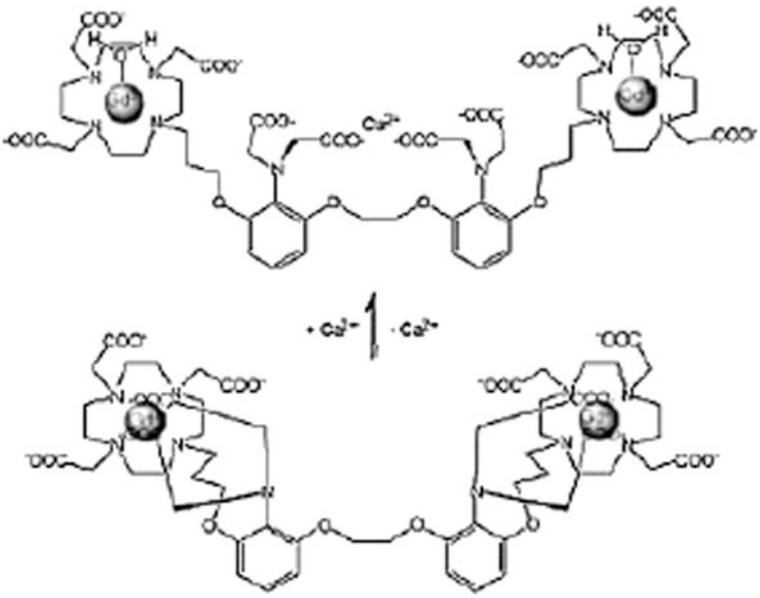

Fig. 4.5 Example for calcium sensitive contrast agent

Nagano et al. [23, 34] have used a similar scheme for detection of zinc ions, with a DTPA ligand coupled with N,N,N′,N′-tetrakis (2-pyridylmethyl)ethylenediamine (TREN) as a zinc specific chelator. Without zinc ion, a water molecule is bound to the gadolinium ion. In the presence of zinc ion, the carboxylic acid and pyridine moieties are coordinated to zinc ion thus restricting the access of the water molecule to the Gd ion. This decrease in q yields a decrease in relaxivity in the presence of zinc.

An iron-sensitive contrast agent was synthesized by Aime et al. [35] by functionalizing DTPA with salicylate moieties. Upon addition of iron (III), the Gd-DTPA-salicylate complexes bind to the iron ions via the salicylate functional groups. This binding yields an increase in τ_R and in relaxivity.

Another iron-sensitive contrast agent was prepared by Comblin and Jacques [36, 37]. DOTA was conjugated to a phenanthroline derivative. Self assembly around iron (II) ions leads to an increase in τ_R and the relaxivity increases from 5.1 to 12.5 mM^{-1} s^{-1}. PhenHDO3A is a ditopic ligand featuring a tetraazacyclododecane unit substituted by three acetate arms and one 6-hydroxy-5,6-dihydro-1, 10-phenanthroline group. This ligand was specially designed so as to obtain highly stable heteropolymetallic assemblies [38]. Costa et al. [39] have developed the same kind of rigid chelates obtained by self-assembly of Fe(II) ions and two terpyridine based Gd-DTTA. $Fe[Gd_2bpy(DTTA)_2(H_2O)_4]_3\}^{4-}$ is a self-assembled, metallostar-structured contrast agent, with six Gd ions confined into a small molecular space. The relaxivity is particularly remarkable at very high magnetic fields (r_1 = 15.8 mM^{-1} s^{-1} at 200 MHz, 37 °C) [40]. Another high-molecular weight

tetrametallic supramolecular complex $[(Ln\text{-}DTPA\text{-}phen)_3Fe]^-$ (Ln = Gd, Eu, La) has been prepared upon self-assembly around one iron (II) ion of three 1,10-phenanthroline-based molecules substituted in 5′-position with the DTPA ligand, $DTPA\text{-}phen^{4-}$ ([41], Fig. 4.6).

4.2.2.3 Enzyme-Activated Contrast Agents

The first enzymatic sensitive contrast agent was reported by Louie et al. [42]; it was developed in response to the need to correlate biological events with gene expression during an imaging experiment. The mechanism is based on 2 distinct relaxation states, a weak and a strong ones. By blocking the one remaining open coordination site, water protons are excluded from the innersphere and the effect of the Gd ions on the relaxivity is diminished. The agent «Egad» was activated by the enzyme β-galactosidase. The enzyme substrate (sugar) occupies all nine coordination sites, inhibiting water access to the Gd ion. The contrast agent is irreversibly turned «on» when β-galactosidase cleaves the sugar and water becomes accessible to the paramagnetic ion, thus modulating q number (Fig. 4.7). These agents have been successfully used in vivo.

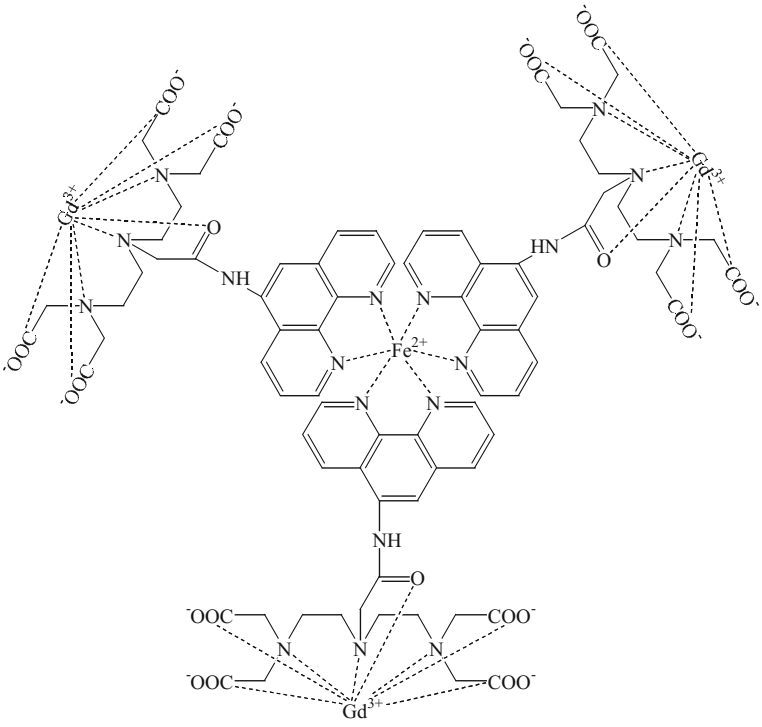

Fig. 4.6 Structure example of iron sensitive contrast agents

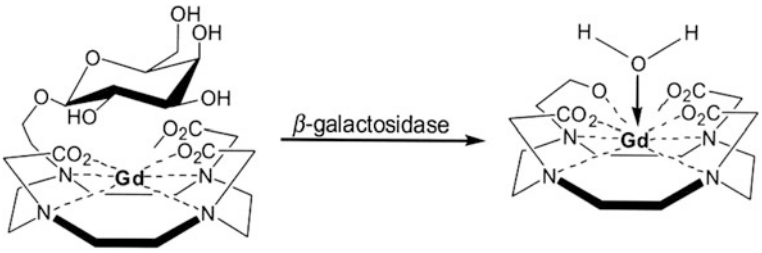

Fig. 4.7 Enzymatic cleavage of the Gd-DOTA derivative with β-galactosidase

Anelli et al. [43] have synthesized a DTPA compound which can detect carbonic anhydrase. The Gd complex contains a sulfonamide group helping to selectively target the enzyme carbonic anhydrase. Upon binding to the enzyme, the relaxivity increases (five fold at 40 MHz).

Nivorozhkin et al. [44] prepared an agent that is sensitive to the presence of human carboxypeptidase B which has been implicated in thrombotic disease. TAFI cleaves a trilysine masking group attached to the agent exposing an aromatic functional group which has a high affinity for human serum albumin. The contrast agent binds HSA leading to an increase in τ_R. This event is known as a receptor induced magnetization enhancement (RIME). The trilysine chain makes this agent a pro-RIME agent because the trilysine chain inhibits interaction with HSA.

Bogdanov et al. [45] prepared a peroxidase activatable agent. This agent consists of a Gd chelate linked to benzene-1,2-diol that acts as a monomer. In the presence of peroxide, the monomers are oligomerized yielding a threefold increase in relaxivity due to an increase of τ_R. This MRI signal amplification can detect peroxidase concentration in vitro and has been used to detect E-selectin expression on human endothelial cells in cell culture by the high local enzymatic activity of antibody bound peroxidase associated with the plasma membrane of these cells.

Duimstra et al. [46] have synthesized a new class of enzyme activated contrast agents using a self immolative mechanism for detection of β-glucuronidase. Querol et al. [47] have prepared new DTPA bisamides. These derivatives bear thyramido or 5-hydroxytryptamido groups that could be oligomerized in situ in the presence of peroxidase/H_2O_2 pair resulting in a net increase in r_1 relaxivity. Chen et al. [48] showed that activatable paramagnetic imaging agents can be used to directly image myeloperoxidase (MPO). Plaque rupture in atherosclerotic disease is the major cause of morbidity and correlates well with MPO secretion by activated macrophages and neutrophils in human. Gd-DOTA-serotonin (3-(2-aminoethyl)-5-hydroxy indole) was efficiently polymerized in the presence of human neutrophil MPO resulting in a 70–100 % increase in proton relaxivity.

4.2.2.4 pO_2

The use of deoxyhemoglobin as MRI contrast agent was discovered by Thulborn et al. [49]. Ogawa et al. [50] have shown that the signal was dependent on the oxygenated state of blood and that the blood oxygen level-dependent (BOLD) signal could be used for noninvasive mapping of human brain function. Activable contrast agents sensitive to the partial pressure of O_2 (pO_2) have been synthesized [51]. The oxidation state of a europium ion is varied to trigger the signal on and off by the environmental pO_2. Eu^{3+} is reduced in Eu^{2+} (isoelectronic with Gd^{3+}) and enhances the observed MR signal upon reduction. Aime et al. [52] have developed a redox switch to increase τ_R as a pO_2 sensitive compound. These complexes use manganese (Mn^{2+}) as the redox ion. By coupling the product to polycyclodextran, the Mn^{2+} porphirin aggregates increasing the Mn^{2+} concentration and τ_R. The water relaxation of Mn^{2+} is much greater than the Mn^{3+} one, creating a redox switch dependent on pO_2. This technique can quantify the oxygen concentration in the surrounding environment.

4.2.3 Specific Contrast Agents for Molecular Imaging

To develop specific contrast agents for molecular imaging, it is necessary to graft molecules targeting receptors overexpressed in pathology.

Contrast agents can be accumulated in a pathological site by passive or active targeting mechanisms. Thanks to the passive targeting, most nanoparticles can be accumulated in tumors due to the pathophysiologic characteristics of the tumor blood vessels [53]. Tumors have higher retention time than normal tissues because tumors lack a well-defined lymphatic system [54, 55]. This can explain an enhanced permeability and retention (EPR) effect.

Active targeting is based on the use of vectorized ligands. A lot of vectors as antibodies, peptides or proteins, aptamers, polysaccharides, … can be grafted to target cellular biomarkers.

MRI contrast agents are used to help in the diagnosis of many diseases (various cancers like breast [56], liver [57], ovarian [58], lung [59], …), however, the agents described so far have the limitation of being non-site specific. The inability to localize selectively in a desired area lessens the diagnostic potential of these agents. The first step toward improving the diagnostic capability of contrast agents is to make them target specific and accumulate in desired biological locations. Many attempts have been made to deliver gadolinium chelates to specific biological targets. An aminooxy-functionalized DTPA derivative that is tumor specific has been synthesized by taking advantage of the fact that tumor cells overexpress sialic acid residues [60]. A DOTA derivative conjugated to the HIV-Tat peptide has the ability to be internalized into many different cell lines unlike unmodified chelates that are not internalized into cells [61]. Liposomes containing gadolinium were conjugated to mouse antibodies and successfully targeted to ICAM-1, an endothelial leukocyte

receptor upregulated on cerebral microvasculature during experimental autoimmune encephalitis [62]. Polylysine labeled with Gd–DTPA and transferrin can image cells expressing the transferrin receptor [63]. Further, this polymer has been modified with an anti-CEA $F(ab')_2$ immunoconjugate to image colorectal carcinoma [64]. Dendrimers labeled with Gd-DTPA have been conjugated to folate and used to successfully image tumor cells which are expressive of the high-affinity folate receptor in mice [65, 66]. Specific, non invasive imaging of angiogenesis in rabbits was accomplished using an antibody to the angiogenesis marker endothelial integrin $\alpha_v\beta_3$ conjugated to gadolinium containing liposomes [67] and perfluorocarbon-nanoparticles [68].

The blood brain barrier (BBB) is one of the most challenging physical hurdles when designing contrast agents intended for the brain. The BBB contains various mechanisms for minimizing the flow of material into and out of the brain [69]. This barrier prevents most passive diffusion except by extremely small molecules such as water and ethanol. Electric charge, lipid solubility, and molecular weight can be used to help predict whether or not a molecule will cross the BBB [70]. Brain tumors have a fenestrated BBB and diseases such as multiple sclerosis involve temporary weakening of the BBB. Gd-DTPA [71, 72], Gd-BOPTA [73], have all been used to image these BBB breakdowns. One recent development in the delivery of contrast agents into the brain involves the conjugation of putrescine (an endogenously occurring polyamine that is known to increase BBB permeability) to a peptide linked to Gd-DTPA. This agent successfully crossed the BBB as predicted [74].

Targeted contrast agents may greatly improve the accuracy and scope of diagnostic imaging.

4.2.4 How to Obtain High Relaxivity with Paramagnetic Gd-Derivatives by Increasing τ_R

Several dinuclear complexes have been envisaged to obtain higher relaxivity [75–77]. Gd-DTPA or Gd-DOTA with large substituents have been studied [78–81]. Port et al. have developed several Gd macrocyclic compounds based on a Gd-DOTA substituted by hydrophilic arms. The structure of P760 [78, 79] and P792 [80–82] has been optimized to obtain a high relaxivity in the field for MRI (P760: 24.7 s^{-1} mM^{-1} at 20 MHz and P792: 29 s^{-1} mM^{-1} at 60 MHz), a high biocompatibility profile and a high molecular volume (Fig. 4.8).

Macromolecules To obtain a better relaxivity, intense research has been carried out in the covalent coupling of contrast agents with macromolecules like polymers, dendrimers, proteins, … First of all, a compromise must be found between the size of the macromolecules (to be eliminated by glomerular filtration) and tolerability in the body. They must be biocompatible and the grafted complexes kinetically stable. Albumin was the first molecule to which Gd-DTPA units were attached [83].

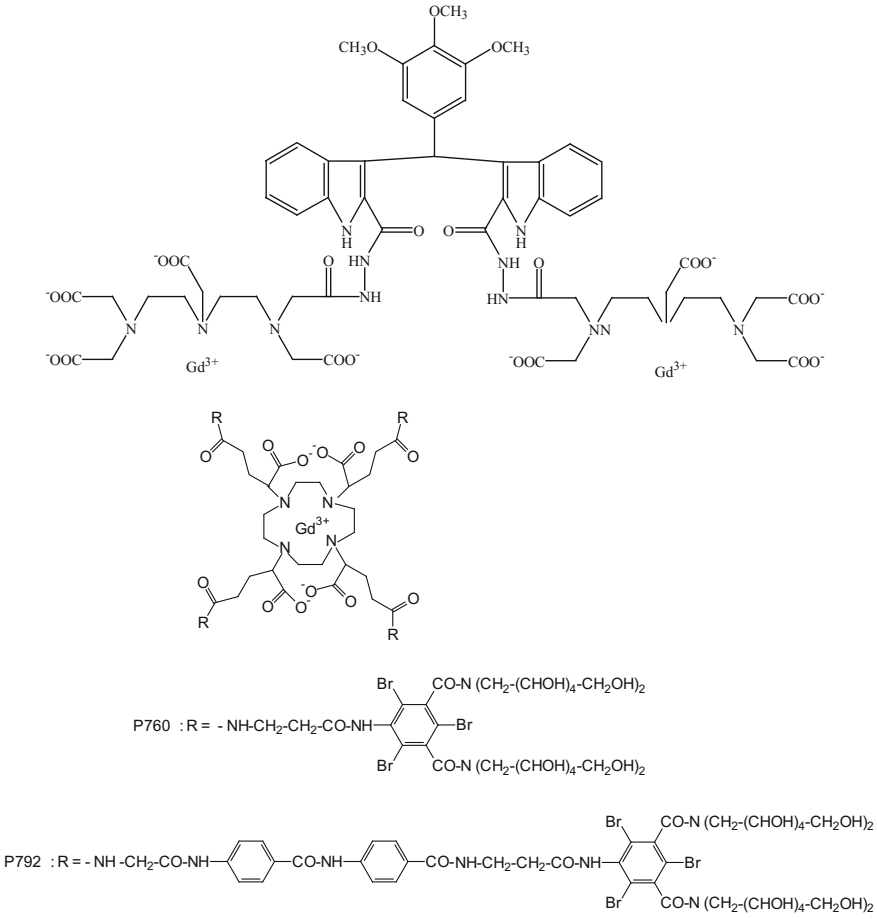

Fig. 4.8 Some examples of Gd-DTPA or Gd-DOTA derivatives with large substituents

Gd-DTPA complexes have also been grafted onto a lysine residue without [84] or in presence of PEG [85] which increases the relaxivity. Gd complexes have been attached to linear polymer chains as side chains [86–89] or incorporated in the linear polymer itself [90]. The relaxivities of these molecules have been found to be lower than expected. This was explained by the highly flexible nature of the macromolecule. Higher efficiency has been obtained for Gd-DTPA-bisamide copolymers, $[(\text{Gd-DTPA-BA})\text{-}(\text{CH2})_n]_x$ (n = 6, 10 or 12) which contain hydrophobic parts in the polymer [91].

Dextran containing a spacer arm was also used [92]. The advantage of dextran is its high capacity for functionalization (carbamate, epichlorhydrine, periodate, carboxymethyl) [93–100].

Several Gd chelates have also been grafted on polysaccaride like inulin [101].

For all these macromolecules, the increase in relaxivity is not as large as predicted by the theory. The macromolecular contrast agent must lead to a slowing of the rotational speed and to an increase in the relaxivity via τ_R. The polymer allows a certain rotational freedom and probably, the movements of the Gd complexes are more rapid than the polymer molecule itself.

Gd-DTPA-polylysine, Gd-DOTA-polylysine, Gd-SCN-Bz-DOTA-polylysine were also investigated [102].

Relaxivity studies indicated that polyaspartamide Gd complexes containing sulfadiazine groups possess higher relaxivities than that of Gd-DTPA. MRI showed that the macromolecular PAEA-Gd-DTPA-SD greatly enhanced the contrast of MR images of hepatoma in the lower limb of mice and prolonged intravascular duration [103]. Most currently macromolecular contrast agents are not biodegradable. Wen et al. [104] have synthesized and characterized poly(glutamic acid) Gd chelates as biodegradable blood pool compounds. Biodegradable macromolecular chelates, Gd-DTPA cystine copolymers were grafted with PEG of different size to modify the physicochemical properties and in vivo MRI contrast enhancement of the agents and to study the effect of PEG chain length (MW = 550, 1000 and 2000) on these properties [105]. PEG 2000 showed more prominent enhancement in the blood pool for a longer period of time. Polydisulfide-based biodegradable polymer Gd complexes have been modified to improve the in vivo retention time and MRI contrast [106].

The Gd complexes have been grafted on PAMAM dendrimers [107–110]. The increase in relaxivity can be explained by the steric hindrance which predominates at the periphery and which produces an increase in τ_R. Relaxivity studies showed that the dendritic Gd complexes possess high efficiency. Dendritic Gd-chelates containing pyridoxamine groups enhanced the contrast of the MR images of the liver, provided prolonged intravascular duration and produced highly contrasted visualization of the blood vessels [111].

Two things have guided the development of contrast agents interacting with HSA: the blood pool compound for angiography and the increase of τ_R for higher relaxivity and so better efficiency. In the last case, two techniques can be used, the covalent (see above) or non-covalent interaction with a macromolecule.

Several ways have been investigated for conjugation of contrast agents to a protein: DTPA bisanhydride as the acylation agent [112–114], DTPA mixed anhydride [86, 115], N-hydroxysuccinic ester [116], squaric acid esters linker [117], isothiocyanatobenzyl groups [89]. The most studied system is represented by albumin labeled with Gd-DTPA. The frequency and temperature dependence of proton and oxygen-17 relaxivities of $(Gd\text{-}DTPA)_{45}$-HSA have been studied [118]. The observed behaviour is typical of systems whose relaxivity is limited by a long exchange lifetime of the coordinated water molecule [119]. Sieving et al. [120] have synthesized a poly-(L-lysine) containing 60–90 chelating groups (DTPA or DOTA). The relative small relaxation enhancement shown by Gd complexes when bound to polylysine is accounted for by the high internal mobility of the paramagnetic moiety. An analogous result was observed by using the squaric acid unit as linker between the macromolecule and the Gd-chelates. Labeling of monoclonal antibodies with Gd-DTPA has also been considered for targeting tumors [64, 121].

The clinical application of Gd chelates grafted with polymers is limited by the slow excretion of the complexes and so the accumulation of toxic Gd. To avoid this problem, biodegradable polydisulfide macromolecular complexes have been prepared based on the disulfide—thiol exchange to allow degradation of the macromolecules by endogenous thiol and facilitate excretion of Gd chelate [122].

Zeolite and tungstosilicates Gd doped zeolite NaY nanoparticles have been envisaged as a contrast agent for MRI [123–125]. The relaxivity of GdNaY increases when the Gd content in the zeotile is decreasing [126]. The relaxivity increases drastically (from 11.4 to 37.7 s^{-1} mM^{-1} at 60 MHz and 37 °C) as Gd loading decreases [127]. Gd sandwiched complexes with tungstosilicates have also been tested in vivo and in vitro [128]. They are favorable candidates for hepatic contrast agents but they exhibit high toxicity and need to be modified before clinical use.

Nanosystems To enhance the relaxivity of Gd complexes, Aime et al. have trapped Gd-HP-DO3A in apoferritin [129]. The relaxivity shown by each Gd complex included in the protein at 20 MHz and 25 °C is very high (about 80 s^{-1} mM^{-1}), value about 20 times higher than the value of the free complex in water.

Novel materials having stronger proton relaxivity and higher signal enhancement have been tested for a new generation of contrast agents. Recently, polyhydroxylated Gd metallofullerenes have been proposed by several groups. The team of Wilson [130, 131] have found $r_1 = 20$ s^{-1} mM^{-1} (20 MHz, 40 °C), Zhang et al. [132] have reported a relaxivity of $r_1 = 47$ mM^{-1} s^{-1} (400 MHz) and Shinohara et al. [133] measured a particularly high proton relaxivity for $Gd@C_{82}(OH)_{40}$ (81 mM^{-1} s^{-1} at 25 °C, 40 MHz). Kato et al. have [134] reported endohedral metallofullerenols $M@C_{82}(OH)_n$ with M = La, Gd, Ce, Dy, Er. The origin of the high relaxivities and the mechanism involved have not been fully elucidated. Recently, Bolskar et al. [135] have obtained the first water soluble $Gd@C_{60}$ derivatives. Toth et al. [136, 137] have reported the physicochemical characterization of $Gd@C_{60}[C(COOH)_2]_{10}$ and $Gd@C_{60}(OH)_x$.

More recently, another way to reach high relaxivity has been opened by use of carbon-nanotubes. Nanowires of magnetic metals (Fe, Gd, Co) have been prepared inside the hollow interiors of single wall nanotubes (SWNTs) by filling SWTNs with precursor metal chlorides and subsequent reduction [138]. A metallofullerene, $Gd@C_{82}$, encapsulated in the inside space of single walled carbon nanotube has been identified as an STM image of a carbon cage and a Gd atom by a measurement of the tunnel currents onto the SWNT surface. This fact indicates that there is a substantial local interaction between the wall of SWNT and the Gd ions close to the wall [139]. In a preliminary study [140], surprisingly high relaxivities (500 s^{-1} mM^{-1} at low frequency and about 180 s^{-1} mM^{-1} at high frequency) have been found. At this time, no theory can explain this observation.

Numerous organic or inorganic nanoparticles for encapsulation of Gd based contrast agents, such as lipid nanoparticles (liposomes, solid lipid nanoparticles, …), silica nanoparticles, dendrimers or polymer nanoparticles have been described.

Liposomes

Liposomes, thanks to their biocompatibility, low toxicity and high structural flexibility are widely used as vehicles for therapeutic and/or diagnostic purposes. Due to their structure, liposomes can encapsulated hydrophilic contrast agents in the hydrophilic compartment or internalize hydrophobic complexes into the membrane.

Encapsulation within the cavity generally led to a decrease in relaxivity, due to the limited interaction between the contrast agent and the surrounding water molecules [141, 142]. For example, encapsulation of Gd-HPDO3A in liposomes causes a decrease in its longitudinal relaxivity of three to nineteen times according to the nature of the lipid used [r_1 = 3.75 mM^{-1} s^{-1} for free Gd-HPDO3A and between 0.2 and 1.1 mM^{-1} s^{-1} for encapsulated (at 25 °C and 20 MHz)] [143]. The incorporation of the functionalized lipid gadolinium chelates in the membrane causes an enhancement of relaxivity, due to a facilitated interaction between the water protons and the gadolinium, and to a lesser free rotation of the gadolinium chelate [141]. For example, the Gd-DOTA functionalized with a phosphoethanolamine (DSPE-GdDOTA) is an integral part of the liposome membrane and has a longitudinal relaxivity of approximately 15 mM^{-1} s^{-1} at 37 °C and 60 MHz [142]. In this way, it is possible to include large amounts of gadolinium chelates. For example, 34,000 gadolinium centers could be incorporated into the bilayer of liposomes of 100 nm diameter [142]. To gain relaxivity, it is also possible to optimize the size, permeability and organization of the liposome membrane [144]. Thus, liposomes prepared from Gd-DTPA-BSA and Gd-DOTA-DSPE did not give the same results in terms of efficiency (respectively r_1 = 7.5 and 12.8 mM^{-1} s^{-1} at 37 °C and 60 MHz) and proton exchange rate (respectively τ_M = 1200 and 250 ns) while Gd-DTPA and Gd-DOTA exhibit similar values. This difference in behavior is explained by a difference in orientation of the polar heads at the liposome/water interface. Indeed, in Gd-DTPA-BSA, Gd-DTPA is at the interface and BSA is the amphiphilic tail. In contrast, in the case of Gd-DOTA-DSPE, the phosphate moiety is placed at the interface and Gd-DOTA is removed from the rest of the nanoparticle to the aqueous medium [145] (Fig. 4.9).

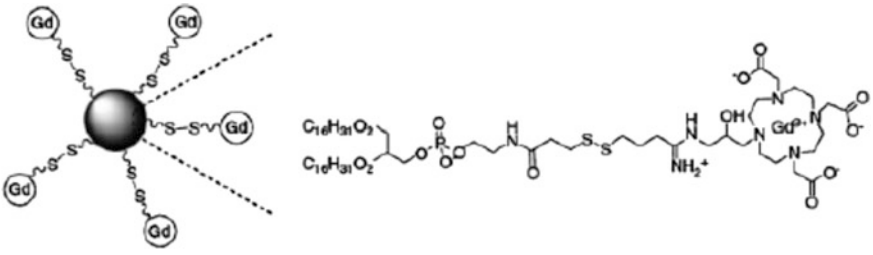

Fig. 4.9 Example of Gd complexes conjugated to phospholipids in liposomes [146]

Polymers

Nanocapsules or nanospheres can encapsulate or adsorb contrast agents. PLGA nanoparticles were tested for encapsulating commercial contrast agents. If the encapsulation of T_2 agents was successfully observed, the results obtained for T_1 agents were worse than what was hoped [147, 148]. The incompatibility between the hydrophobic matrix and contrast agent induced premature release and a restriction of exchange between the water molecules and the Gd ion. For these reasons, when the polymer matrix is hydrophobic, the exaltation of the relaxivity of the paramagnetic agent proceeds rather by its grafting to the surface of the nanoparticle than by its containment. Surface functionalization of the PLGA nanoparticles with gadolinium complexes allows to observe a relaxivity gain of approximately three to four times that of the free agent (483). It is possible to optimize the gain by varying the length or the architecture of the spacer group linking the chelate to the nanoparticle. Thus, when the Gd-DTPA and Gd-DOTA are grafted on the surface of PLGA nanoparticles via a spacer of polyethyleneimine type (PEI), their relaxivity is increased up to approximately 17 mM^{-1} s^{-1} (as compared to 4 for the free complex) at 25 °C and 60 MHz.

An improvement in relaxivity per Gd center can be achieved by containment of contrast agents in hydrogels formed from hydrophilic polymers as chitosan. The longitudinal and transverse relaxivities of Gd-DOTA may be increased to achieve respective values of r_1 = 72.3 mM^{-1} s^{-1} and r_2 = 177.5 mM^{-1} s^{-1} (37 °C, 60 MHz) [149]. It is the same for the Gd-DOTP (r_1 = 98 mM^{-1} s^{-1} and r_2 = 109.5 mM^{-1} s^{-1} at 37 °C, 20 MHz) [150]. The results confirm a relaxivity exalted by Gd center via second sphere mechanisms.

Other types of polymeric nanoparticles are able of increasing the relaxivity of Gd complexes. For example, dendrimers can incorporate several contrast agents, increasing the longitudinal relaxivity r_1 of the Gd-DTPA from 5 mM^{-1} s^{-1} to values between 20 and 30 mM^{-1} s^{-1} for Gd-DTPA associated with dendrimers (between 0.5 and 1.5 T at 37 °C) [151].

Inorganic nanoparticles

Wartenberg et al. have significantly increased the relaxivity of Gd-(ebpatcn) simply by incorporation into silica nanoparticles via the sol-gel process. Thus the relaxivity of encapsulated Gd chelates (encapsulated r_1 = 84 mM^{-1} s^{-1} at 25 °C and 45 MHz) is 18 times greater than that of the free Gd complexes (r_1 = 4.7 mM^{-1} s^{-1} at 25 °C and 45 MHz) [152]. The decrease in relaxivity observed when the nanoparticles increase in size is explained by a larger charging rate of contrast agent hindering movement of water molecules and thus reducing exchanges.

Other systems based on the confinement of Gd complexes have allowed a significant increase of the relaxivity values. This is the case, for example, with Gd-fullerenes, Gd-zeolites or complexes of Gd (III) included in the cavity of the apoferritin [153–155].

The gadofullerenes consist of a carbon cage (produced by electric arc from composite materials Gd/graphite) enclosing one or more Gd ions. In this cage, the Gd^{3+} ions have their movement slowed and the presence of hydroxyl groups on the surface of fullerene promotes exchanges with the surrounding water molecules. Relaxivity can then be increased by approximately 10–40 times compared to commercial Gd complexes [153, 155].

Zeolites are microporous aluminosilicate crystals in which the ion Gd^{3+} can be fixed. Relaxivity can reach between 20 and 40 mM^{-1} s^{-1} which is better than the commercial contrast agents but remains far from the theoretical maximum. This moderate increase can be explained by the low diffusion of water molecules through the pores [155].

Finally improved relaxivity is greater when the contrast agent is confined rather than bound to the nanoparticle, provided that the structure thereof is permeable to water molecules. When both conditions are met, relaxivity values close to the theoretical maximum can be reached (100 mM^{-1} s^{-1} at 25 °C and 20 MHz). This is explained by the fact that the confinement of the Gd chelate in the particle limits the free rotation but also that of water molecules therein, moderating indeed anarchic reorientation of Gd–H_2O vectors. When the Gd complex is bound to the particle by a covalent bond, the nanoparticle minimizes the overall rotation of the building but local rotational movement of the chelates, at their covalent bond with the nanoparticle structure, remains. This results in an enhancement of relaxivity but this increase is limited.

4.2.5 PARACEST Agents

Another class of activatable lanthanide based agents makes use of a chemical exchange saturation transfer (CEST) event as the "switch" [156] (Fig. 4.10).

Conventional low-molecular weight, extracellular, Gd^{3+}-based contrast agents enter the extracellular space and highlight only those tissue regions that temporally accumulate the paramagnetic complex. This accumulation of paramagnetic complex results in a shortening of the bulk water spin-lattice relaxation time (T_1) and hence brightening of the image in that region. This mechanism of altering bulk water relaxation cannot be controlled externally and hence one cannot modulate (turn on/off) the relaxation effects of a T_1 shortening agent; one can only compare image intensities pre- and post injection of the agent.

There has been considerable effort to engineer Gd^{3+}-based complexes with substantially higher relaxivities, but it is not always easy. As shown before, one of the ways to gain a substantial increase in relaxivity is to slow rotation of Gd^{3+} complexes by attachment to a larger structure such as biopolymer, a nanoparticle, or a naturally occurring polymer like albumin.

As an alternative to T_1 shortening agents for MR contrast enhancement, one could also introduce contrast by altering the proton density or total water signal detected. This can be accomplished using a NMR technique called magnetization

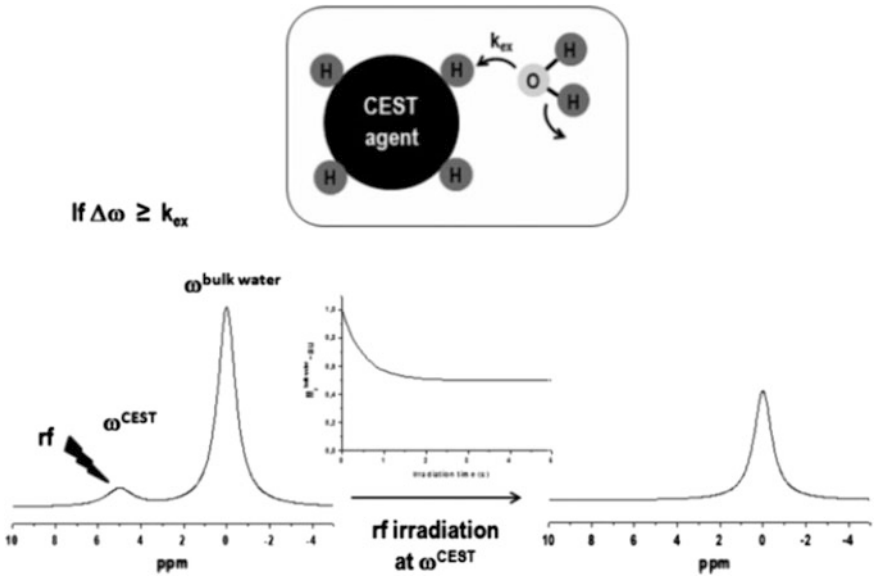

Fig. 4.10 Schematic view of the saturation transfer mediated by chemical exchange. The plot reported on the *arrow* indicates the dependence of the bulk water magnetization on the irradiation time [172]

transfer (MT). Ward et al. [157, 158] introduced the idea of using the MT effect to induce contrast into an image and proposed a new class of MRI contrast agent based on chemical exchange saturation transfer (CEST) between intrinsic metabolites like amino acids, sugars, nucleotides or other heterocycles having exchangeable OH or NH groups that exchange protons with bulk water. They demonstrated using simple diamagnetic molecules that MRI contrast can be switched on/off by applying a saturating irradiation pulse at an exchangeable site a few ppm away from the bulk water resonance. CEST agents take advantage of the difference in proton chemical shift between the amide proton and the innersphere water protons of the contrast agent. Aime et al. [159–161] and Zhang et al. [162–166] have used this kind of CEST agents. The concentration dependence is avoided by using two different exchange sites within a contrast agent, as in the OH and NH bonds. When external RF is directed at the frequency of one of the proton pool resonances, this causes saturation transfer to the water resonances and decreases the bulk water intensity, allowing for external manipulation of the signal intensity. Aimé et al. [167] have shown that Yb complex can be sensitive to biological substrates such as lactate. The free Yb complex and the lactate bound complex have two different sets of amide frequencies to irradiate. The concentration in lactate can be determined by irradiating the amide protons of the unbound complex. Aime et al. have [167] also developed a pH sensitive CEST agent, a Yb-DOTA-tetraglycineamide complex. Saturation of the amide protons that are in close proximity to the paramagnetic center results in an excellent CEST agent. The

observed effect is pH-dependent since the exchange rate for amide protons is pH modulated. By irradiating the amide N–H resonances, saturation transfer to the water resonance occurs, leading to a decrease in the water signal intensity which determines the contrast in MRI. Several strategies have been developed for improving the activity of CEST agents: to increase the number of mobile proton per molecule [168, 169] or to increase the chemical shift difference between the exchangeable protons and the bulk water with paramagnetic shift reagents interacting with the diamagnetic system bearing the mobile protons [170]. This CEST method can be use with liposomes that intrap a paramagnetic shift complex [171]. This system called Lipocest, allows a very low detection limit and opens the possibility of use in the field of magnetic molecular imaging.

References

1. Krause W (2002) Topics in current chemistry. Contrast agents II: optical, ultrasound, X-ray and radiopharmaceutical imaging. Springer, Berlin
2. Caravan P, Ellison JJ, McMurry TJ (1999) Gadolinium(III) chelates as MRI contrast agents: structure, dynamics, and applications. Chem Rev 99:2293–2352
3. Laurent S, Henoumont C, Vander Elst L, Muller RN (2012) Synthesis and physicochemical characterisation of Gd-DTPA derivatives as contrast agents for MRI. Eur J Inorg Chem 12:1889–1915
4. Aime S, Fasano M, Terreno E (1998) Lanthanide(III) chelates for NMR biomedical applications. Chem Soc Rev 27:19–29
5. Vander Elst L, Maton F, Laurent S et al (1997) A multinuclear MR study of Gd-EOB-DTPA: comprehensive preclinical characterization of an organ specific MRI contrast agent. Magn Reson Med 38:604–614
6. Uggeri F, Aime S, Anelli PL et al (1995) Novel contrast agents for magnetic resonance imaging. Synthesis and characterization of the ligand BOPTA and its Ln(III) complexes (Ln = Gd, La, Ln). X-ray structure of disodium (TPS-9-145337286-C-S)-[4-carboxy-5,8,11-tris(carboxymethyl)-1-phenyl-2-oxa-5,8,11-triazatridecan-13-oato(5-)] gadolinite (2-) in a mixture with its enantiomer. Inorg Chem 34:633–642
7. Muller RN, Raduchel B, Laurent S et al (1999) Physicochemical characterization of MS-325, a new gadolinium complex, by multinuclear relaxometry. Eur J Inorg Chem 11:1949–1955
8. Bloembergen N, Morgan LO (1961) Proton relaxation times in paramagnetic solutions. Effects of electron spin relaxation. J Chem Phys 34(3):842
9. Solomon I (1955) Relaxation processes in a system of two spins. Phys Rev 99(2):559–565
10. Freed JH (1964) Anisotropic rotational diffusion and electron spin resonance linewidths. J Chem Phys 41:2077
11. Hwang L-P, Freed JH (1975) Generalized Einstein relations for rotational and translational diffusion of molecules including spin. J Chem Phys 63:118
12. Bloembergen N (1957) J Chem Phys 27:573–575
13. Kimmich R, Anoardo E (2004) Field-cycling NMR relaxometry. Progr Nuclear Magn Reson Spectroscopy 44:257–320
14. Merbach AE, Helm L, Toth E (eds) (2013). The chemistry of contrast agents in medical magnetic resonance imaging. Wiley, USA, pp 25–81 (Chapter 2)

15. Laurent S, Vander Elst L, Muller RN (2006) Comparative study of the physicochemical properties of six clinical low molecular weight gadolinium contrast agents. Contrast Med Mol Imaging 1(3):128–137
16. Vander Elst L, Raynal I, Port M et al (2005) In vitro relaxometric and luminescence characterization of P792 (Gadomelitol, Vistarem) an efficient and rapid clearance blood pool MRI contrast agent. Eur J Inorg Chem 15:1142–1148
17. Vander Elst L, Port M, Raynal I et al (2003) Physicochemical characterization of p760, a new macromolecular contrast agent with high relaxivity. Eur J Inorg Chem 13:2495–2501
18. Lu Z-R, Mohs AM, Zong Y, Feng Y (2006) Polydisulfide Gd(III) chelates as biodegradable macromolecular magnetic resonance imaging contrast agents. Int J Nanomed 1:31–40
19. Woods M, Zhang S, Ebron VH, Sherry AD (2003) pH sensitive modulation of the second hydration sphere in lanthanide(III) Tetraamide-DOTA complexes; a novel approach to smart MR contrast media. Chemistry 9:4634–4640
20. Lindner L, Reinl HM, Schlemmer M, Stahl R, Peller M (2005) Paramagnetic thermosensitive liposomes for MR-thermometry. Int J Hyperth 21:575–588
21. Aime S, Digilio G, Fasano M et al (1999) Metal complexes as allosteric effectors of human hemoglobin: an NMR study of the interaction of the gadolinium(III) bis(m-boroxyphenylamide) diethylenetriaminepentaacetic acid complex with human oxygenated and deoxygenated hemoglobin. Biophys J 76:2735–2743
22. Shiftan L, Neeman M (2006) Kinetic analysis of hyaluronidase activity using a bioactive MRI contrast agent. Contrast Med Mol Imaging 1:106–112
23. Hanaoka K, Kikuchi K, Urano Y et al (2002) Design and synthesis of a novel magnetic resonance imaging contrast agent for selective sensing of zinc ion. Chem Biol 9:1027–1032
24. Aime S, Botta M, Garino E et al (2000) Non-covalent conjugates between cationic polyamino acids and Gd^{III} chelates: a route for seeking accumulation of MRI-contrast agents at tumour targeting sites. Chem Eur J 6(14):2609–2617
25. Mikawa M, Miwa N, Brautigam M et al (1998) A pH-sensitive contrast agent for functional magnetic resonance imaging (MRI). Chem Lett, pp 693–694
26. Aime S, Botta M, Geninatti Crich S et al (1999) A macromolecular Gd(III) complex as pH-responsive relaxometric probe for MRI applications. Chem Commun, pp 1577–1578
27. Lowe MP, Parker D, Reany O et al (2001) pH-dependent modulation of relaxivity and luminescence in macrocyclic gadolinium and europium complexes based on reversible intramolecular sulfonamide ligation. J Am Chem Soc 123:7601–7609
28. Gløgård C, Hovland R, Fossheim SL et al (2000) Synthesis and physicochemical characterisation of new amphiphilic gadolinium DO3A complexes as contrast agents for MRI. J Chem Soc Perkin Trans 2:1047–1052
29. Zhang S, Wu K, Sherry AD (1999) A novel pH-sensitive MRI contrast agent. Angew Chem Int Ed Engl 38:3192–3194
30. Woods M, Zhang S, Ebron VH, Sherry AD (2003) pH-Sensitive modulation of the second hydration sphere in lanthanide(III) tetraamide-DOTA complexes: a novel approach to smart MR contrast media. Chemistry 9(19):4634–4640
31. Aime S, Barge A, Botta M et al (1999) Dependence of the relaxivity and luminescence of gadolinium and europium amino-acid complexes on hydrogencarbonate and pH. Chem Commun, pp 1047–1048
32. Li W-H, Parigi G, Fragai M et al (2002) Mechanistic studies of a calcium dependent MRI contrast agents. Inorg Chem 41:4018–4024
33. Li W-H, Fraser SE, Meade TJ (1999) A calcium-sensitive magnetic resonance imaging contrast agent. J Am Chem Soc 121:1413–1414
34. Hanaoka K, Kikuchi K, Urano Y, Nagano T (2001) Selective sensing of zinc ions with a novel magnetic resonance imaging contrast agents. J Chem Soc (Perkin 1) 2:1840–1843
35. Aime S, Botta M, Fasano M, Terreno E (1993) Gd(III)–Fe(III) heterobimetallic complexes of DTPA-bis-salicylamide. Spectrochim Acta 49A:1315–1322
36. Comblin V, Gilsoul D, Hermann M et al (1999) Designing new MRI contrast agents: a coordination chemistry challenge. Coord Chem Rev 185–186:451–470

37. Jacques V, Desreux JF (2002) New classes of MRI contrast agents. Top Curr Chem 221:123–164
38. Paris J, Gameiro C, Humblet V et al (2006) Auto-assembling of ditopic macrocyclic lanthanide chelates with transition-metal ions. Rigid multimetallic high relaxivity contrast agents for magnetic resonance imaging. Inorg Chem 45(13):5092–5102
39. Costa J, Ruloff R, Burai L, Helm L, Merbach AE (2005) Rigid MIIL2Gd2III (M = Fe, Ru) complexes of a terpyridine-based heteroditopic chelate: a class of candidates for MRI contrast agents. J Am Chem Soc 127(14):5147–5157
40. Livramento JB, Weidensteiner C, Prata MIM et al (2006) First in vivo MRI assessment of a self-assembled metallostar compound endowed with a remarkable high field relaxivity. Contrast Med Mol Imaging 1(1):30–39
41. Parac-Vogt TN, Vander Elst L, Kimpe K et al (2006) Pharmacokinetic and in vivo evaluation of a self-assembled gadolinium(III)–iron(II) contrast agent with high relaxivity. Contrast Med Mol Imaging 1(6):267–278
42. Louie AY, Huber MM, Ahrens ET et al (2000) In vivo evaluation of gene expression using magnetic resonance imaging. Nat Biotechnol 18:321–325
43. Anelli PL, Bertini I, Fragai M et al (2000) Sulfonamide-functionalized gadolinium DTPA complexes as possible contrast agents for MRI: a relaxometric investigation. Eur J Inorg Chem, pp 625–630
44. Nivorozhkin AL, Kolodziej AF, Caravan P et al (2001) Enzyme-activated Gd(3+) magnetic resonance imaging contrast agents with a prominent receptor-induced magnetization enhancement. Angew Chem Int Ed 40:2903–2906
45. Bodganov A, Matuszewski L, Bremer C, Petrovsky A, Weissleder R (2002) Oligomerization of paramagnetic substrates result in signal amplification and can be used for MR imaging of molecular targets. Mol Imaging 1:16–23
46. Duimstra JA, Femia FJ, Meade TJ (2005) A gadolinium chelate for detection of beta-glucuronidase: a self-immolative approach. J Am Chem Soc 127(37):12847–12855
47. Querol M, Chen JW, Weissleder R, Bogdanov A Jr (2005) DTPA-bisamide-based MR sensor agents for peroxidase imaging. Org Lett 7(9):1719–1722
48. Chen JW, Pham W, Weissleder R, Bogdanov A Jr (2004) Human myeloperoxidase: a potential target for molecular MR imaging in atherosclerosis. Magn Reson Med 52(5):1021–1028
49. Thulborn KR, Waterton JC, Matthews PM, Radda GK (1982) Oxygenation dependence of the transverse relaxation time of water protons in whole blood at high field. Biochem Biophys Acta 714:265–270
50. Ogawa S, Tank DW, Menon R et al (1992) Intrinsic signal changes accompanying sensory stimulation: functional brain mapping with magnetic resonance imaging. Proc Natl Acad Sci USA 89:5951–5955
51. Burai L, Scopelliti R, Toth E (2002) EuII-cryptate with optimal water exchange and electronic relaxation: a synthon for potential pO2 responsive macromolecular MRI contrast agents. Chem Commun 20:2366–2367
52. Aime S, Botta M, Gianolio E, Terreno E (2000) A p(O(2))-responsive MRI contrast agent based on the redox switch of manganese(II/III)—porphyrin complexes. Angew Chem Int Ed Engl 39:747–750
53. Jones A, Harris AL (1998) New developments in angiogenesis: a major mechanism for tumor growth and target for therapy. Cancer J Sci Am 4:209–217
54. Allen TM, Cullis PR (2004) Drug delivery systems: entering the mainstream. Science 303:1818–1822
55. Byrne JD, Betancourt T, Brannon-Peppas L (2008) Active targeting schemes for nanoparticle systems in cancer therapeutics. Adv Drug Deliv Rev 60:1615–1626
56. Brown J, Buckley D, Coulthard A et al (2000) Magnetic resonance imaging screening in women at genetic risk of breast cancer: imaging and analysis protocol for the UK multicentre study. UK MRI breast screening study advisory group. Magn Reson Imaging 18:765–776

57. Yu J-S, Ki WK, Park M-S, Yoon S-W (2002) Transient peritumoral enhancement during dynamic MRI of the liver: cavernous hemangioma versus hepatocellular carcinoma. J Comput Assist Tomogr 26:411–417
58. Konda SD, Aref M, Wang S et al (2001) Specific targeting of folate–dendrimer MRI contrast agents to the high affinity folate receptor expressed in ovarian tumor xenografts. Magn Reson Mater Phys Biol Med 12:104–113
59. Hunter GJ, Hamberg LM, Choi N et al (1998) Dynamic T1-weighted magnetic resonance imaging and positron emission tomography in patients with lung cancer: correlating vascular physiology with glucose metabolism. Clin Cancer Res 4:949–955
60. Lemieux GA, Yarema KJ, Jacobs CL et al (1999) Exploiting differences in sialoside expression for selective targeting of MRI contrast reagents. J Am Chem Soc 121:4278–4279
61. Bhorade R, Weissleder R, Nakakoshi T et al (2000) Macrocyclic chelators with paramagnetic cations are internalized into mammalian cells via a HIV-tat derived membrane translocation peptide. Bioconjugate Chem 11:301–305
62. Sipkins DA, Gijbels K, Tropper FD et al (2000) ICAM-1 expression in autoimmune encephalitis visualized using magnetic resonance imaging. J Neuroimmunol 104:1–9
63. Kayyem JF, Kumar RM, Fraser SE, Meade TJ (1995) Receptor targeted co-transport of DNA and magnetic resonance agents. Chem Biol 2:615–620
64. Curtet C, Maton F, Havet T et al (1998) Polylysine-Gd-DTPAn and polylysine-Gd-DOTAn coupled to anti-CEA F(ab′)2 fragments as potential immunocontrast agents. Relaxometry, biodistribution, and magnetic resonance imaging in nude mice grafted with human colorectal carcinoma. Invest Radiol 33:752–761
65. Wiener EC, Konda S, Shadron A et al (1997) Targeting dendrimer-chelates to tumors and tumor cells expressing the high-affinity folate receptor. Invest Radiol 32:748–754
66. Konda SD, Aref M, Brechbiel M, Wiener EC (2000) Development of a tumor-targeting MR contrast agent using the high-affinity folate receptor: work in progress. Invest Radiol 35:50–57
67. Sipkins DA, Cheresh DA, Kazemi MR et al (1998) Detection of tumor angiogenesis in vivo by alphaVbeta3-targeted magnetic resonance imaging. Nat Med 4:623–626
68. Anderson SA, Rader RK, Westlin WF et al (2000) Magnetic resonance contrast enhancement of neovasculature with alpha(v)beta(3)-targeted nanoparticles. Magn Reson Med 44:433–439
69. Tweedle MF, Kumar K (1999) Top Biol Inorg Chem 2:1–43
70. Abbott NJ, Chugani DC, Zaharchuk G et al (1999) Delivery of imaging agents into brain. Adv Drug Deliv Rev 37:253–277
71. Pardridge WM (1997) Drug delivery to the brain. J Cereb Blood Flow Metab 17:713–731
72. Horsfield MA, Rocca MA, Cercignani M, Filippi M (2000) Activity revealed in MRI of multiple sclerosis without contrast agent. A preliminary report. Magn Reson Imaging 18:139–142
73. Baleriaux D, Colosimo C, Ruscalleda J et al (2002) Magnetic resonance imaging of metastatic disease to the brain with gadobenate dimeglumine. Neuroradiology 44:191–203
74. Poduslo JF, Wengenack TM, Curran GL et al (2002) Molecular targeting of Alzheimer's amyloid plaques for contrast-enhanced magnetic resonance imaging. Neurobiol Dis 11:315–329
75. Parac-Vogt TN, Kimpe K, Laurent S et al (2005) Synthesis, characterization, and pharmacokinetic evaluation of a potential MRI contrast agent containing two paramagnetic centers with albumin binding affinity. Chem Eur J 11:3077–3086
76. Costa J, Toth E, Helm L, Merbach AE (2005) Dinuclear, bishydrated Gd(III) polyaminocarboxylates with a rigid xylene core display remarkable proton relaxivities. Inorg Chem 44 (13):4747
77. Nicolle GM, Yerly F, Imbert D et al (2003) Towards binuclear polyaminocarboxylate MRI contrast agents? Spectroscopic and MD study of the peculiar aqueous behavior of the LnIII chelates of OHEC (Ln = Eu, Gd, and Tb): implications for relaxivity. Chemistry 9(22):5453

78. Corot C, Port M, Raynal I et al (2000) Physical, chemical, and biological evaluations of P760: a new gadolinium complex characterized by a low rate of interstitial diffusion. J Magn Reson Imaging 11(2):182–191
79. Vander Elst L, Port M, Raynal I et al (2003) Physicochemical characterization of P760, a new macromolecular contrast agent with high relaxivity. Eur J Inorg Chem 2495–2501
80. Port M, Corot C, Rousseaux O et al (2001) P792: a rapid clearance blood pool agent for magnetic resonance imaging: preliminary results. Magma. 12(2–3):121
81. Port M, Corot C, Raynal I et al (2001) Physicochemical and biological evaluation of P792, a rapid-clearance blood-pool agent for magnetic resonance imaging. Inverst Radiol 36(8):445
82. Vander Elst L, Raynal I, Port M, et al (2005) In vitro relaxometric and luminescence characterization of P792 (Gadomelitol, Vistarem®), an efficient and rapid clearance blood pool MRI contrast agent. Eur J Inorg Chem, pp 1142–1148
83. Mosseley ME, White DL, Wang SC et al (1989) Vascular mapping using albumin-(Gd-DTPA), an intravascular MR contrast agent, and projection MR imaging. J Comput Assist Tomogr 13:215–221
84. Vexler VS, Clement O, Schmitt-Willich H, Brash RC (1994) Effect of varying the molecular weight of the MR contrast agent Gd-DTPA-polylysine on blood pharmacokinetics and enhancement patterns. J Magn Reson Imaging 4:381–388
85. Bogdanov AA, Weissleder R, Frank HW et al (1993) A new macromolecule as a contrast agent for MR angiography: preparation, properties, and animal studies. Radiology 87:701–706
86. Sieving PF, Watson AD, Rocklage SM (1990) Preparation and characterization of paramagnetic polychelates and their protein conjugates. Bioconjugate Chem 1:65–71
87. Schuhmann-Giampieri G, Schmitt-Willich H, Frenzel T et al (1991) In vivo and in vitro evaluation of Gd-DTPA-polylysine as a macromolecular contrast agent for magnetic resonance imaging. Invest Radiol 26:969–974
88. Desser T, Rubin D, Muller H et al (1994) Dynamics of tumor imaging with Gd-DTPA-polyethylene glycol polymers: dependence on molecular weight. J Magn Reson Imaging 4:467–472
89. Aime S, Botta M, Geninatti Crich S et al (1999) Novel paramagnetic macromolecular complexes derived from the linkage of a macrocyclic Gd(III) complex to polyamino acids through a squaric acid moiety. Bioconjugate Chem 10:192–199
90. Toth E, van Uffelen I, Helm L et al (1998) Gadolinium-based linear polymer with temperature independent proton relaxivities: a unique interplay between the water exchange and the rotational contribution. Magn Reson Chem 36:S125–S134
91. Toth E, Helm L, Kellar KE, Merbach AE (1999) Gd(DTPA-bisamide)alkyl copolymers: a hint for the formation of MRI contrast agents with very high relaxivity. Chem Eur J 5:1202–1211
92. Rougued P, Klaveness J (1991) Water-soluble polysaccharides as carriers of paramagnetic contrast agents for magnetic resonance imaging: synthesis and relaxation properties. Carbohydrate Res 214:315–323
93. Bligh SWA, Harding CT, Sadler PJ et al (1991) Use of paramagnetic chelated metal derivatives of polysaccharides and spin-labeled polysaccharides as contrast agents in magnetic resonance imaging. Magn Reson Med 17:516–532
94. Li KCP, Quisling RG, Armitage FE et al (1992) In vivo MR evaluation of Gd-DTPA conjugated to dextran in normal rabbits. Magn Reson Imaging 10:439–444
95. Meyer D, Schaefer M, Bouillot A et al (1991) Paramagnetic dextrans as magnetic resonance contrast agents. Invest Radiol 26(Suppl 1):S60–S64
96. Meyer D, Schaefer M, Chambon C, Beauté S (1994) Paramagnetic dextrans as magnetic resonance blood pool tracers. Invest Radiol 29:S90–S92
97. Corot C, Schaefer M, Beauté S et al (1997) Physical, chemical and biological evaluations of CMD-A2-Gd-DOTA. A new paramagnetic dextran polymer. Acta Radiol 412(Suppl):91–99

98. Casali C, Janier M, Canet E et al (1998) Evaluation of Gd-DOTA-labeled dextran polymer as an intravascular MR contrast agent for myocardial perfusion. Acad Radiol 5(Suppl 1): S214–S218
99. Rebizak R, Schaefer M, Dellacherie E (1999) Macromolecular contrast agents for magnetic resonance imaging. Influence of polymer content in ligand on the paramagnetic properties. Eur J Pharm Sci 7:243–248
100. Sirlin CB, Vera DR, Corbeil JA et al (2004) Gadolinium-DTPA-dextran: a macromolecular MR blood pool contrast agent. Acad Radiol 11(12):1361–1369
101. Lebduskova P, Kotek J, Hermann P et al (2004) A gadolinium(III) complex of a carboxylic-phosphorus acid derivative of diethylenetriamine covalently bound to inulin, a potential macromolecular MRI contrast agent. Bioconjugate Chem 15(4):881–889
102. Uzgiris EE, Cline H, Moasser B et al (2004) Conformation and structure of polymeric contrast agents for medical imaging. Biomacromolecules 5(1):54–61
103. Yan GP, Liu ML, Li LY (2005) Polyaspartamide gadolinium complexes containing sulfadiazine groups as potential macromolecular MRI contrast agents. Bioconjugate Chem 16(4):967–971
104. Wen X, Jackson EF, Price RE et al (2004) Synthesis and characterization of poly(L-glutamic acid) gadolinium chelate: a new biodegradable MRI contrast agent. Bioconjugate Chem 15 (6):1408–1415
105. Mohs AM, Zong Y, Guo J, Parker DL, Lu ZR (2005) PEG-g-poly(GdDTPA-co-L-cystine): effect of PEG chain length on in vivo contrast enhancement in MRI. Biomacromolecules 6 (4):2305–2311
106. Zong Y, Wang X, Goodrich KC et al (2005) Contrast-enhanced MRI with new biodegradable macromolecular Gd(III) complexes in tumor-bearing mice. Magn Reson Med 53(4):835–842
107. Laus S, Sour A, Ruloff R et al (2005) Rotational dynamics account for pH-dependent relaxivities of PAMAM dendrimeric, Gd-based potential MRI contrast agents. Chemistry 11 (10):3064–3076
108. Wang SJ, Brechbiel M, Wiener EC (2003) Characteristics of a new MRI contrast agent prepared from polypropyleneimine dendrimers, generation 2. Invest Radiol 38(10):662–668
109. Kobayaski H, Kawamoto S, Saga T et al (2001) Positive effects of polyethylene glycol conjugation to generation-4 polyamidoamine dendrimers as macromolecular MR contrast agents. Magn Reson Med 46(4):781–788
110. Bryant LH, Brechbiel MW, Wu C et al (1999) Synthesis and relaxometry of high-generation (G = 5, 7, 9, and 10) PAMAM dendrimer-DOTA-gadolinium chelates. J Magn Reson Imaging 9(2):348–352
111. Yan GP, Hu B, Liu ML, Li LY (2005) Synthesis and evaluation of gadolinium complexes based on PAMAM as MRI contrast agents. J Pharm Pharmacol 57(3):351–357
112. Hnatowich DJ, Layne WW, Childs RL et al (1983) Radioactive labeling of antibody: a simple and efficient method. Science 220:515–613
113. Lauffer RB, Brady TJ (1985) Preparation and water relaxation properties of proteins labeled with paramagnetic metal chelates. Magn Reson Imag 3:11–16
114. Ogan MD, Schmiedl U, Moseley M et al (1987) Albumin labeled with Gd-DTPA. An intravascular contrast-enhancing agent for magnetic resonance blood pool imaging: preparation and characterization. Invest Radiol 22:665–671
115. Maisano F, Gozzini L, de Haen C (1992) Coupling of DTPA to proteins: a critical analysis of the cyclic dianhydride method in the case of insulin modification. Bioconjugate Chem 3:212–217
116. Spanoghe M, Lanens D, Dommisse R (1992) Proton relaxation enhancement by means of serum albumin and poly-L-lysine labeled with DTPA-Gd3+: relaxivities as a function of molecular weight and conjugation efficiency. Magn Reson Imaging 10:913–917
117. Tietze LF, Schroter C, Gabius S et al (1991) Conjugation of p-aminophenyl glycosides with squaric acid diester to a carrier protein and the use of neoglycoprotein in the histochemical detection of lectins. Bioconjugate Chem 2:48–53

118. Niemi P, Reisto T, Hemmilä I, Kormano M et al (1991) Magnetic field dependence of longitudinal relaxation rates of solutions of various protein-gadolinium3+ chelate conjugates. Invest Radiol 26:820–824
119. Berthezène Y, Vexler V, Price DC et al (1992) Magnetic resonance imaging detection of an experimental pulmonary perfusion deficit using a macromolecular contrast agent: polylysine-gadolinium-DTPA40. Invest Radiol 27:346–351
120. Sieving PF, Watson AD Rocklage SM (1990) Preparation and characterization of paramagnetic polychelates and their protein conjugates. Bioconjug Chem 1(1):65–71
121. Wu C, Brechbiel W, Kozak RW, Gansow OA (1994) Metal Chelate dendrimer antibody constructs for use radio-immunotherapy and imaging. Bioorg Med Chem Lett 4:449–454
122. Lu ZR, Parker DL, Goodrich KC et al (2004) Extracellular biodegradable macromolecular gadolinium(III) complexes for MRI. Magn Reson Med 51(1):27–34
123. Balkus KJ, Sherry AD, Young SW (1992) Zeolite enclosed transition and rare earth metal ions as contras agents for gastrointestinal tract, US Patent n° 5122363
124. Balkus KJ, Bresinska I (1994) Molecular sieve based MRI contrast agents. J Alloys Coumpd 207(208):25–28
125. Young SW, Qing F, Rubin D et al (1995) Gadolinium zeolite as an oral contrast agent for magnetic resonance imaging. J Magn Reson Imaging 5:499–508
126. Bresinska I, Balkus KJ (1994) Studies of Gd(III)-exchanged Y-type zeolites relevant to magnetic resonance imaging. J Phys Chem 98:12989–12994
127. Platas-Iglesias C, Vander Elst L, Zhou W et al (2002) Zeolite GdNaY nanoparticles with very high relaxivity for application as contrast agents in magnetic resonance imaging. Chemistry 8(22):5121–5131
128. Sun G, Feng J, Wu H et al (2004) Investigation of sandwiched gadolinium (III) complexes with tungstosilicates as potential MRI contrast agents. Magn Reson Imaging 22(3):421–426
129. Aime S, Frullano L, Genibatti Crich S (2002) Compartmentalization of a gadolinium complex in the apoferritin cavity: a route to obtain high relaxivity contrast agents for magnetic resonance imaging. Angew Chem Int Ed 41(6):1017–1019
130. Wilson LJ (1999) Medical applications of fullerenes and metallofullerenes. Electrochem Soc Interface 8:24–28
131. Cagle DW, Kennel SJ, Mirzadeh S et al (1999) In vivo studies of fullerene-based materials using endohedral metallofullerene radiotracers. Proc Natl Acad Sci USA 96:5182–5187
132. Zhang S, Sun D, Li X, Pei F, Liu S (1997) Synthesis and solvent enhanced relaxation property of water-soluble endohedral metallofullerenols. Fullerene Sci Technol 5:1635–1643
133. Mikawa M, Kato H, Okumura M et al (2001) Paramagnetic water-soluble metallofullerenes having the highest relaxivity for MRI contrast agents. Bioconjugate Chem 12:510–514
134. Kato H, Kanazawa Y, Okumura M et al (2003) Lanthanoid endohedral metallofullerenols for MRI contrast agents. J Am Chem Soc 125:4391–4397
135. Bolskar RD, Benedetto AF, Husebo LO et al (2003) First soluble M@C60 derivatives provide enhanced access to metallofullerenes and permit in vivo evaluation of Gd@C60[C(COOH)2]10 as a MRI contrast agent. J Am Chem Soc 125:5471–5478
136. Toth E, Bolskar RD, Borel A et al (2005) Water-soluble gadofullerenes: toward high-relaxivity, pH-responsive MRI contrast agents. J Am Chem Soc 127:799–805
137. Laus S, Sitharaman B, Toth E et al (2005) Destroying gadofullerene aggregates by salt addition in aqueous solution of Gd@C(60)(OH)(x) and Gd@C(60)[C(COOH(2))](10). J Am Chem Soc 127:9368–9369
138. Satishkumar BC, Taubert A, Luzzi DE (2003) Filling single-wall carbon nanotubes with d- and f-metal chloride and metal nanowires. J Nanosci Nanotechnol 3(1–2):159–163
139. Kimura K, Ikeda N, Maruyama Y et al (2003) Evidence for substantial interaction between Gd ion and SWNT in $(Gd@C_{82})_n$@SWNT peapods revealed by STM studies. Chem Phys Lett 379:340–344
140. Sitharaman KR, Kissell KB, Hartman LA et al (2005) Superparamagnetic gadonanotubes are high-performance MRI contrast agents. Chem Comm, pp 3915–3917

141. Langereis S, Hijnen N, Strijkers G et al (2014) Multifunctional liposomes for MRI and image-guided drug delivery. Ther Deliv 5:21–24
142. Langereis S, Geelen T, Grüll H et al (2013) Paramagnetic liposomes for molecular MRI and MRI-guided drug delivery. NMR Biomed 26:728–744
143. Fossheim SL, Fahlvik AK, Klaveness J, Muller RN (1999) Paramagnetic liposomes as MRI contrast agents: influence of liposomal physicochemical properties on the in vitro relaxivity. Magn Reson Imaging 17:83–89
144. Mulder WJM, Strijkers GJ, van Tilborg GAF et al (2006) Lipid-based nanoparticles for contrast-enhanced MRI and molecular imaging. NMR Biomed 19:142–164
145. Hak S, Sanders HMHF, Agrawal P et al (2009) A high relaxivity Gd(III)DOTA-DSPE-based liposomal contrast agent for magnetic resonance imaging. Eur J Pharm Biopharm 72:397–404
146. Geraldes CFGC, Laurent S (2009) Classification and basic properties of contrast agents for magnetic resonance imaging. Contrast Med Mol Imaging 4:1–23
147. Wang Y, Ng YW, Chen Y et al (2008) Formulation of superparamagnetic iron oxides by nanoparticles of biodegradable polymers for magnetic resonance imaging. Adv Funct Mater 18:308–318
148. Ratzinger G, Agrawal P, Körner W et al (2010) Surface modification of PLGA nanospheres with Gd-DTPA and Gd-DOTA for high-relaxivity MRI contrast agents. Biomaterials 31:8716–8723
149. Courant T, Roullin VG, Cadiou C et al (2012) Hydrogels incorporating Gd-DOTA: towards highly efficient dual T_1/T_2 MRI contrast agents. Angew Chem Int Ed 51:9119–9122
150. Callewaert M, Roullin VG, Cadiou C et al (2014) Tuning the composition of biocompatible Gd nanohydrogels to achieve hypersensitive dual T_1/T_2 MRI contrast agents. J Mater Chem B 2:6397–6405
151. Kojima C, Turbey B, Ogawa M et al (2011) Dendrimer-based MRI contrast agents: the effects of PEGylation on relaxivity and pharmacokinetics. Nanomed Nanotechnol 7:1001–1008
152. Wartenberg N, Fries P, Raccurt O et al (2013) A gadolinium complex confined in silica nanoparticles as a highly efficient T1/T2 MRI contrast agent. Chem Eur J 19:6980–6983
153. Zhang J, Ye Y, Chen Y et al (2014) Gd3N@C84(OH)x: a new egg-shaped metallofullerene magnetic resonance imaging contrast agent. J Am Chem Soc 136:2630–2636
154. Ananta JS, Godin B, Sethi R et al (2010) Geometrical confinement of gadolinium-based contrast agents in nanoporous particles enhances T1 contrast. Nat Nanotechnol 5:815–821
155. Platas-Iglesias C, Vander Elst L, Zhou W et al (2002) Zeolite GdNaY nanoparticles with very high relaxivity for application as contrast agents in magnetic resonance imaging. Chem Eur J 8:5121–5131
156. Merbach AE, Helm L, Toth E (eds) (2013) The chemistry of contrast agents in medical magnetic resonance imaging. Wiley, USA, pp 387–421 (Chapter 9)
157. Ward KM, Balaban RS (2000) Determination of pH using water protons and chemical exchange dependent saturation transfer (CEST). Magn Reson Med 44(5):799–802
158. Ward KM, Aletras HA, Balaban RS (2000) A new class of contrast agents for MRI based on proton chemical exchange dependent saturation transfer (CEST). J Magn Reson 143 (1):79–87
159. Aime S, Barge A, Castelli DD et al (2002) Paramagnetic lanthanide(III) complexes as pH-sensitive chemical exchange saturation transfer (CEST) contrast agents for MRI applications. Magn Reson Med 47:639–658
160. Terreno E, Castelli DD, Cravotto G et al (2004) Ln(III)-DOTAMGly complexes: a versatile series to assess the determinants of the efficacy of paramagnetic chemical exchange saturation transfer agents for magnetic resonance imaging applications. Invest Radiol 39 (4):235–243
161. Aime S, Calabi L, Biondi L et al (2005) Iopamidol: exploring the potential use of a well-established x-ray contrast agent for MRI. Magn Reson Med 53(4):830–834

162. Zhang S, Michaudet L, Burgess S, Sherry AD (2002) The amide protons of an ytterbium(III) dota tetraamide complex act as efficient antennae for transfer of magnetization to bulk water. Angew Chem Int Ed Eng 41:1919–1921
163. Zhang S, Merritt M, Woessner DE et al (2003) PARACEST agents: modulating MRI contrast via water proton exchange. Acc Chem Res 36:783–790
164. Zhang S, Winter P, Wu K, Sherry AD (2001) A novel europium(III)-based MRI contrast agent. J Am Chem Soc 123:1517–1518
165. Zhang S, Trokowki R, Sherry AD (2003) A paramagnetic CEST agent for imaging glucose by MRI. J Am Chem Soc 125(50):15288–15289
166. Woessner DE, Zhang S, Merritt ME, Sherry AD (2005) Numerical solution of the Bloch equations provides insights into the optimum design of PARACEST agents for MRI. Magn Reson Med 53(4):790–799
167. Aime S, Castelli DD, Fedeli F, Terreno E (2002) A paramagnetic MRI-CEST agent responsive to lactate concentration. J Am Chem Soc 124:9364–9865
168. Goffeney N, Bulte JW, Duyn J et al (2001) Sensitive NMR detection of cationic-polymer-based gene delivery systems using saturation transfer via proton exchange. J Am Chem Soc 123:8628–8629
169. Snoussi K, Bulté JW, Gueron M, van Zijl PC (2003) Sensitive CEST agents based on nucleic acid imino proton exchange: detection of poly(rU) and of a dendrimer-poly(rU) model for nucleic acid delivery and pharmacology. Magn Reson Med 49:998–1005
170. Aime S, Castelli DD, Terreno E (2003) Supramolecular adducts between poly-L-arginine and [Tm(III)dotp]: a route to sensitivity-enhanced magnetic resonance imaging-chemical exchange saturation transfer agents. Angew Chem Int Ed 42:4527–4529
171. Aime S, Castelli DD, Terreno E (2005) Angew Chem Int Ed, 2487
172. Terreno E, Castelli DD, Aime S (2010) Encoding the frequency dependence in MRI contrast media: the emerging class of CEST agents. Contrast Media Mol Imaging 5(2):78–98

Chapter 5
Superparamagnetic Iron Oxide Nanoparticles

Abstract Thanks to their unique properties, inorganic nanostructures have become the center of modern material science. Among existing nanomaterials, magnetic iron oxide nanoparticles (IONP) have attracted a lot of interest. These nanoparticles are suitable for many technological applications such as contrast agent for magnetic resonance imaging. When comparing to molecular MRI probes (Gd-based organic complexes), IONP present many advantages such as a better sensitivity, a poor toxicity, and the possibility to easily modify their surface to develop some properties as multimodality, modulable half-life or specificity. However, one must stress that these properties are related to IONP's composition, shape and stability (physical and chemical). In that paper, we will introduce some concepts related to IONP's physico-chemical properties, the synthetic ways to obtain such structures and we will finish with some concepts governing their stability and surface modification.

Superparamagnetic iron oxide nanoparticles have a hydrodynamic diameter ranging from 5 to 300 nm (Tables 5.1 and 5.2). These nanomaterials are coated with a natural or synthetic polymer or a small ionic molecule for ensuring a stable suspension [1, 2]. They have a very large magnetic moment and higher transverse relaxivity values than paramagnetic Gd complexes. This magnetic moment creates a local heterogeneity of the magnetic field in the region where water molecules are diffusing. This process leads to an acceleration of proton nuclear spin dephasing and a decrease of transverse relaxation time T_2. With a greater relaxivity r_2 than r_1, these contrast agents have a so-called negative T_2 predominant effect, leading to a decrease of the signal (dark MRI signal). Contrast induced by superparamagnetic agents is optimum using a T_2-weighted (increasing of TR and extending the TE). It is also possible, at low magnetic field to obtain a positive contrast using T_1-weighted sequences.

Two types of superparamagnetic nanoparticles were developed [1, 2] for MRI of liver or lymphatic system:

– Ultrasmall superparamagnetic iron oxide nanoparticle (USPIO, Fig. 5.1) and nanocompound monocrystalline iron oxide (MION) with a hydrodynamic

S. Laurent et al., *MRI Contrast Agents*, Nanotheranostics,
DOI 10.1007/978-981-10-2529-7_5

Table 5.1 Some examples of "ultrasmall superparamagnetic particle of iron oxide" (USPIO) (37 °C, 1.5 T) [2]

USPIO (coating)	Hydrodynamic diameter (nm)	Relaxivity (s^{-1} mM^{-1})
AMI-227, Sinerem®, Combidex® (dextran)	17–30	r_1 = 19.5 r_2 = 87.6
Ferumoxytol (carboxymethyldextran)	30	r_1 = 15 r_2 = 89
SHU-555C, Supravist® (carboxydextran)	30	r_1 = 10.7 r_2 = 38
Feruglose, Clariscan® (pegylated starch)	20	r_1 = 20 r_2 = 35 (0.47 T)
VSOP-C184 (citrate)	7	r_1 = 14 r_2 = 33.4
MION-46L (dextran)	8–20	r_1 = 3.95 r_2 = 19.6

Table 5.2 Some examples of "superparamagnetic particles of iron oxide" (SPIO) (37 °C, 1.5 T) [2]

SPIO (coating)	Hydrodynamic diameter (nm)	Relaxivity (s^{-1} mM^{-1})
AMI-25, Endorem®, Feridex®, Ferumoxides (dextran)	80–150	r_1 = 10.1 r_2 = 158
SHU-555A, Ferucarbodextran, Resovist® (carboxydextran)	60	r_1 = 9.7 r_2 = 189
AMI-121, Ferumoxil, Lumirem®, Gastromark® (silicone)	300	r_1 = 2 r_2 = 47

diameter between 20 and 30 nm, those systems are monocrystalline (single crystal per particle). AMI-227, developed by Advanced Magnetics and Guerbet, is composed of particles with a hydrodynamic diameter of 17 nm and is obtained from a separation column of AMI-25 (Table 5.1).

– Superparamagnetic iron oxide nanoparticles (SPIO, Table 5.2, Fig. 5.1) have a hydrodynamic diameter higher than 60 nm and have several magnetic grains per particle. Among them are the AMI-25, known in Europe under the name Endorem®.

These particles are composed of a polycrystalline iron oxide core entrapped in a crown of dextran. The interactions between the magnetic core and dextran are low. Stabilization can be improved by cross-linked dextran molecules to enhance their interactions with the crystal core (CLIO) [3]. Another class of versatile particles USPIO (VUSPIO) has also been developed [4]. In this case, the dextran molecules are covalently bound via silanol on the surface of nanoparticles.

The majority of iron oxide nanoparticles is often composed of magnetite (Fe_3O_4) and its oxidized form maghemite (γ-Fe_2O_4). These iron oxides exhibit an inverse

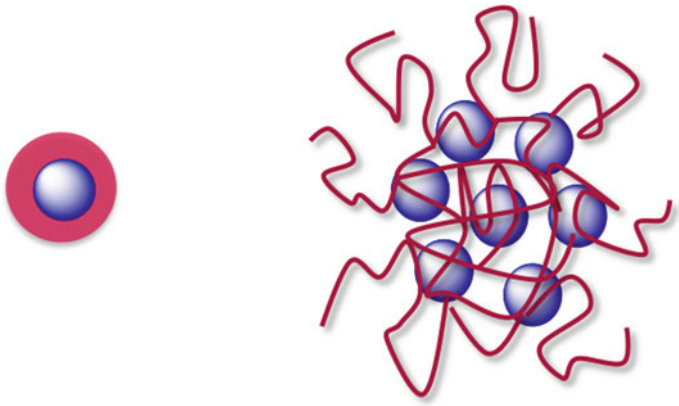

Fig. 5.1 Schematic structures of USPIO and SPIO

spinel structure with a general formula of AB_2X_4 where A and B are cations and X are anions [5]. These crystals adopt a face-centered cubic crystalline structure. Anions delimit the network of the face-centered cubic crystal system and the cations are distributed in tetrahedral and octahedral sites. Specifically, the crystalline structure of magnetite is based on 32 anions of oxygen and contains both divalent and trivalent iron as cations. For one unit cell of magnetite containing 32 oxygens, 64 tetrahedral and 32 octahedral sites are generated. For each unit cell, 8 divalent atoms and 8 trivalent atoms of iron fill the octahedral sites of magnetite (Fig. 5.2) [6]. In the tetrahedral sites, 8 trivalent iron ions are present. Overall, each unit cell of magnetite contains 56 atoms in which there are 32 ions of oxygens, 16 ions of iron (III) and 8 ions of iron (II).

Iron oxide nanoparticles have been the subject of extensive scientific researches during the last decade, and several iron oxide based nanosystems have been

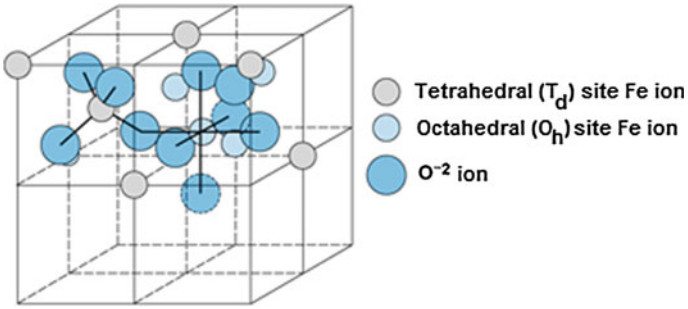

Fig. 5.2 Schematic illustration of inverse spinel of magnetite in which 8 octahedral sites are surrounded by 6 oxygens and 16 tetrahedral sites are surrounded by 4 oxygens. With permission of Ref. [7]. Available from: http://www.intechopen.com/books/modern-surface-engineering-treatments/surface-modification-of-nanoparticles-used-in-biomedical-applications

approved as T_2 agents. They include magnetite (Fe_3O_4), maghemite (γ-Fe_2O_3) and other ferrites which have bivalent metal ions to replace Fe^{2+}, such as $MnFe_2O_4$ [8], $ZnFe_2O_4$ [9] and $CoFe_2O_4$ [10].

5.1 Superparamgnetic Properties of Iron Oxide Nanoparticles

5.1.1 Relaxometric Properties

5.1.1.1 Relaxation Processes of Single Domain Iron Oxide Nanoparticles

Superparamagnetic iron oxide nanoparticles are composed of a single magnetic domain with a size of a few nanometers, the global size being much smaller than a Weiss domain of the corresponding bulk ferromagnetic materials [11, 12].

For these nanoparticles, the directions of the magnetization vector are generally aligned on preferred positions called "easy direction magnetization" or "anisotropy axes" in order to minimize the anisotropy energy of the system. The anisotropy energy can be defined as the energy required to move the magnetization between the positions of easy magnetization axis [13].

The anisotropy energy (E_a) of a single domain is proportional, in a first approximation, to its volume (V) [14]. In the simplest case of uniaxial anisotropy (Fig. 5.3), the energy barrier between two easy magnetization directions is proportional to K_aV and is defined as:

$$E_a = K_a V \sin^2 \theta$$

where K_a is the anisotropy constant and θ is the angle between both anisotropy axis positions.

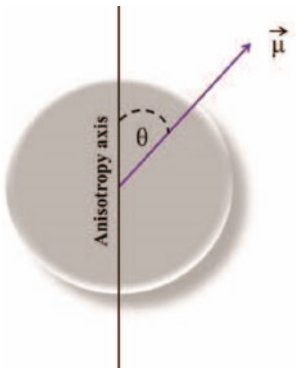

Fig. 5.3 Uniaxial anisotropy axis for superparamagnetic materials

K_a constant can be influenced by four contributions for isolated nanoparticles: (i) the chemical composition and the crystallographic structure of the material, (ii) the nanoparticle shape, (iii) the coating nature and (iv) the inter-distance between the nanoparticles. In the case of agglomerated nanoparticles, only the distance between the nanoparticles contributes to K_a [15].

The anisotropy energy of magnetic crystal dramatically increases with the crystal volume and thus with the particle radius [16]. Consequently, for large crystal, the energy barrier is high and the transitions from an easy axis to another one are not favored. The magnetization vector is thus blocked on an anisotropy axis. On the contrary, for small particles, the transitions of the magnetization from one easy axe to another one are thus easier [17].

The changeover of magnetic moment vector from an easy axis to another is observed when the thermal energy is sufficient to break the anisotropy energy barrier. The average time to switch from one direction to another is called "Néel relaxation time (τ_N)" and is given by

$$\tau_N = \tau_0 E_a e^{\frac{E_a}{Tk_b}}$$

where τ_N is the Néel relaxation time, k_b is the Boltzmann constant, T is the temperature and τ_0 (E_a) corresponds to the preexponential factor of the Néel relaxation time expression.

The alignment of magnetization vector is influenced by two contributions: the anisotropy energy (K_aV) and the thermal agitation energy (k_bT). The ratio between both energies induces two situations as described below:

- If $K_aV \gg k_bT$, the magnetic moment is locked in one of the easy directions. Consequently, the changeover of the magnetic vector to another easy axis involves the complete rotation of the particle.
- If $K_aV \ll k_bT$, the thermal agitation is a dominant factor, the free transition of the magnetization vector on the easy axes occurs without the particle rotation.

For superparamagnetic crystals dispersed in a liquid medium, the return of the magnetic moment to equilibrium state is defined by two different processes: the **Néel relaxation** and the **Brownian relaxation**.

The Néel relaxation is related to the permanent changeover of the magnetization from an easy direction to another one and depends on temperature and crystal volume. The values of the Néel relaxation time τ_N are generally included in the range of 10^{-9}–10^{-11} s. When an external magnetic field is applied, the magnetic moments stay long enough on one easy magnetization axis to produce a resulting magnetization proportional to the strength of magnetic field. The behavior of these particles can be compared to the paramagnetic substances. However, the magnetic susceptibility of superparamagnetic materials is very much higher (100 or 1000 times) due to the collective interactions of electrons, and this explains why these compounds are called superparamagnetic.

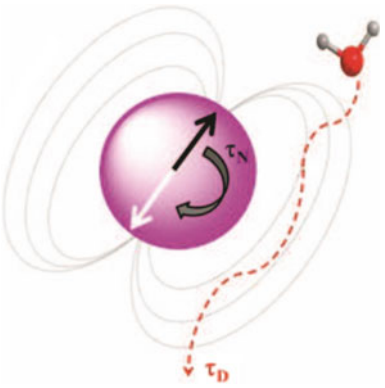

Fig. 5.4 Illustration of water proton relaxation due to the presence of superparamagnetic particles

For large crystals, the Néel relaxation time becomes longer and any changeover of the magnetization is observed because the magnetic moments are locked on an easy axis. The blocking volume (V_B) is defined as a crystal critical volume. This parameter leads to a lock of the magnetization during the measuring time at a given temperature. In this case, only the total rotation of particles submitted to the thermal agitation can be observed. The characteristic time of this rotation is given by the Brownian relaxation times (τ_B):

$$\tau_B = \frac{3V\eta}{k_b T}$$

where V is the crystal volume, η is the fluid viscosity, k_b is the Boltzmann constant and T is the temperature.

In summary, the global magnetic relaxation rate of colloidal suspensions (Fig. 5.4) is modulated by Néel and Brownian relaxation times following this equation:

$$\frac{1}{\tau} = \frac{1}{\tau_N} + \frac{1}{\tau_B}$$

The fastest process dominates the relaxation of system. The Néel relaxation is thus dominant for small crystals, whereas, the relaxation of large crystals is almost exclusively governed by Brownian contribution.

5.1.1.2 Superparamagnetic Relaxation: Theoretical Model

Due to their particular magnetic properties, superparamagnetic particles are used for MRI applications. The high magnetization of these compounds influences greatly the surrounding water relaxation rate.

The understanding of the superparamagnetic relaxation phenomena is possible with the accepted theory established by Roch-Muller-Gillis (commonly called RMG model or SPM model) [13, 18, 19]. This theory is based on the classical outer-sphere relaxation theory, but extended to include the presence of materials with a strong anisotropy. The relaxation induced by superparamagnetic nanoparticles is due to the coupling between the magnetic moments of water protons and the electron magnetic moments of particles. The modulation is caused by Néel relaxation (flip of the magnetization vector of particles from on easy axis to another) and the diffusion of water protons.

RMG model of large crystals will be firstly described and the model of small crystals will be then discussed.

- **For the large crystals (particle radius > 7.5 nm)**

The anisotropy barrier is high, inducing the lock of magnetic moment of superparamagnetic materials on one anisotropy axis when high magnetic fields are applied. Depending on the strength of external magnetic field, several limiting cases can be described as below.

At ***low magnetic fields***, the magnetic moments can easily move from one anisotropy direction to an other causing drastic magnetic fluctuations on the water diffusion in the vicinity of magnetic particles. Consequently, the dipolar interactions between water protons and magnetic core are modulated by the translational correlation time of the water molecules (τ_D) and the Néel relaxation time (τ_N) as shown in Fig. 5.5. Both modulations can be gathered together in a global correlation time (τ_{CI}) as follows:

$$\frac{1}{\tau_{CI}} = \frac{1}{\tau_N} + \frac{1}{\tau_D}$$

where τ_D is equal to the square of crystal radius (r) divided by the diffusion constant (D).

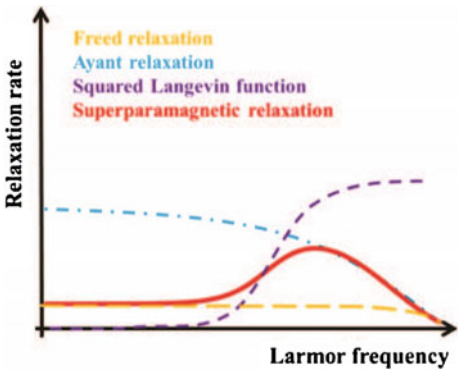

Fig. 5.5 Relaxation model for large magnetic nanoparticles with each contribution

The proton longitudinal and transversal relaxation rates can be expressed from Freed spectral density (J_F) [20]:

$$R_1 = \frac{1}{T_1} = \frac{32\pi}{405{,}000}\gamma^2\mu^2\left(\frac{N_A C}{r^3}\right)[10J_F(\omega_I, \tau_D, \tau_N)]$$

$$R_2 = \frac{1}{T_2} = \frac{32\pi}{405{,}000}\gamma^2\mu^2\left(\frac{N_A C}{r^3}\right)[8J_F(\omega_I, \tau_D, \tau_N) + 2J_F(0, \tau_D, \tau_N)]$$

$$J_F(\omega_I, \tau_D, \tau_N) = R_e\left[\frac{1 + \frac{1}{4}\Omega^{\frac{1}{2}}}{1 + \Omega^{\frac{1}{2}} + \frac{4}{9}\Omega + \frac{1}{9}\Omega^{\frac{3}{2}}}\right]$$

$$\Omega = i\omega_I\tau_D + \frac{\tau_D}{\tau_N}$$

With γ is the proton gyromagnetic ratio, μ is the electron magnetic moment, N_A is the Avogadro number, C corresponds to the molar concentration of superparamagnetic compound, r is the crystal radius and ω_I is the proton angular frequency.

At ***high magnetic fields***, the magnetization vector remains onto one of the easy axes. In this case, the Néel relaxation time is longer due to a high anisotropy. Therefore, the modulation of relaxation solely results from water proton diffusion. This modulation is described thanks to Ayant spectral density (J_A) [21] and the relaxation rates are described as below:

$$R_1 = \frac{1}{T_1} = \frac{32\pi}{405{,}000}\gamma^2\mu^2\left(\frac{N_A C}{r^3}\right)\left[9L^2(\alpha)J_A\left(\sqrt{2\omega_I\tau_D}\right)\right]$$

$$R_2 = \frac{1}{T_2} = \frac{32\pi}{405{,}000}\gamma^2\mu^2\left(\frac{N_A C}{r^3}\right)\left[\frac{9}{2}J_A\left(\sqrt{2\omega_I\tau_D}\right) + 6J_A(0)\right]$$

with

$$J_A(\mu) = \frac{1 + \frac{5\mu}{8} + \frac{\mu^2}{8}}{1 + \mu + \frac{\mu^2}{2} + \frac{\mu^3}{6} + \frac{4\mu^4}{81} + \frac{\mu^5}{81} + \frac{\mu^6}{648}}$$

At ***intermediate magnetic fields***, the water relaxation induced by superparamagnetic particles is modulated by both previous contributions. A linear combination of the equations with Langevin function [L(α)] must be used to take into account that the magnetization is divided in two parts: the first one is locked with external magnetic field and the second one is influenced by Néel relaxation.

$$R_1 = \frac{1}{T_1} = \frac{32\pi}{405{,}000}\gamma^2\mu^2\left(\frac{N_A C}{r^3}\right)\left\{\left(\frac{L(\alpha)}{\alpha}\right)21J_F(\omega_I,\tau_D,\tau_N) + 9\left[1 - L^2(\alpha) - 2\left(\frac{L(\alpha)}{\alpha}\right)\right]J_F(\omega_I,\tau_D,\tau_N) + 9L^2(\alpha)J_A\left(\sqrt{2\omega_I\tau_D}\right)\right\}$$

$$R_2 = \frac{1}{T_2} = \frac{32\pi}{405{,}000}\gamma^2\mu^2\left(\frac{N_A C}{r^3}\right)\left\{\left(\frac{L(\alpha)}{\alpha}\right)19.5J_F(\omega_I,\tau_D,\tau_N) + \left[1 - L^2(\alpha) - 2\left(\frac{L(\alpha)}{\alpha}\right)\right]\frac{9}{2}[J_F(\omega_I,\tau_D,\tau_N) + 6J_F(0,\tau_D,\tau_N] + L^2(\alpha)\left[\frac{9}{2}J_A\left(\sqrt{2\omega_I\tau_D}\right) + 6J_A(0)\right]\right\}$$

In summary, for large crystals, the relaxation is differently modulated depending on the strength of external magnetic field. This theory predicts the evolution of water proton relaxation rate with magnetic field. Each modulation is shown in Fig. 5.5.

The RMG model allows a good fitting of experimental points obtained for large crystals (Fig. 5.6a). However, this model does not fit the particles presenting a lower anisotropy energy (r < 7.5 nm). The experimental data show dispersion at low frequency that does not agree with the theoretical predictions. An example is shown in Fig. 5.6b. Consequently, an adaptation of RMG model has been elaborated.

- **For small crystals (particle radius < 7.5 nm):**

These materials are characterized by a small anisotropy energy in which the magnetic moments can fluctuate from one easy magnetization axis to another one.

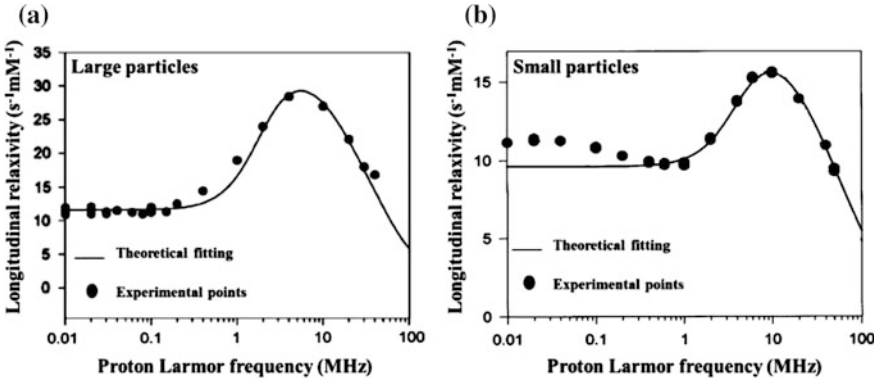

Fig. 5.6 **a** Relaxation evolution of a suspension of large particles (Endorem®: r = 15 nm) as a function of Larmor frequency and **b** relaxation evolution of a suspension of small particles (r = 5 nm) as a function of Larmor frequency. The *line* represents the theoretical fit developed for large magnetic crystals reproduced with permission of Ref. [2]

Therefore, a new theory is required to explain the superparamagnetic relaxation of small magnetic cores. The objective is to insert the anisotropy energy as a quantitative parameter. However, the analysis requires a long calculation time which is not easy to practice. Therefore, Roch et al. [18, 19] developed an alternative heuristic method to include this parameter. This model reproduces the gradual vanishing of the low field dispersion through a linear combination of the rate for infinite and zero anisotropy energy.

$$R_1 = \frac{1}{T_1} = \frac{32\pi}{405{,}000}\gamma^2\mu^2\left(\frac{N_A C}{r^3}\right)\left\{\left(\frac{L(\alpha)}{\alpha}\right)21PJ_F(\omega_I,\tau_D,\tau_N) + 21(1-P)J_F(\omega_I,\tau_D,\tau_N) + 9\left[1 - L^2(\alpha) - 2\left(\frac{L(\alpha)}{\alpha}\right)\right]J_F(\omega_I,\tau_D,\tau_N) + 9L^2(\alpha)J_A\left(\sqrt{2\omega_I\tau_D}\right)\right\}$$

$$R_2 = \frac{1}{T_2} = \frac{32\pi}{405{,}000}\gamma^2\mu^2\left(\frac{N_A C}{r^3}\right)\left\{\left(\frac{L(\alpha)}{\alpha}\right)19.5J_F(\omega_I,\tau_D,\tau_N) + \left[1 - L^2(\alpha) - 2\left(\frac{L(\alpha)}{\alpha}\right)\right]\frac{9}{2}[J_F(\omega_I,\tau_D,\tau_N) + 6J_F(0,\tau_D,\tau_N] + L^2(\alpha)\left[\frac{9}{2}J_A\left(\sqrt{2\omega_I\tau_D}\right) + 6J_A(0)\right]\right\}$$

where P is a weighing factor of the linear combination and ω_s is the electron angular frequency.

The modified model allows a good interpretation of the relaxation for small particles (Fig. 5.7). These predictions have been confirmed with the experimental results for materials with low anisotropy energy [2].

5.1.1.3 Nuclear Magnetic Resonance Dispersion Profiles (NMRD)

NMRD profiles are essential tools to evaluate the relaxometric properties of MRI contrast agents as a function of magnetic field. The measurements are performed

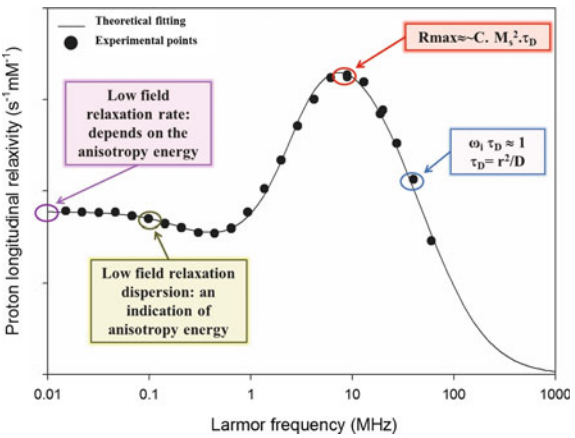

Fig. 5.7 NMRD profiles of superparamagnetic particles. With permission of Ref. [2]

thanks to fast field cycling relaxometer. The method allows a rapid analysis of the properties for new contrast agents and can be exploited to control the reproducibility of the nanoparticle synthetic protocol. The fitting of NMRD profiles with suitable theoretical models provides information about the magnetic crystals (Fig. 5.7) such as their average radius (r), their saturation magnetization (M_s), their anisotropy energy (E_a) and their Néel relaxation times (τ_N).

The dependence of each parameter is explained as follows:

- **Average radius (r):**
  At high magnetic field, the relaxation rate only depends on the diffusion correlation time (τ_D) as shown by the equation of Ayant spectral density. The inflection point corresponds to the condition of $\omega_I.t_D \gg 1$ in which ω_I is the proton Larmor frequency. The diffusion correlation time is defined as a ratio of the square of crystal radius divided by diffusion constant ($\tau_D = r^2/D$) and thus the average radius can be estimated. An increase of crystal size modifies the position of inflection point, which moves towards lower frequency.
- **Saturation magnetization (M_s):**
  At high magnetic fields, the saturation magnetization is reached and can be estimated from the relaxivity maximum by M_s $(R^{max}/c\tau_D)^{1/2}$, where c and R^{max} respectively correspond to a constant and the maximum relaxation rate.
- **Crystal anisotropy energy (E_a):**
  The dispersion observed at low magnetic fields informs on the presence of crystals with low anisotropy energy. For materials with high anisotropy energy, no pitch dispersion is observed. The dispersion at low frequencies gives qualitative information on the magnitude of anisotropy energy of magnetic compounds in solution.
- **Néel relaxation time (τ_N):**
  The Néel relaxation time obtained from the theoretical fitting is an approximate value. It can be used as qualitative information in addition to the crystal size and the specific magnetization by theoretical model.

The magnetic and relaxometric measurements give a complete description of the physico-chemical properties of iron oxide nanoparticles. It is important to notice that the RMG model is based on the assumption that nanoparticle size is uniform, and consequently, the theoretical parameters extracted from the theoretical fitting are average values. However, in the real situations, the size distribution of magnetic crystals is often inhomogenous. If the size distribution is large, the nanoparticle suspensions contain crystals with different sizes or agglomerated nanoparticles, and consequently, the obtained theoretical parameters don't represent the effective characteristics of nanoparticle suspension.

5.2 Synthesis of Magnetic Nanoparticles

The preparation of magnetic materials in bulk form is easy. However, reducing the crystal size to the nanometer scale, brings some new complexities to synthesize these functional materials.

Due to their great potential in a wide range of domains, numerous synthetic methods were developed to produce iron oxide nanoparticles [22–28].

The synthetic way is very important and has a high impact on the characteristic of the SPIONs: size, size distribution, shape, surface chemistry, … Preparation routes can be classified into three main categories [29]: physical (aerosol, gas phase deposition, pulsed laser ablation, electron beam lithography, laser induced pyrolysis), biological (production from fungi, bacteria or proteins) and chemical (coprecipitation, thermal decomposition, microemulsion, sonochemical, electrochemical deposition) methods. Chemical methods represent most of the published protocols because they are easy, cheap and allow the best control on size, shape and composition.

The synthesis of magnetic nanoparticles in a solution by a chemical reaction consists in the formation of nuclei, followed by particles growth. When the formed monomers achieve saturation and then the supersaturation state, the nucleation is initiated such that monomers gather to form nuclei, followed by subsequent growth to result in the formation of nanoparticles. The relationship between supersaturation and nucleation and growth is defined by the following simplified equations,

$$B = k_b \Delta C^b$$
$$G = k_g \Delta C^g$$

where B and G are the nucleation and growth rates, respectively; the subscripts b and g refer to nucleation order and growth order, respectively; k is a constant and ΔC is the supersaturation [30]. It is well acknowledged that a drastic burst of nucleation followed by slow controllable growth is critical to obtain monodisperse nanoparticles.

Synthesis of nanoparticles with uniform size and morphology is possible under conditions of rigorous control on kinetics of the nucleation and growth. The optimal control can be achieved when the two processes are separated in time, where nucleation needs to be completed before the beginning of growth of nuclei.

5.2.1 Coprecipitation Method

Coprecipitation technique is the most simple and efficient way to prepare iron oxide nanoparticles. In this method, nanoparticles are produced by heating 2/1 stoichiometric mixture of ferric and ferrous salts in alkaline medium [31, 32]. The size, shape, and composition of the particles depend on several parameters as the salts,

the pH of the solution, the temperature and the ionic strength of the media [33–35]. Chemical reaction of magnetite (Fe_3O_4) formation can be written as:

$$Fe^{2+} + 2Fe^{3+} + 8OH^- \rightarrow Fe_3O_4 + 4H_2O$$

A complete precipitation of Fe_3O_4 occurs at a pH between 9 and 14, and under a non-oxidizing oxygen-free environment. Fe_3O_4 is not very stable and is rapidly oxidized into γ-Fe_2O_3 in the presence of oxygen. Nitrogen is used to produce non oxidative environment but also to reduce the particle size [36, 37].

There are three phases in the coprecipitation process. In phase I, monomer concentration increases up to its saturation point. Then (phase II), small nuclei are formed when the concentration of the species reaches critical supersaturation. This second phase is followed by the growth of the crystal (phase III). The nucleation and growth steps need to be separated for producing nanoparticles [38, 39]. This phenomenum can be illustrated in the LaMer diagram (Fig. 5.8).

The presence of chelating organic molecules with negative charges (carboxylate ions, such as gluconic, citric, oleic acid, …) or polymers (natural or synthetic as dextran, polyvinyl alcohol, starch, polyethyleneglycol, …) during the formation of nanoparticles can help to control their size. Addition of organic ions can inhibit nucleation or crystal growth and lead to larger or smaller particles.

The most common synthesis is the Massart's method [41]. $FeCl_3$ and $FeCl_2$ are mixed in alkali to produce the nanoparticles. In the original synthesis of Massart, the magnetite particles have a mean diameter of 8 nm [42]. The influence of the base (NaOH, NH_4OH or CH_3NH_2), the pH, the cations (Na^+, Li^+, K^+, NH_4^+, $N(CH_3)_4^+$, and $CH_3NH_3^+$), and Fe^{3+}/Fe^{2+} ratio were studied. Depending on these different parameters, particles with size between 4.2 and 16.6 nm can be obtained. The influence of pH and ionic strength were also studied, and particle size between 2 and 15 nm were produced. The shape of the particles is correlated with the electronic surface density of the nanoparticles [43, 44].

The synthetic medium can be aqueous media or organic solvents [45]. Massart [42] reported also the synthesis of γ-Fe_2O_3 by a rapid method which allows various coatings, such as α-hydroxyacids, aminoacids, hydroxamates, or dimercaptosuccinic acid.

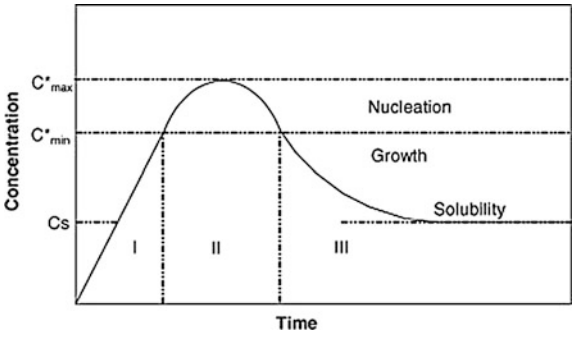

Fig. 5.8 LaMer diagram illustrating the nucleation and growth during the coprecipitation synthesis. The nucleation process rapidly occurs with a subsequent nuclei formation. With the permission of reference [40]. Available from https://www.researchgate.net/figure/215475567_fig13_LaMer-diagram

The influence of Fe^{2+}/Fe^{3+} ratio on the size, shape, composition, and magnetic properties of the nanoparticles has been studied [46]. When the ratio is too small, FeO(OH) are formed in the solution. When the ratio is equal to 0.3, two phases are present. The first one has a Fe^{2+} and Fe^{3+} ratio of 0.07 and produces 4 nm particles; the other one has a ratio of 0.33 and gives larger particles. When this ratio is 0.35, only one phase exists. When this ratio is 0.5, the particles are homogeneous in size and in chemical composition.

The pH and ionic strength has a strong influence on the particle size. Due to their effect on the electrostatic surface charge, the particle size and size distribution width decreases when the pH and the ionic strength are increased [47].

The mixing rate can also influence the particle size: if the mixing rate increases, the size of the particles decreases. The influence of temperature has also been studied: the number of magnetite nanoparticles decreases when the temperature increases [33].

In aqueous synthesis, coprecipitation is widely employed to obtain different ferrites (MFe_2O_4, M = Fe, Mn, Co, Mg, Zn, Ni, etc.). Coprecipitation of thermodynamically favourable phases is propitious to obtain well-crystallized anhydrous oxides, even from diluted solutions.

The general reaction formula is:

$$2Fe^{3+} + M^{2+} + 8OH^{-} \rightarrow MFe_2O_4 + 4H_2O$$

Fe_3O_4, for example, has been synthesized by a simple coprecipitation of Fe^{3+} and Fe^{2+} in 2:1 molar ratio with NaOH above 70 °C [48]. Fe_3O_4 nanoparticles can also be obtained by coprecipitation using tetramethylammonium hydroxide with or without aqueous ammonia as the OH^{-} source [49]. $ZnFe_2O_4$ nanoparticles of 3–4 nm were similarly prepared from Zn^{2+} and Fe^{3+} solutions at temperatures ranging from 40 to 100 °C [50]. The relaxivities have been shown to be dependent on the size of magnetic particles, which can be controlled during the synthesis process by changing the conditions of coprecipitation. $CuFe_2O_4$ nanoparticles were obtained by coprecipitation in alkaline medium of a ferrite stoichiometric mixture of Cu^{2+} and Fe^{3+} [51]. By controlling the pH and ionic strength, variations of size and shape can be observed, without complexing agents [52]. The nanoparticles obtained from coprecipitation did not have to be annealed at a high temperature, which can avoid their agglomeration in some degree. It is especially helpful for the medical applications, where the agglomeration of particles should be avoided.

5.2.2 Hydothermal Method

In the hydrothermal way, reactions are performed in the aqueous media in rectors or autoclaves at high pressure (higher than 2000 psi) and high temperature (above 200 °C) [53, 54].

Two main routes are used for the formation of ferrites: hydrolysis and oxidation or neutralization of mixed metal hydroxides. These two reactions are similar, except that ferrous salts are used in the first method [55]. The solvent, the temperature and the reaction time have a large effect on the particle characteristics [56]. The size of the particles increases when the reaction time or when the amount of water increase. At higher temperatures, the nucleation process is faster than the crystal growth and the size of the particles decreases. With longer reaction time, the crystal growth dominates and larger particles can be formed. Magnetite nanoparticles with a size up to 27 nm have been obtaiend by hydrothermal method [57].

5.2.3 Thermal Decomposition Method

Thermal decomposition of iron precursors in the presence of hot organic surfactants is probably the best method to control the size, the size distribution, and to obtain a good crystallinity of the synthesized nanoparticles [58].

Numerous types of thermal decomposition of iron complexes ($Fe(Cup)_3$, $Fe(CO)_5$, or Fe $(oleate)_3$) have been developed. For exemple, Sun et al. described a high temperature mediated reaction of iron acetylacetonate ($Fe(acac)_3$) with 1,2-hexadecanediol in the presence of oleic acid and oleylamine. Resulting nanoparticles were monodisperse and size could be tuned from 4 nm to 20 nm [59].

The decomposition of iron pentacarbonyl in the presence of oleic acid at 300 °C allows the production of magnetite nanoparticles with a very good crystallinity, the size of the particles obtained range from 4 to 16 nm [58]. The size and shape of the particles are determined by the reaction time, temperature, precursors, concentration, ratios of the reactants, and solvent. The oleic acid on the surfaces of the particles is used to stabilize the colloid solution.

The thermal decomposition of iron carbonyl in the presence of octyl ether and oleic acid and using consecutive aeration can produce hydrophobic magnetite nanoparticles with narrow size distribution [60].

The thermal decomposition of iron oleate or iron pentacarbonyl in organic solvent at different temperatures can produce particles with size between 4 and 11 nm [61].

This method produced nanoparticles dispersible in organic solvents but not in aqueous medium. The decomposition of $Fe(acac)_3$ or $FeCl_3$ in refluxing 2-pyrrolidone can produce water-dispersible particles in acidic or basic media [62, 63]. The decomposition of $Fe(acac)_3$ in high boiling organic solvent allowed to obtain particles with size of 4, 6, 9 or 12 nm and very narrow size distribution. They are coated by 2,3-dimercaptosuccinic acid and are dispersible in water [64].

The decomposition of $Fe_3(CO)_{12}$ in the presence of oleic acid and diethylene glycol diethyl ether has also been described [65]. The particles are then annealed at 300, 700, and 900 °C. The annealing temperature helps to control the size, size distribution, composition, and magnetic properties of the particles.

To control the oxides crystal growth and to get uniform size and shape of nanoparticles, the decomposition is performed in low polar solvents and high boiling point. The solvents in thermolysis sometimes can be used as the stabilizing agent, for their high dielectric constant or high donor number [66, 67]. $Fe(acac)_3$ is mostly used as the Fe-source for forming Fe_3O_4 by thermolysis. To achieve the control over the nucleation and growth processes, assistant agents interacting with metal atoms and solvents are required, which mostly employ polymers with nucleophilic groups, capping ligands and organoaluminium agents. Superparamagnetic Fe_3O_4 nanoparticles with different sizes were synthesized from high-temperature reaction of iron acetylacetonate and 1,2-hexadecanediol in high-boiling phenyl ether solvent in the presence of oleic acid and oleylamine [59]. $CoFe_2O_4$ and $MnFe_2O_4$ nanoparticles were synthesized by the same method but with addition of $Co(acac)_2$ and $Mn(acac)_2$, respectively. It was found that particle diameter can be tuned from 3 to 20 nm by varying reaction conditions such as refluxing temperature or by seed-mediated growth. The key to obtain monodisperse nanoparticles was the pretreatment of mixture solution at 200 °C for some time before refluxing. Gao and his coworkers reported the synthesis of Fe_3O_4 nanoparticles via the thermal decomposition of $Fe(acac)_3$ dissolved in 2-pyrrolidone, which was used as the polar solvent and also the ligand agents for controlling the crystal growth and preventing the agglomeration [68]. For the application as MRI CAs, Fe_3O_4 nanoparticles obtained by thermolysis were transferred from hydrophobic to hydrophilic, using hydrophilic polymers like monocarboxyl-terminated poly(ethylene glycol) (MPEG-COOH) [69, 70] and by amphiphilic molecular like oleyl alcohol [71].

Size of the nanoparticles synthesized using by thermal decomposition method depends strongly of the reaction temperature, the iron to surfactant ratio and the reaction time. Nanoparticles obtained are soluble in organic solvents, they are stabilized and protected from aggregation by a surfactant surface coating as lauric or oleic acid: the polar head group of the surfactant is oriented on the nanoparticle surface and the hydrophobic tail is extended away from the nanoparticles as shown in Fig. 5.9 [72, 73].

5.2.4 Sol-Gel Methods

The sol-gel process is based on the hydrolysis and condensation of precursors in a colloidal solution (sol). A metal oxide network (gel) can be obtained by removing solvent or chemical reaction: a colloidal gel is produced by basic catalysis and a polymeric form of the gel is produced by acidic catalysis [74].

The rates of hydrolysis and condensation influence the properties of particles formed. A lower and more controlled hydrolysis rate allows to produce smaller particles. The size of the particles can also be correlated to the solvent, concentration, pH, and temperature [75].

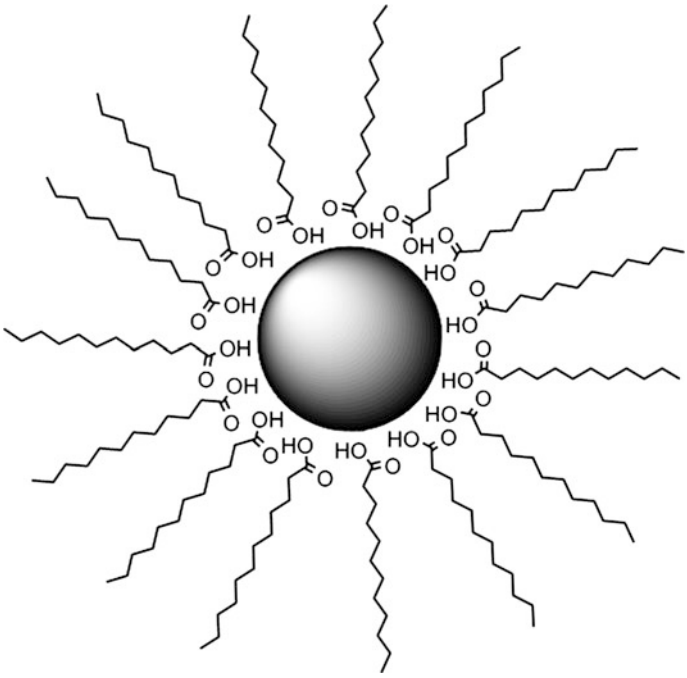

Fig. 5.9 Representation of SPIONs synthesized by thermal decomposition method. SPION surface is coated with lauric acid during the synthesis

After a treatment at 400 °C, Fe_2O_3 particles with a size between 6 and 15 nm are formed [76]. With this method, Fe_2O_3 nanoparticles can be coated in an inert and inorganic silica matrix [77, 78].

5.2.5 Microemulsions

A microemulsion is a thermodynamically stable dispersion of two immiscible liquids. In water-in-oil microemulsion systems, the microdroplets of the aqueous phase surrounded by surfactant molecules are dispersed in a continuous oil phase [38]. The role of surfactant molecules is the limitation of the nucleation, the growth, and thus the agglomeration of the particles [79, 80]. The growth of the particles is due to an interdroplet exchange and nuclei aggregation [81, 82].

Water-in-oil (w/o) microemulsions are formed by well-defined nanodroplets of the aqueous phase, dispersed by the assembly of surfactant molecules in a continuous oil phase. Vidal-Vidal et al. [83] have reported the synthesis of

monodisperse maghemite nanoparticles by the one-pot microemulsion method. Due to the nanometer size of the aqueous core, the particles formed usually have a size less than 15 nm and a very narrow size distribution. The biggest advantage of this method is the control of the particle size.

5.2.6 Polyol Methods

The polyols, like polyethyleneglycol, have some good properties: (i) a high dielectric constant, (ii) an ability to dissolve inorganic compounds, and (iii) a high boiling temperature. They offer a wide range of operating temperature for the production of inorganic compounds [84]. Nanoparticles can be produced by the reduction of dissolved iron salts and precipitation in the presence of polyol [85, 86].

The polyols are used as reduction agents and also as stabilizers, they can control the growth of particles and prevent aggregation. In this method, the precursor is suspended in the liquid polyol. The suspension is stirred and heated to reach the boiling point of polyol. The precursor becomes soluble in the diol during the process. The size and shape of the nanoparticles can be regulated by controlling the kinetic of the process.

The yield of iron oxide nanoparticles depends on the kind of polyols and ferrous salts, but also on the concentration and temperature. The size and yield of the particles are related to the reduction potential of the polyols [87].

Non-aggregated magnetite nanoparticles have been produced by a modified polyol method [88]. Different polyols, including ethylene glycol, diethyleneglycol, triethylene glycol, and tetraethylene glycol, have been used to react with $Fe(acac)_3$ at high temperature. The non-aggregated magnetite nanoparticles with narrow size distribution and uniformed shape are only produced when using triethylene glycol.

5.2.7 Electrochemical Methods

Nanoparticles with a size between 3 and 8 nm have been synthesized by electrochemical method [89]. In this method, the particles are prepared from an iron electrode in an aqueous solution of dimethylformamide and cationic surfactant; the nanoparticle size is controlled by the current density.

5.2.8 Aerosol/Vapor Method

Aerosol methods, including spray and laser pyrolysis, are continuous chemical processes allowing high rate production.

Spray pyrolysis consists in a process where a solution of ferric salts and a reducing agent in organic solvents is sprayed into a series of reactors, then the solvent is evaporated and the solute condenses. The size of the original droplets controls the particle diameter. Using different iron precursors in alcoholic solution, maghemite particles with size ranging from 5 to 60 nm and with different shapes can be produced.

Laser pyrolysis is a method to reduce the reaction volume. In this method, laser is used to heat a flowing gaseous mixture of iron precursor, and non-aggregated particles with small size and narrow size distribution can be obtained. By controlling the experimental conditions, maghemite particles can have a size between 2 and 7 nm and a very narrow size distribution [90, 91]. For example, maghemite nanoparticles with a size of 5 nm have been synthesized by continuous laser pyrolysis of $Fe(CO)_5$ vapors [92].

5.2.9 Sonolysis/Thermolysis

The decomposition of organometallic precursors by sonolysis can also produce iron oxide nanoparticles. Polymers, organic capping agents, or structural hosts allow to limit the particle growth [93, 94]. The rapid collapse of cavities generated by sonochemistry gives very high temperature hot spots. These spots allow the conversion of ferrous salts into magnetic nanoparticles. For example, magnetite nanoparticles have been produced by the sonolysis of $Fe(CO)_5$ aqueous solution in the presence of sodium dodecyl sulfate [95].

In another example, well-defined supermagnetic iron oxide nanoparticles have been produced by sonolysis [96]. Stable particles coated with oleic acid can be dispersed in chitosan solution and have a size of 65 nm.

For biomedical applications, the control of particle size, size distribution, particle shape, and magnetic properties is very important. Different physico-chemical characteristics can be obtained by different fabrication methods (Table 5.3).

According to the comparison of the different synthetic way to form iron oxide nanoparticles, thermal decomposition of metal iron precursors appears as the most profitable and the most promising synthetic method to produce monodispersed crystalline magnetic nanomaterials. This process forms well-controlled iron oxide particles without the use of a size selection step at the end of the synthesis.

5.3 Stabilization of Nanoparticle Suspensions

Colloidal suspensions are stable dispersions of small solid particles ranging in size from 1 nm to 1 µm. Stable nanoparticle dispersions are colloidal suspensions. The behavior of such solutions is dictated by the rules of interface and colloid science [97].

Table 5.3 Summary of the synthetic method of iron oxide nanoparticles

Synthetic methods	Synthesis comments	Reaction temperature (°C)	Reaction period	Solvent	Size distribution	Shape control
Co-precipitation	Very simple, ambient conditions	20–90	Minutes	Water	Relatively narrow	Poor
Thermal decomposition	Complicated, inert atmosphere	100–320	Minutes hours	Organic compound	Very narrow	Very good
Microemulsion	Complicated, ambient conditions	20–50	Hours	Waterorganic compound	Relatively narrow	Good
Hydrothermal synthesis	Simple, high pressure	130–250	Hours–days	Water or/and organic compound	Very narrow	Very good
Polyol	Simple, high temperature and inert conditions	120–280	Minutes days	Polyol compound	Relatively broad	Good
Sol-gel	Complicated, high temperature	200–400	Minutes days	Water or/and organic ompound	Relatively broad	Good

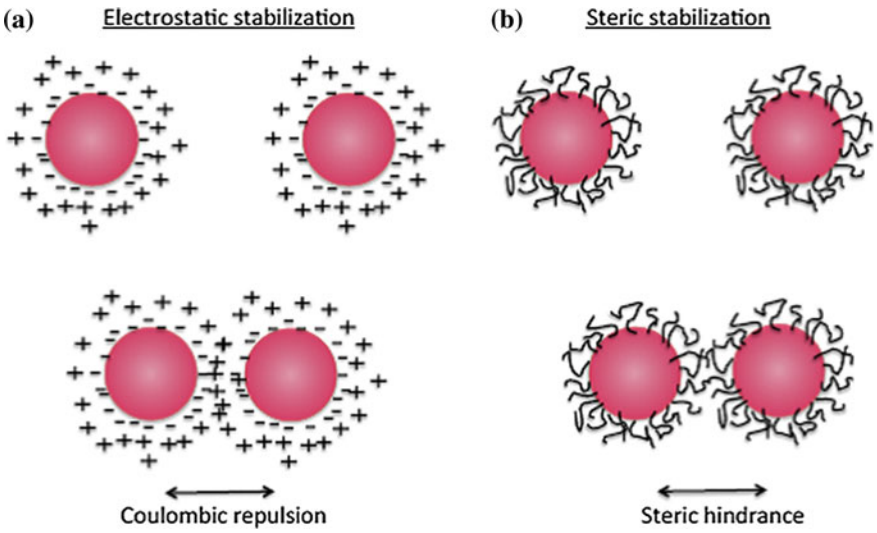

Fig. 5.10 Representation of the two possible ways for particle stabilization. **a** Electrostatic stabilization, **b** steric stabilization

Due to their high surface-to-volume ratio, nanoparticles tend to aggregate in order to lower their interfacial energy. The destabilization is caused by interparticle attractions. The dispersion state of nanoparticle solutions is an important factor while synthesizing nanoparticles for biomedical applications because it tends to modify their physico-chemical properties. The DLVO theory (named after Dejaguin, Landau, Verwey and Overbeek) [98–104] describes the stability of colloid suspensions and will be presented later.

Production of stable nanoparticle suspensions is challenging and primordial for biomedical applications. Stability of nanoparticles in a colloidal system is related to their tendency to aggregate under the action of gravity. Destabilization results from attractive van der Waals interactions.

One way to stabilize nanoparticles is to introduce interparticle repulsions that avoid van der Waals attraction. This can be achieved (A) by charging particles so that the surface charge leads to interparticle repulsion forces or (B) by covering the nanoparticles with big molecules to create interparticle steric repulsions.

The first strategy is known as electrostatic stabilization and the second is the steric stabilization (Fig. 5.10).

5.3.1 Stability of Charged Nanoparticles

This section highlights the factors that control stability. Nanoparticles can acquire a charge by four different mechanisms [97]:

– ionization of surface groups where the degree and nature of which are controlled by the pH of the solution,
– ion adsorption as for instance the adsorption of a cationic surfactant,
– isomorphous substitution,
– dissolution in ionic solids.

To understand the stabilization mechanism, it is primordial to study what happens when a charged particle is in solution. Let's take the case of a positively charged nanoparticle. When placed in a solution containing inert ions, anions will be attracted by the nanoparticle surface and cations repelled from the interface. Electroneutrality is reached when the magnitude of the negative charge of the layer near the interface is equal to the magnitude of the nanoparticle's surface charge.

This charged surrounding is known as the electrochemical double layer. It is characterized by a potential drop across the solid/liquid interface which is described by the Stern-Gouy-Chapman (SGC) model. According to this latter, the surface charge is counterbalanced by two distinctive regions, the Helmholtz layer (or inner layer) and the Gouy-Chapman layer (or diffuse layer) (Fig. 5.11). They both contribute to the total interfacial charge density.

The innerlayer includes the inner Helmholtz plane (IHP) and the outer Helmholtz plane (OHP). Ions directly adsorbed to the surface are located in the IHP and OHP is defined as the plane of closest approach of fully solvated ions. The charge in OHP is counterbalanced by a dynamic ionic atmosphere forming the diffuse layer.

The surface potential at the diffuse layer is called zeta potential (ε) and is an experimentally measurable value.

The SGC model considers that the solvent is a dielectric continuum and that ionic species are non-interacting point charges. It assumed that the total interfacial charge density depends on ionic species concentration in solution and on the permittivity of the solvent.

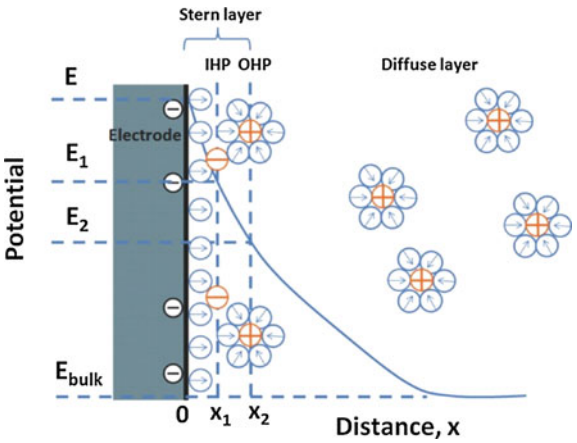

Fig. 5.11 Representation of the electrochemical double layer in accordance with the SGC model. Reproduced from Ref. [105]

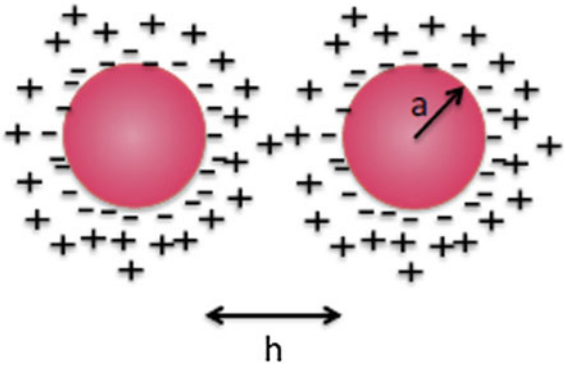

Fig. 5.12 Representation of two colloidal particles coming close together

Stability of a whole colloidal system can be predicted by studying what happens when two nanoparticles come close together because of the Brownian motion. The colloidal pair potential governs the stability of colloidal dispersions, it is defined as the potential energy of interaction between two colloidal particles. The most relevant components for interaction between charged particles are the van der Waals and the repulsive forces (Fig. 5.12).

The potential energy resulting from attractive forces (U_A) is proportional to the particle radius (a), a material constant named the Hamaker constant (A) and the inverse of the distance of separation (h) [106]. It is given by equation.

$$U_A = -\frac{A}{12}\left[\frac{1}{x(x+2)} + \frac{1}{(x+1)^2} + 2\ln\frac{x(x+2)}{(x+1)^2}\right]$$

where $\chi = h/2a$

If the particles are very close ($h \ll 2a$), then the last equation can be simplified and the potential energy becomes,

$$U_A = -\frac{Aa}{12h}$$

The Hamaker constant depends on the electronic polarisability and the density of the material. Table 5.4 provides the value of the Hamaker constant for some media and materials.

$$A = \left(\sqrt{A_{particle}} - \sqrt{A_{medium}}\right)^2$$

The electrostatic repulsion is an important stabilization mechanism of charged nanoparticles dispersed in aqueous solutions. When two of them come close together, two cases exist: their surface charge doesn't change and the surface potential compensates or the opposite.

Table 5.4 Value of the Hamaker constant of some components [99]

Media	Hamaker constant ($J/10^{-20}$)
Water	3.7
Ethanol	4.2
Cyclohexane	5.2
Particles	**Hamaker constant ($J/10^{-20}$)**
Silica	6.5
Titanium dioxide	19.5
Metals (Au, Ag, …)	40

Hogg, Healy and Fuersteneau have developed equations describing the electrostatic interaction between two non-identical particles under constant charge $\left(U_R^{\sigma}\right)$ and constant potential $\left(U_R^{\psi}\right)$ [107]

$$U_R^{\psi} = \frac{\varepsilon a_1 a_2 \left(\psi_{01}^2 + \psi_{02}^2\right)}{4(a_1 + a_2)} \left[\frac{2\psi_{01}\psi_{02}}{\psi_{01}^2 + \psi_{02}^2} \ln\left(\frac{1 + e^{-\kappa h}}{1 - e^{-\kappa h}}\right) + \ln\left(1 + e^{-2\kappa h}\right) \right]$$

$$U_R^{\sigma} = \frac{\varepsilon a_1 a_2 \left(\psi_{01}^2 + \psi_{02}^2\right)}{4(a_1 + a_2)} \left[\frac{2\psi_{01}\psi_{02}}{\psi_{01}^2 + \psi_{02}^2} \ln\left(\frac{1 + e^{-\kappa h}}{1 - e^{-\kappa h}}\right) + \ln\left(1 - e^{-2\kappa h}\right) \right]$$

where κ^{-1} is the Debye length defined as the thickness of the electrical double layer, ε is the dielectric constant of the suspending medium, ψ_{01}, ψ_{02} are the total double layer potentials of the respective particles, h is the distance between the particles and a_1 and a_2 are the particle radii.

For two identical particles, $a_1 = a_2 = a$, $\psi_{01=}\ \psi_{02}\ = \psi_0$ and these two last equations become,

$$U_R^{\psi} = \frac{\varepsilon a \psi_0^2}{2} \ln\left(1 + e^{-\kappa h}\right)$$

$$U_R^{\sigma} = \frac{\varepsilon a \psi_0^2}{2} \ln\left(1 - e^{-\kappa h}\right)$$

and if $\kappa a < 3$, then the general expression is given by equation

$$U_R = 2\pi\varepsilon\alpha\psi_0^2 e^{-\kappa h}$$

According to the DLVO theory, the colloidal stability of charged particles relies on the total potential resulting from the interaction of colloidal particles (Fig. 5.13). It is equal to the linear sum of the attractive and the repulsive potentials. The attractive potential results from attractive van der Waals forces and the repulsive one from repulsive electrical double layer forces. The result is a typical curve for charge-stabilized colloid particles.

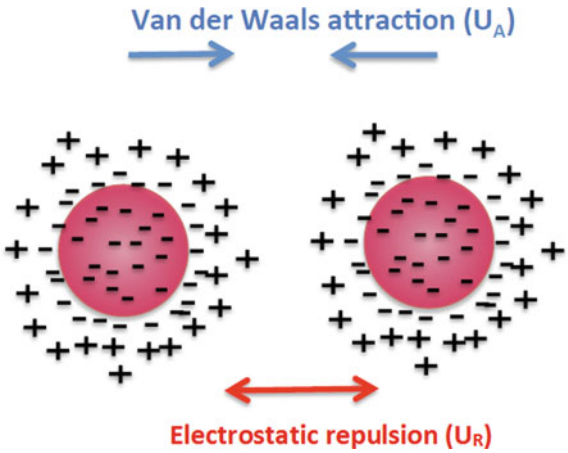

Fig. 5.13 Representation of the DLVO theory showing the interparticle interaction as the result of the van der Waals attraction and the electrostatic repulsion

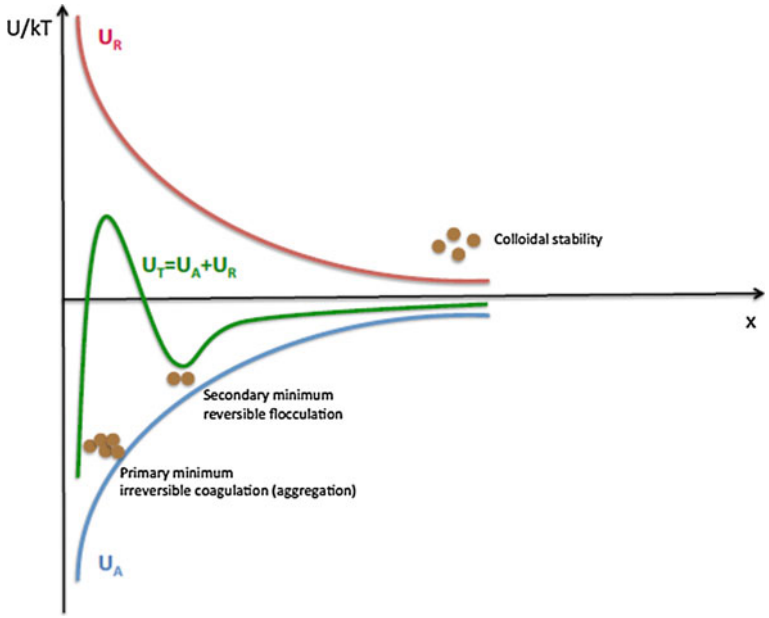

Fig. 5.14 Shape of the total potential energy (U_T) as a function of the distance (x)

$$U_T = U_A + U_R$$

From low to high interparticle distance, the shape of the curve presents, first, a primary minimum leading to irreversible coagulation (aggregation), then, a potential energy barrier and finally, a secondary minimum resulting in reversible flocculation (Fig. 5.14).

Nevertheless, while the DLVO theory works reasonably well to predict the stability of colloidal solutions at law salt concentrations ($< 5 \times 10^{-2}$ M), it has been shown to fail at higher ionic salt concentrations. The magnitude of forces varies greatly by changing counter-ion and is not in good agreement with the experiment anymore. This is explained by the fact that the theory ignores ion effects and dispersion forces acting on the ions.

At low salt concentration, electrostatic forces dominate so that the DLVO theory that describes interparticle interaction as the result of attractive VDW forces and repulsive electrical double layer forces is sufficient. But at higher salt concentration, buffer specificity is influent, dispersion forces are expected to dominate electrostatic forces and must be treated at the same level [108]. This is a major problem particularly when samples are devoted to biomedical applications because biological salt concentrations are more or less equal to 0.1 M. It can be solved by properly including dispersion forces acting on ions.

5.3.2 Steric Stabilization

The colloidal stability resulting from steric stabilization, for example the adsorption of polymer chains on the particle surface, is based on steric hindrance. The total potential function is the linear sum of the attractive potential (U_A) due to van der Waals interaction and a steric potential (U_s) and is given by the following equation.

$$U_S = 4\pi akT(0.5 - \chi)\Gamma^2 e^{\left(1-\frac{h}{2\sigma}\right)}$$

where h is the interparticle distance, Γ is the amount of adsorbed or grafted polymer, σ is the layer thickness and χ is the Flory polymer/solvent interaction. In the ideal case of stability, $\chi < 0.5$ and U_S is repulsive; if $\chi > 0.5$, U_S is attractive and the solution is not stable.

$$U_T = U_A + U_S$$

5.3.3 The Surface of Iron Oxide Nanoparticles

In order to describe the different stabilization methods, it is essential to define the surface nature of iron oxide nanoparticles. During the nanoparticle formation, surface is covered by epoxy functions which naturally react with water molecules to form hydroxyl groups on surface (Fig. 5.15).

The hydroxyl groups on nanoparticle surface exhibit amphoteric properties and thus their charge can be modified with pH variation. These charge modification can

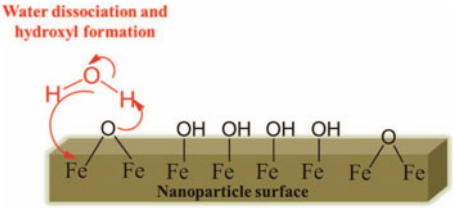

Fig. 5.15 Schematic representation of hydroxyl formation on iron oxide surface

modulate the surface with positive or negative charges as illustrated by following relations:

As a function of pH, acido-basic equilibriums are:

$$\mathbf{Fe{-}OH_2^+} \leftrightarrow \mathbf{Fe{-}OH} + \mathbf{H^+} \quad \text{with } k_a^+ = \frac{[\text{Fe–OH}]\left[\text{H}^+\right]}{\left[\text{Fe–OH}_2^+\right]}$$

$$\mathbf{Fe{-}OH} \leftrightarrow \mathbf{Fe{-}O^-} + \mathbf{H^+} \quad \text{with } k_a^- = \frac{[\text{Fe–O}^-]\left[\text{H}^+\right]}{[\text{Fe–OH}]}$$

The superficial electrical charge (q_0) is given by:

$$q_0 = \left(\frac{F}{S}\right)\left\{\left[\text{Fe}{-}\text{OH}_2^+\right] - \left[\text{Fe}{-}\text{O}^-\right]\right\}$$

where S is nanoparticle area by volume unit ($m^2\ L^{-1}$), F is Faraday constant (96,500 C mol^{-1}) and the second factor correspond to the difference between the concentrations of both charged species (mol L^{-1}).

The charge of nanoparticle surface depends on the pH and on the ionic force of the solution: the superficial electrical charge can be positive, negative and neutral as a function of the medium condition. Zero Point Charge (ZPC) corresponds to the pH value which the electrical charges cancel out [109]. ZPC depends on material nature and is represented as an average between the dissociation constants of species present on surface:

$$ZPC = \frac{pk_a^+ + pk_a^-}{2}$$

In the case of magnetite (Fig. 5.16), ZPC is around to 6.5 [110–112]. Below the ZPC, hydroxyl sites absorb the protons and become positive by the formation of $FeOH_2^+$ species. Above the ZPC, the protons are desorbed and the deprotonation leads to negative species Fe–O^-.

When iron oxide nanoparticles are put in contact with a solution, a biphasic system is created with solid/liquid interface. At this interface, some phenomena can appear and influence the colloidal stability, especially, the creation of a double electrical layer.

In the presence of water molecules, the surface can be hydrated by the surrounding water molecules. A water layer will thus be absorbed on nanoparticle

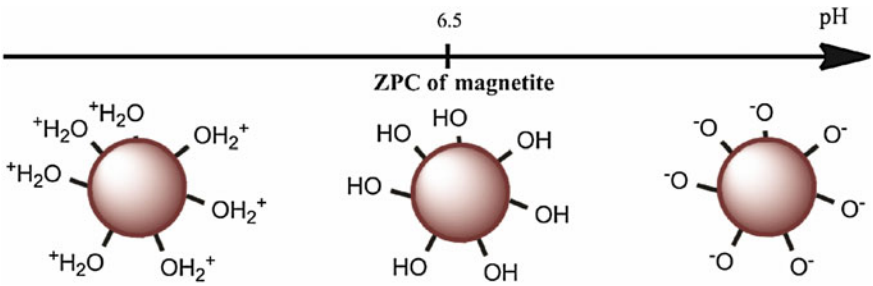

Fig. 5.16 Schematic representation of the charges present on nanoparticle surface as a function of pH

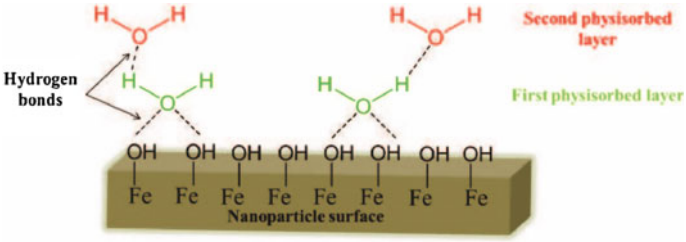

Fig. 5.17 Schematic representation of solvated surface of iron oxide nanoparticles

surface and the structure is stabilized by hydrogen bonds as shown in Fig. 5.17 [113]. Depending on the oxide nature, the thickness of solvated layer can vary from 1 to10 Å.

The surface depends on two parameters: the charge and the hydration states. However, it is also important to distinguish the difference between the ZPC and the isoelectric point (IEP). ZPC is the pH value at which the surface is neutral by the absence of positive or negative charges. On the contrary, the isoelectric point is the pH value when the surface charge is exactly offset by the counter-ions.

The structure of the double electrical layer is described by different models [114–119]. In our work, Stern model was used to explain the composition of the interface between the nanoparticles and the solution (Fig. 5.18). It is based on the models of Helmholtz and Gouy-Chapman. The double electrical layer is composed of two distinct layers: a **compact layer** (Stern layer) and a **diffuse layer** (Fig. 5.18b).

The compact film of the double electrical layer corresponds to the Stern layer in which the ions (H^+ or OH^-) can protonate or deprotonate the hydroxyl groups bonded on iron oxide surface. The Stern layer can be separated into two sets:

(A) The first part of Stern layer is composed of ions presenting a high affinity with surface. Their main role is to neutralize charges of the surface. These ions are away from the surface until a distance called Interne Helmholtz Plan (IHP).

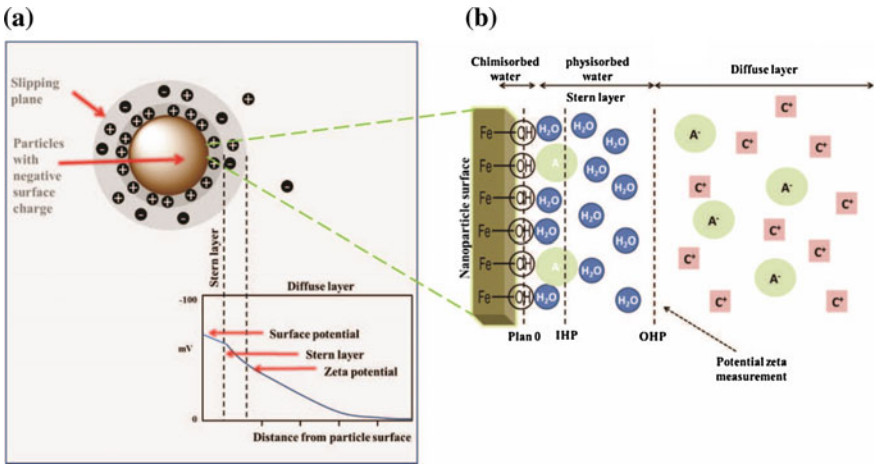

Fig. 5.18 **a** Schematic representation of the electrical double layer and the evolution of electrostatic potential as a function of the distance with negative charges on particle surface. **b** Schematic representation of the water absorption on the surface of iron oxide nanoparticles where A^- and C^+ are the anions and the cations present in solution respectively. IHP is the interne Helmholtz plan and OHP is the Outer Helmholtz plan. Wih pemission of Ref. [120]

(B) The second part of Stern layer can be considered as a frontier between the IHP layer and the diffuse layer. This layer is included in the Stern layer until the Outer Helmholtz Plan (OHP).

Beyond the Outer Helmholtz Plan, the second layer of the double electrical layer starts. This one is called the diffuse layer and is mainly composed of the counter ions. The global electric charge of the diffuse layer leads to the charge compensation, inducing the electric neutrality of the nanoparticles. These different layers explain why the hydrodynamic diameter of nanoparticles is always larger than the diameter measured by the transmission electron microscopy.

The electrostatic potential decreases as a function of the distance with the nanoparticle surface. However, this decrease is more affected by the Outer Helmholtz plan also called slipping plan as illustrated in Fig. 5.18a. At this plan, the potential observed is named the zeta potential (ξ). This value is the unique measurement of an observable and measurable potential. It is used as a reference to evaluate the stability of colloidal suspension.

The magnitude of zeta potential gives an indication of the stability of a nanoparticle suspension. In the case of a high value of zeta potential (negative or positive), the colloidal suspensions are stable and the presence of agglomerates is not observed. On the contrary, when low values of zeta potential are observed, flocculation generally occurs in solution. This parameter is strongly influenced by pH value. Zeta potential value varies and allows thus to estimate the pH region where the suspension is stable or not. At a given pH value, the zeta potential is close to zero when all charges are compensated by the counter-charged molecules versus

to the surface; this point is the isoelectric point (previously described). Although the pH is the most important factor influencing the zeta potential properties, the ionic strength of the media also affects the value of zeta potential, and especially, the nature of the ions interacting with the surface.

The thickness of the double layer depends on the ion concentrations in solution and can be correlated to the ionic strength of the medium. According to the ionic force, the double layer can be collapsed (at high ionic force) or extended (at low ionic force).

Two kinds of ions can interact with a charged surface:

- The **nonspecific ions** exhibit a low electrostatic interaction with the surface. When their concentrations increase in solution, the thickness of the electrical double layer is reduced without any effect on the value of the isoelectric point;
- The **specific ions** are attracted towards the surface with the electrostatic force inducing their adsorption on the surface and the isoelectric point is thus modified. In some cases, the adsorption of specific ions can affect the nature on charge surface.

The knowledge and the study of the surface state give indications on the stability of colloidal suspensions. Moreover, the measurements of zeta potential are generally used to confirm the surface modification process.

5.3.4 Stabilization Strategies

The surface of nanoparticle is the first area interacting with the body fluids when iron oxide suspensions are injected. This is the major reason why the nanoparticle surface is extensively studied and characterized. The problematic of uncoated nanoparticles is their trend to agglomerate. This explains why the development of stabilization methods are required to promote the repulsive forces between the particles that are opposed to attractive Van der Waals forces. The strategy generally used is to insert capping agents on nanoparticle surface.

Two complementary approaches can be envisaged: **electrostatic stabilization** and **steric stabilization** (Fig. 5.19) [121–124].

The goal of the surface protection is to decrease the interfacial energy in order to obtain a strong barrier that limits the distance of closest approach between nanoparticles. In the literature, the main coating agents are polymers (synthetic or naturals), small ionisable organic molecules, silica coating and biological molecules. Some examples are illustrated in Fig. 5.20.

The following part briefly describes some examples for each stabilizing agent.

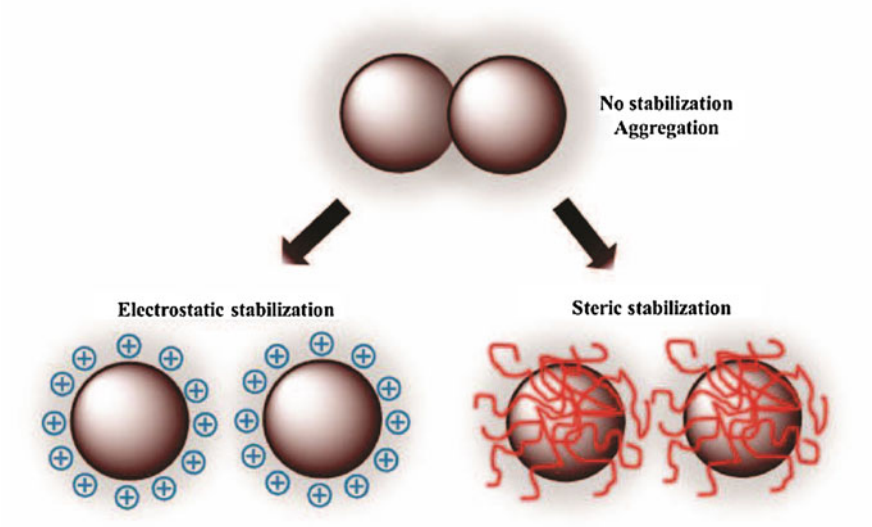

Fig. 5.19 Schematic representation of stabilization strategies: electrostatic and steric protections

Fig. 5.20 Summary of the main coating agents used for the stabilization of iron oxide nanoparticles

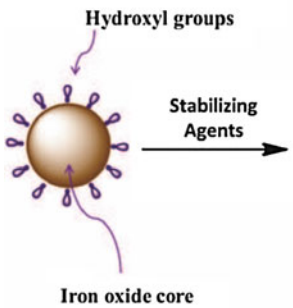

Natural polymers

Dextran	Gelatin
Chitosan	Pullulan

Synthetic polymers

Polyethylene Glycol	PEG
Polyvinyl Alcohol	PVA
Polystyrene	PS
Poly(vinylpyrrolidone)	PVP
Poly(acrylic acid)	PAA

Silica, silane

TEOS
Alkoxysilane

Small organic molecules

Carboxylate
Phosphate
Sulphate
phosphonate

Biological molecules

Avidin
Human serum albumin HSA

5.3.4.1 Silica

The most common strategy used for the surface modification is the formation of a silica shell. Protocols including trialkoxysilane molecules or tetraethyl orthosilicate (TEOS) are often reported [125]. The advantage of these molecules is that the silane groups can be covalently grafted onto nanoparticle surface through the reaction between the hydroxyl groups present on iron oxide surface and the alkoxysilane functions (–Si–O–R where R is methyl or ethyl groups) [126]. The cross-linking reactions induce the formation of a silica layer surrounding the particles [127]. A large choice of terminal functional groups (alcohol, amine, epoxy, thiol or carboxylate) [128–130] can be used to protect and stabilize iron oxide nanoparticles (Fig. 5.21).

Coating agents with precious metal (such as gold) can also provide an effective protection to avoid the surface oxidation and to reduce nanoparticle agglomeration in aqueous solution [132, 133].

5.3.4.2 Polymers

Another important and widely employed stabilizing agent is polymer (synthetic or natural). This type of coating allows a biocompatible and biodegradable surface but also improves the blood circulation times depending on the polymer nature [134, 135]. The polymers can be natural [136] or synthetic [134, 137].

One of the most used natural polymers is dextran [138]. This biocompatible and biodegradable polysaccharide can be strongly absorbed on nanoparticle surface, due to a strong interaction with hydrogen bonds formed between the hydroxyl functions on the polymer chains and the surface of iron oxide cores [139, 140]. Several MRI contrast agents have been elaborated with a dextran coating or its derivatives (carboxydextran and carboxymethyl dextran) [141–144]. Some dextran coatings are based on the cross-linked polymer after the nanoparticle attachment using epichlohydrin [145, 146]. The system has demonstrated a high circulation half-life in blood with no acute toxicity.

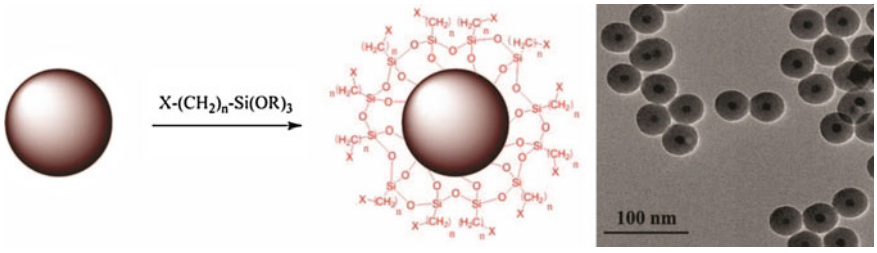

Fig. 5.21 General silica coating method and TEM images of silica coated iron oxide nanoparticles [131]

Duguet et al. [147–149] described the modification of the dextran structure with silane molecules. This strategy allows a covalent grafting on the surface. Other polymers can be used such as chitosan [150–152], gelatin [153], alginate [154] and pullulan [155] as stabilizing agents.

Another natural and biodegradable polymer, polylactic acid, has been used for the preparation of stable colloid suspension with a typical range of hydrodynamic diameter included between 10 and 180 nm [156, 157].

Among the synthetic polymers, the polyethylene glycol (PEG) is widely used due its properties such as the increase of the blood circulation time, the hydrophilicity and the biocompatibility. PEG can also be used for the coupling with other polymer to increase the hydrophilic properties. Two approaches are currently used to coat nanoparticles and consist in the addition of the surfactants during the synthetic process or post-synthesis. Other polymers and copolymers which have been used to coat magnetic nanoparticles are polyvinyl alcohol (PVA) [158, 159], polystyrene (PS) [160, 161], poly(vinylpyrrolidone) (PVP) [162, 163], poly(acrylic acid) (PAA) [164], poly(ethylenimine) (PEI) [165, 166], PAA-chitosan [167], …

5.3.4.3 Small Organic Molecules

Small organic molecules are frequently used to obtain stable colloidal suspension. The chemical functions used generally are carboxylates, phosphates and sulfates due to their high affinity for iron oxide surface. These strong interactions result from an ionic interaction between the acidic functions of the coating agents and the surface of nanoparticles. The most used carboxylic acids are citric and dimercaptosuccinic acids (Fig. 5.22) [168–172]. These polyacids form a stable colloidal suspension resulting from the high coordination on metal surface. However, the ionic bonds between the carboxylic functions and the iron oxide surface are labile and can be easily broken by the elevation of temperature or by carboxylic compounds presenting a much higher affinity with the surface.

Phosphate and phosphonate derivatives also are promising stabilizing molecules. Their absorption on metal surface is very stable and they are able to form a strong interaction in aqueous solution [173–176]. Bisphosphonate compounds (Fig. 5.22) are preferred in order to anchor double functions on the metal surface, involving the strengthening of the nanoparticle stability [177–179].

5.3.4.4 Biological Molecules

The stabilization performed by biological molecules is not a common method. Some examples describe the surface covering with proteins such as avidin [180] or human serum albumin (HSA) [181, 182]. This process allows the formation of stable and biocompatible magnetic fluids.

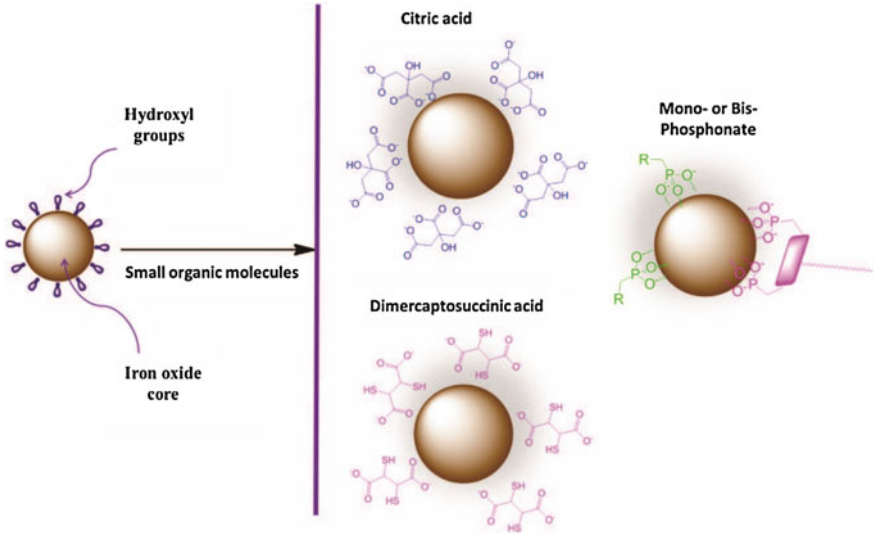

Fig. 5.22 Some examples of the nanoparticle stabilization with small organic molecules as citric acid, dimercaptosuccinic acid and mono- or bis-phosphonate molecules

5.3.5 Recent Advances on the Stabilization of Hydrophobic Iron Oxide Nanoparticles

The biocompatibility and the colloidal stability in water are primordial characteristics in order to use nanoparticles for clinical applications. Iron oxide nanoparticles synthesized in organic medium present the advantages to have controlled magnetic properties depending on the size and on the size distribution.

However, it is essential to modify the surface in hydrophilic one by the use of appropriate coating.

Two main ways are: **ligand addition** or **ligand exchange** (Fig. 5.23).

5.3.5.1 Stabilization by Ligand Addition

The ligand addition approach consists in the addition of amphiphilic molecules interacting with the initial stabilizing agent. The hydrophobic segments interact with the post-synthesis hydrophobic capping groups and the hydrophilic segments contribute to a better dispersion of nanoparticles in water. As a result, this interaction forms a double layer on the nanoparticle surface (Fig. 5.23). In this way, the stabilizing molecules are considered as phase transfer agents that allow the transition from an organic phase to an aqueous solution. The reported main surfactants

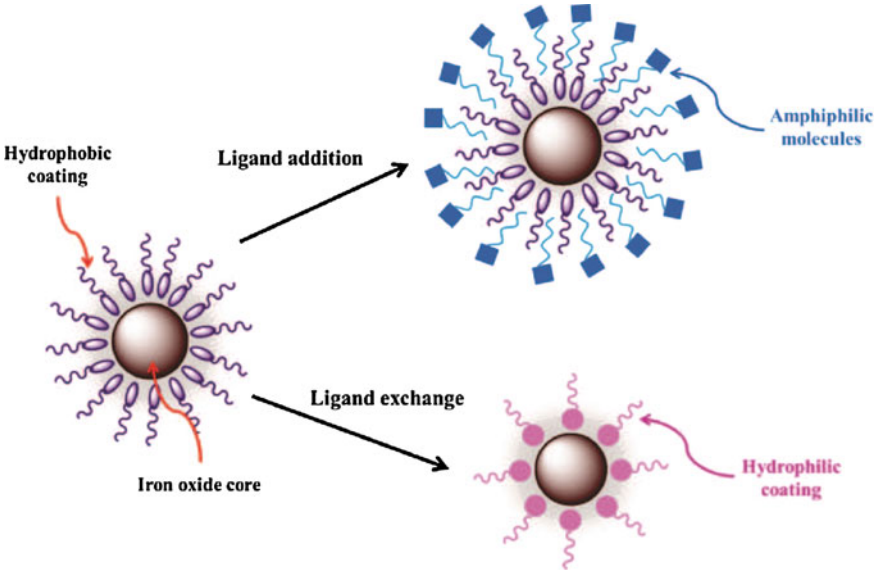

Fig. 5.23 Transfer of hydrophobic iron oxide nanoparticles in water media thanks to the ligand addition or ligand exchange

are polymers, alkylammonium salts and lipids; this part briefly describes some main examples.

Polymers

Many strategies have been developed using polymers as a surfactant. An example widely used is pluronic copolymers composed of a hydrophobic poly(propylene oxide) (PPO) chain flanked on each side with hydrophilic poly(ethylene oxide) (PEO) chains [183–187]. This is a triblock polymer (PEO-PPO-PEO) where hydrophobic PPO segments are located between the oleic acid chains and the PEG segments (Fig. 5.24).

Several similar processes have been described in the literature for diblock or triblock copolymers [188–192].

Alkylammonium Salts

Another common class of phase transfer agents is alkylammonium compounds. For example, cetyltrimethylammonium bromide (CTAB) is usually used [193, 194] as shown in Fig. 5.25.

A better water dispersion is observed when CTAB interacts with initial oleic acid coating. The nanoparticle size is inevitably increased.

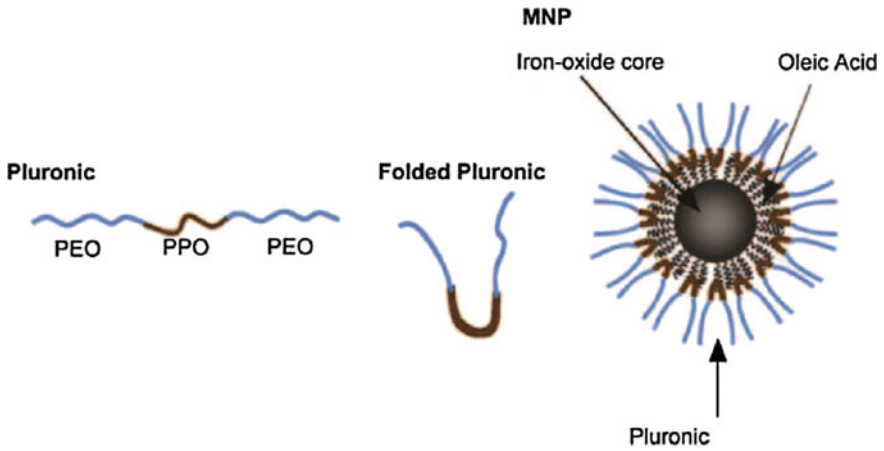

Fig. 5.24 Water stabilization of iron oxide nanoparticles by pluronic polymers (with permission of reference [184])

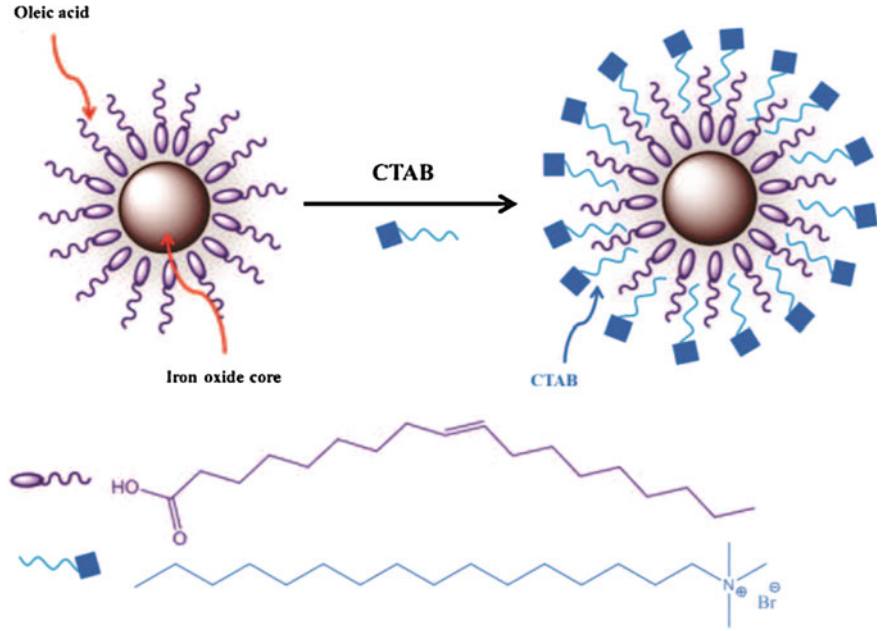

Fig. 5.25 Ligand addition of CTAB on oleic acid coated iron oxide nanoparticles

Lipids

A similar approach is exploited by the addition of lipids (Fig. 5.26) [195, 196] on nanoparticle surface. Phospholipids and fatty acids are the most widely used as amphiphilic ligands in order to transfer hydrophobic particles in water.

Deng et al. [197] reported a strategy to functionalize the hydrophobic surface of iron oxide nanoparticles with phospholipids such as 1,2-dioleyl-snglycero-3-phosphoethanolamin-*N*(succinyl) (carboxylated phospholipid). This coating was selected for several reasons. This phospholipid is amphiphilic, biocompatible and able to disperse nanoparticles in water when it interacts with long carbon chains initially present on nanoparticle surface. Other phospholipids as phosphatidyl-choline and phosphatidylethanolamine were also used [198].

Fatty acids (with 10–18 carbons) are also used to form a hydrophobic-hydrophilic bilayer for the transfer of hydrophobic nanoparticles in water [199, 200].

In summary, ligand addition transfers hydrophobic particles in water by the use of amphiphilic compounds (polymers, alkylammoniums, lipids, …). The strong hydrophobic interaction of amphiphilic molecules with nonpolar organic surface of nanoparticles leads to a complete encapsulation of the magnetic core and preserves the original coating. As a result, the agglomeration phenomena are generally minimized due to the conservation of the initial coating and a strong steric

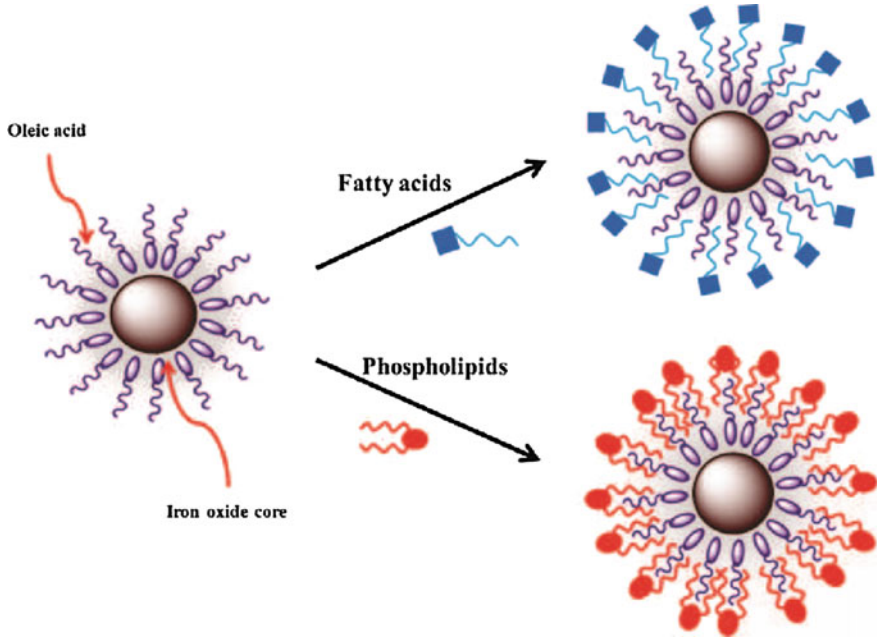

Fig. 5.26 Stabilization of hydrophobic nanoparticles by the use of fatty acids or phospholipids

stabilization. However, some drawbacks are observed such as the increase of nanoparticle size due to the addition of new coating and the destabilization of double layer by the elevation of temperature [159].

5.3.5.2 Stabilization by Ligand Exchange

Ligand exchange is defined as a replacement of initial capping agent with other coating, which is put onto the nanoparticle surface through exchange reactions. This approach is considered as a most versatile process to provide a better colloidal stability. According to the ligand nature, the link between the coating molecules and the nanoparticle surface can be covalent or ionic. In the following part, some major examples are described such as the ligand exchange by small charged molecules, by polymers or by silica.

Small Charged Molecules

The main small charged molecules are carboxylic acid derivatives. As previously described, the interaction between the nanoparticle surface and the carboxylic acid of oleic acid can be easily broken by temperature increase or by exchange with another carboxylic acid compound. An easy way is to select carboxylate molecules containing many carboxylic functions so that it could be anchored by two or more sites on the particle. Citric acid [159, 201] and dimercaptosuccinic acid (DMSA) [202–205] are the most widely used polyacids in which a multiple coordination of carboxylate functions on magnetic core can be observed. These ligands give a better stability in water by a strong ionic interaction.

Tetramethylammonium hydroxide (TMAOH) is a second common transfer agent used in order to replace oleic acid. This small molecule electrostatically stabilizes nanoparticles in water. The phase transfer is composed of a mixture between nanoparticles dispersed in non-polar solvent and an aqueous TMAOH solution. A double phase is created and the solution can be mixed either by magnetic agitation or by the use of ultrasounds [206–208].

These strategies are generally easy to perform. However, their stabilization is often not sufficient in order to conserve nanoparticle suspensions during long time storage.

Polymers

Polymers have been also widely used for the surface modification by ligand exchange. Firstly, the polymer chains can be attached on nanoparticle surface thanks to available chemical functions to create a strong interaction between the nanoparticles and the polymer.

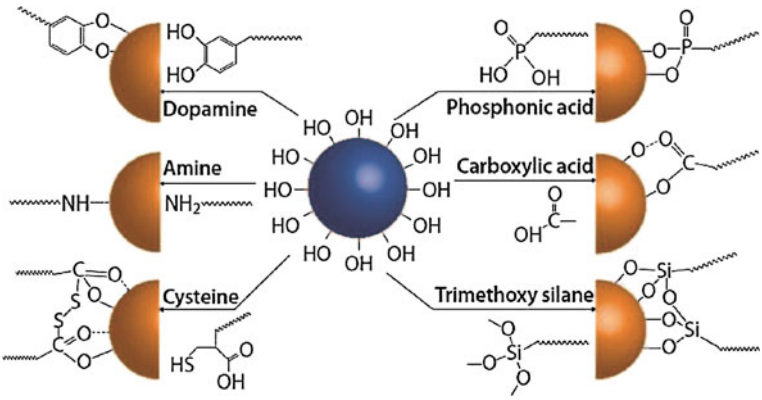

Fig. 5.27 Main chemical functions for the attachment of polymers on nanoparticle surface. With permission of Ref. [134]

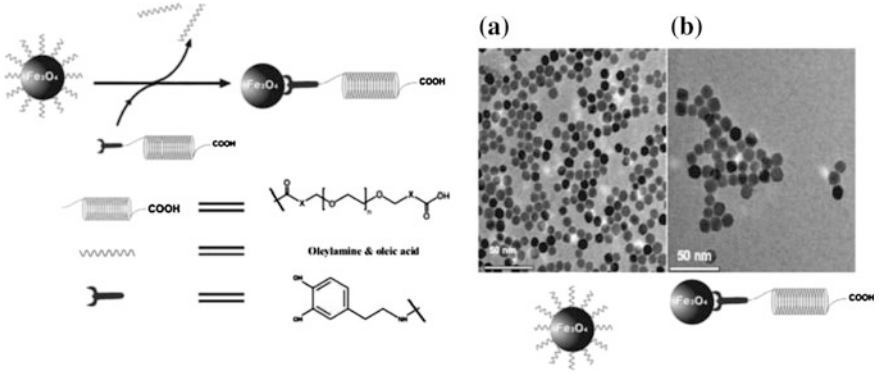

Fig. 5.28 Surface modification of oleic acid coated nanoparticles with dopamine modified PEG diacid and TEM images before and after their surface modification [212]

Several chemical functions [209] can be used to graft the polymer on the surface. Amongst others, we can quote dopamine [210–212], cysteine [213], phosphonic acid, carboxylic acid [214] and alkoxysilane [128, 129, 215] (Fig. 5.27).

As an example, the PEGylation of oleic acid coated nanoparticles can be performed via the reaction with dopamine modified PEG diacid (DPA-PEG-COOH) (Fig. 5.28). The first step is the modification of PEG diacid derivative with dopamine. Then, the resulting DPA-PEG-COOH is used to replace oleate compound and the particle surface is converted from hydrophobic to hydrophilic [212, 216].

Another method to form water-soluble iron oxide nanoparticles from the preparation of high thermal decomposition is to combine two ligand exchange strategies (Fig. 5.29) (small charged molecules and polymers) [159].

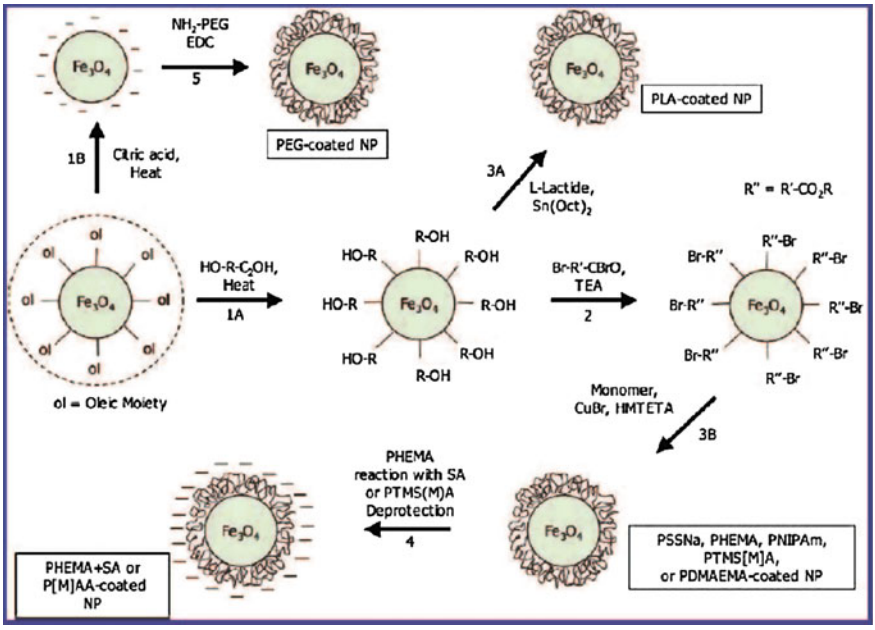

Fig. 5.29 General scheme of stabilization strategies described by Lattuada et al. [217]. Steps 1A and 1B: ligand exchange reactions with polyelectrolytes. Step 2: acylation of hydroxyl groups to prepare the surface with polymerization initiators. Step 3A: surface-initiated the polymerization with L-lactide. Step 3B: polymerization start up via the addition of monomers. Step 4: deprotection or additional reaction after polymerization. Step 5: grafting of end functionalized PEG chains onto nanoparticle surface using amidation chemistry. With permission of Ref. [217]

In the first steps, authors proposed the use of polyelectrolyte compounds such as ricinoleic acid or citric acid to remove oleic acid on nanoparticle surface, ensuring the nanoparticle dispersion in water (Fig. 5.29). The second step promotes the formation of a polymer shell. Two general pathways are described: (i) the first one links the polymer chains by the reaction of carboxylate functions available on nanocrystal surface or (ii) the polymerization process can be directly initiated on nanoparticle surface by addition of initiator.

Another alternative is to combine the effect of small charged molecules and polymers in using a unique compound. Short hydrophilic polyelectrolyte molecules such as poly(acrylic acid), poly(allylamine) or poly(sodium styrene sulfonate) exhibit several functional groups presenting a strong coordination on nanocrystal surface and are thus able to remove initial hydrophobic coating.

For example, Ge et al. [216, 218] proposes a simple process using polyacrylic acid. This method is performed at high temperature in glycol solvent (Fig. 5.30). Due to a high boiling point (245 °C), a high dissolving capability for polyelectrolytes and a high miscibility with water or with organic solvents, diethylene glycol is widely used.

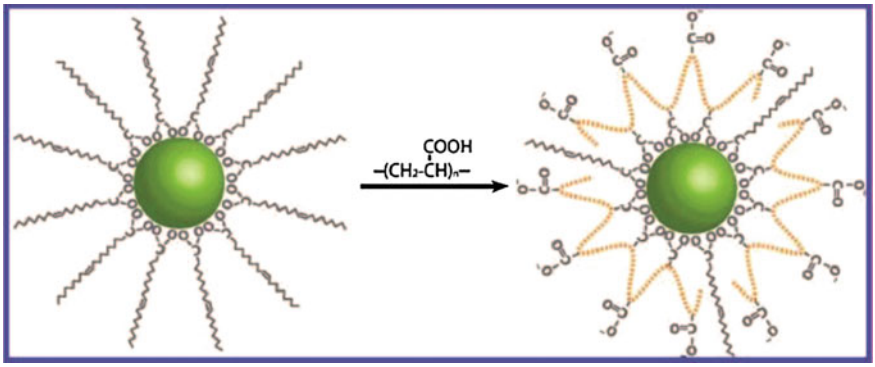

Fig. 5.30 Schematic representation of ligand exchange of oleic acid with polyacrylic acid in diethylene glycol [216, 218]. Reproduced with Ref. [216]

This approach presents several advantages such as:

- the high reaction temperature favors the desorption of oleic acid;
- the polyelectrolyte bonds are strong with multiple anchoring points on nanoparticle surface;
- due to the presence of the large quantities of the polar end functionalities, the final particles are water-soluble.

Silica

Silica coating is extensively used for nanoparticle stabilization in water. Indeed, silica shell is chemically inert and biocompatible [219]. Due to the ability to interact covalently with the surface, they are excellent candidates.

Major methods described in the literature for the silanization of hydrophobic nanoparticles can be separated into three general approaches:

- Direct silanization in non-polar solvents or a mixture of polar and non-polar solvents;
- Silanization by reverse microemulsion;
- Two-steps silanization: phase transfer followed by silanisation.

For the direct silanisation, several research groups proposed to replace oleic acid initially present on nanoparticle surface by organosilanes.

De Palma et al. [127] described a versatile method to functionalize the nanoparticles with different silane coupling agents. This group developed a method consisting in ligand exchange with oleic acid and silanes bearing different chemical end (Fig. 5.31). Briefly, the reaction occurs by the mixing of particles dispersed in n-hexane and selected trialkoxysilane in presence of acetic acid. The resulting solution is then mixed during three days at room temperature. Numerous silanes

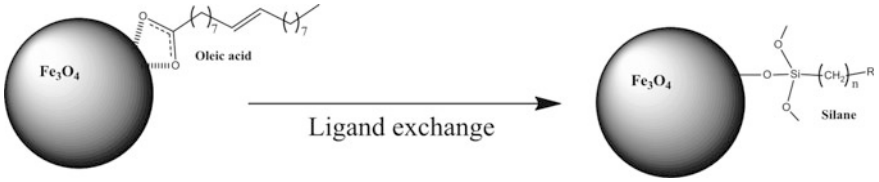

Fig. 5.31 Ligand exchange method to make hydrophilic iron oxide nanoparticles with silane agents. Reproduced with permission of Ref. [127]

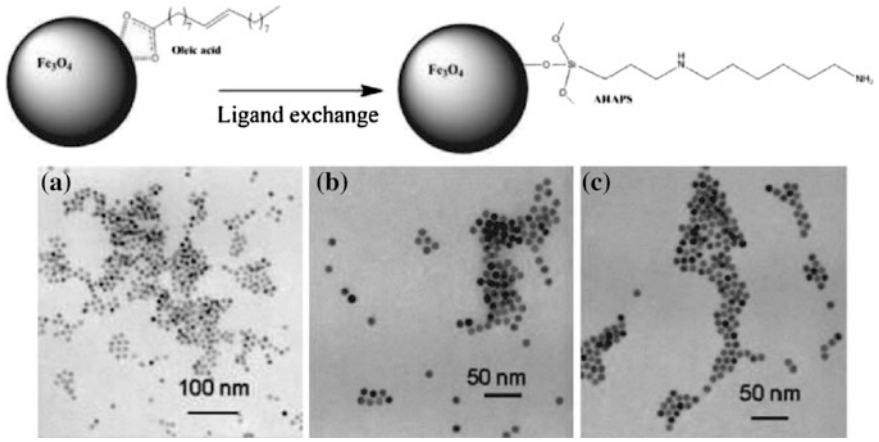

Fig. 5.32 TEM images of iron oxide nanoparticles stabilized with AHAPS from **a** THF, **b** ethanol or **c** water at pH = 3. With permission of Ref. [220]

with different chemical functions were used such as amine, aldehyde, thiol, carboxylic acid and cyano groups. The authors reported the efficient phase transfer of nanoparticles in water.

Another similar approach was proposed by Huang et al. [220]. The reaction is performed in tetrahydrofuran (THF) at 50 °C during a time varying from 100 to 210 min. Two types of silane were tested: *N*-(6-aminohexyl)-aminopropyl-trimethoxysilane (AHAPS) and 3-(triethoxysilyl)propylsuccinic anhydride (TEPSA). Interestingly, this strategy keeps the initial narrow size distribution (Fig. 5.32).

The ligand exchange with silane is time consuming. Therefore, Bloemen and collaborators [221] recently proposed an alternative method to reduce the reaction time. Thanks to the sonication during 5 h, the nanoparticles are dispersed in toluene and are mixed with trimethylamine and selected silane. After the reaction, a silane coating was formed.

Although the direct silanization is an efficient method to stabilize the nanoparticles, the control of the silica layer thickness is a poorly controlled parameter.

Consequently, the reverse microemulsion system was investigated in order to control this parameter. The reverse micelle system can be compared to nanoreactors allowing the control of the size, the shape and the reactant concentration.

Widely inspired by the works on hydrophobic semiconductor nanoparticles [222–225], Narita et al. [226] reported an easy method to control the silica layer thickness by tuning the reaction time and y limiting the reaction rate rather than by changing the solution components. Influenced by the reaction time and the pH, the thickness of silica layer can be tuned from 2 to 14 nm. However, the formation of silica coated particles with multiple magnetic cores has been observed.

Recently, Ding et al. [227] described a similar approach. The preparation of a single magnetic core encapsulated with different silica shell thicknesses for different size of iron oxide nanoparticles was reported. The reverse microemulsion system used is composed of five compounds: ammonia, igepal-CO520, TEOS, cyclohexane and the hydrophobic iron oxide nanoparticles. IgepalCO520 is an amphiphilic copolymer made of hydrophilic polyethyleneglycol chains and a short hydrophobic alkylphenyl derivative. It is used as a surfactant to form reverse micelle in cyclohexane.

TEOS can be used in order to initiate the formation of silica shell after its hydrolysis by ammonia in solution. The general reaction is illustrated in Fig. 5.33.

Thanks to the control of experimental parameters, authors demonstrated the ability to produce silane coated iron oxide nanoparticles with thickness control. Additionally, the silane coverage of magnetic particles presenting different sizes was also proven (Fig. 5.34).

Reverse microemulsion system is an efficient and innovative method to produce nanoparticles covered with a controlled silica shell. Although the silane thickness can be modulated, the preparation of a large quantity needs the use of large surfactant and solvent amounts. Moreover, nanoparticles initially prepared with TEOS

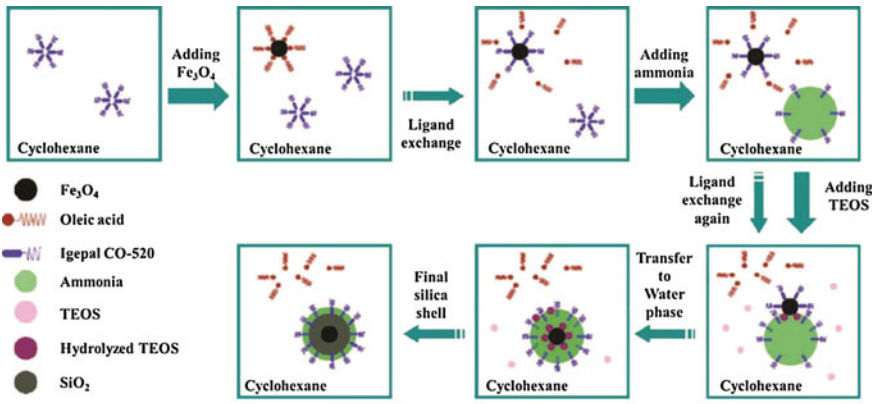

Fig. 5.33 Schematic representation of the silica coating mechanism on the surface of iron oxide nanoparticles via the reverse microemulsion method published by Ding et al., with permission of Ref. [227]

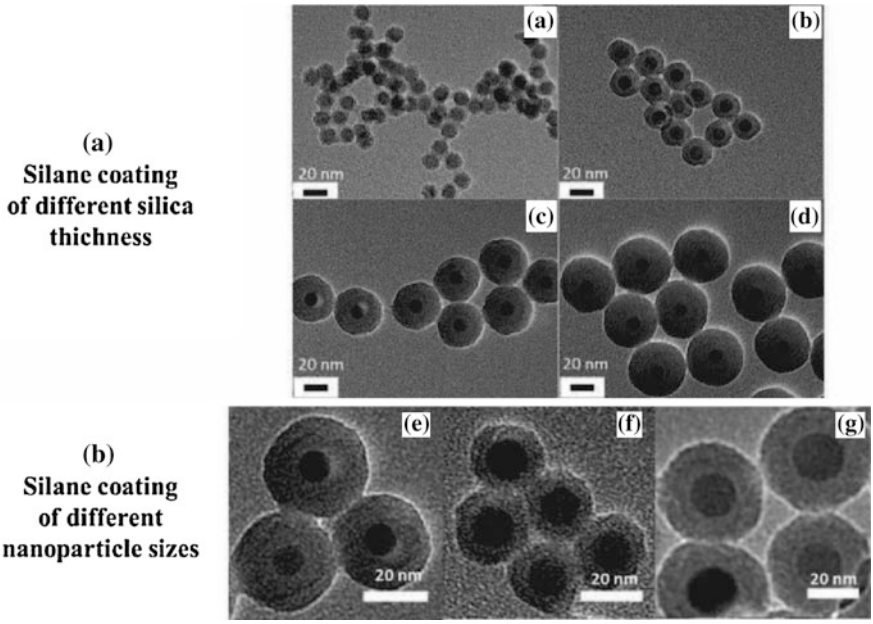

Fig. 5.34 TEM images of silica coated iron oxide nanoparticles: **a** with different silica shell thicknesses of 2 nm (*a*), 6.3 nm (*b*), 14.1 nm (*c*) and 19.8 nm (*d*) and **b** with magnetic core sizes of 10.1 nm (*e*), 13.5 nm (*f*) and 19.1 nm (*g*). With permission of Ref. [131]

often require an additional step in order to functionalize the surface for future targeting [226].

The last method uses two steps. Typically, the first step is a ligand exchange or a ligand addition in order to transfer hydrophobic particles in water. The second step involves the formation of silica shell.

For example, Kim et al. [193, 228] developed a two-steps method to modify hydrophobic nanoparticles with cetyltrimethylammonium bromide (CTAB) in order to disperse nanomaterials in water (Fig. 5.35). The carbon chains of CTAB interact

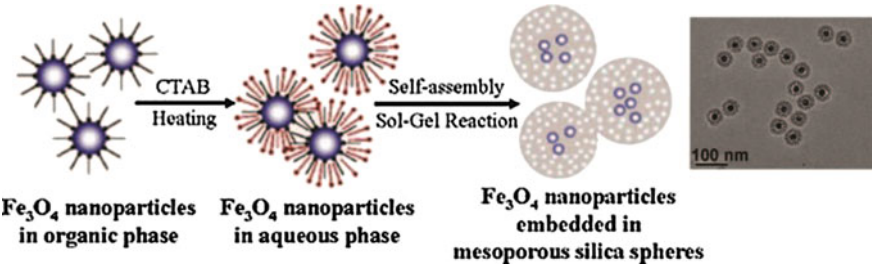

Fig. 5.35 Schematic representation of two-steps silanization and TEM image of the resulting materials. Reproduced with permission of Ref. [228]

with oleic acid chains through hydrophobic interactions and the polar group of CTAB (ammonium function) is oriented towards aqueous solution. This first step is a phase transfer via a ligand addition. The subsequent reaction is a ligand exchange in order to form silica coating by addition of TEOS performed in water medium.

Some authors used this method of phase transfer with polymers as a primary step before the silanization. As an example, Shen et al. [229] proposed the use of silane modified poly(ethylene glycol). Firstly, methoxy-poly(ethylene glycol) silane (MPEG-sil) replaces oleic acid. The nanoparticles are thus coated with polymer and can be dispersed in a more hydrophilic media. The silane function present on the polymer allows the formation of silica coating by the addition of TEOS.

In a similar way, it has been reported that the primary ligand exchange step can be also realized by poly(acrylic acid) (PAA) [230]. After the first ligand exchange, nanoparticles can be dispersed in an aqueous ethanol solution and then, the particles can be easily encapsulated with a uniform silica coating using TEOS as a silica source.

References

1. Corot C, Robert P, Idee J-M, Port M (2006) Recent advances in iron oxide nanocrystal technology for medical imaging. Adv Drug Deliv Rev 58:1471–1504
2. Laurent S, Forge D, Port M et al (2008) Magnetic iron oxide nanoparticles: synthesis, stabilization, vectorization, physico-chemical characterizations and biological applications. Chem Rev 108:2064–2110
3. Yu M, Jeong Y, Park J et al (2008) Drug-loaded superparamagnetic iron oxide nanoparticles for combined cancer imaging and therapy in vivo. Angew Chem Int Ed Engl 47:5362–5365
4. Duguet E, Mornet S, Portier J (2004) Aqueous dispersions of magnetic iron oxide particles, surface modified by covalently grafting amino groups, useful as MRI contrast agents stable against agglomeration at neutral pH. French patent FR2855315
5. Bragg WH (1915) The structure of magnetite and the spinels. Nature 95:561
6. Fleet ME (1986) The structure of magnetite: symmetry of cubic spinels. J Sol State Chem 62 (1):75–82
7. Evrim Umut. (2013). Surface modification of nanoparticles used in biomedical applications, modern surface engineering treatments. In Aliofkhazraei M (ed) ISBN: 978-953-51-1149-8, doi:10.5772/55746 (InTech)
8. Vestal CR, Zhang ZJ (2008) J Am Chem Soc 124:14312–14313
9. Gnanaprakash G, Panneerselvam G, Antony MP et al (2007) J Appl Phys 102:054305
10. Rondinone AJ, Samia ACS, Zhang ZJ (1999) J Phys Chem 103:6876–6880
11. Frenkel J, Doefman J (1930) Spontaneous and induced magnetisation in ferromagnetic bodies. Nature 126:274–275
12. Tartaj P, Serna CJ (2003) Synthesis of monodisperse superparamagnetic Fe/Silica nanospherical composites. J Am Chem Soc 125(51):15754–15755
13. Roch A, Gossuin Y, Muller RN, Gillis P (2005) Superparamagnetic colloid suspensions: water magnetic relaxation and clustering. J Magn Magn Mater 293(1):532–539
14. Dormann JL, Fiorani D, Tronc E (2007) Magnetic relaxation in fine-particle systems. Adv Chem Phys, pp 283–494
15. Laurent S, Forge D, Port M et al (2008) Magnetic iron oxide nanoparticles: synthesis, stabilization, vectorization, physicochemical characterizations, and biological applications. Chem Rev 108(6):2064–2110

16. Gossuin Y, Hocq A Gillis P et al (2009) Magnetic resonance relaxation properties of superparamagnetic particles. Wiley Interdisciplinary Rev Nanomed Nanobiotechnol 1 (3):299–310
17. Pérez N, Guardia N, Roca P et al (2008) Surface anisotropy broadening of the energy barrier distribution in magnetic nanoparticles. Nanotechnology 19(47):475704
18. Roch A, Gillis P, Ouakssim A, Muller RN (1999) Proton magnetic relaxation in superparamagnetic aqueous colloids: a new tool for the investigation of ferrite crystal anisotropy. J Magn Magn Mater 201(13):77–79
19. Roch A, Muller RN, Gillis P (1999) Theory of proton relaxation induced by superparamagnetic particles. J Chem Phys 110(11):5403–5411
20. Freed JH (1978) Dynamic effects of pair correlation functions on spin relaxation by translational diffusion in liquids. II. Finite jumps and independent T1 processes. J Chem Phys 68(9):4034–4037
21. Ayant Y, Belorizky E, Aluzon J, Gallice J (1975) Calcul des densités spectrales résultant d'un mouvement aléatoire de translation en relaxation par interaction dipolaire magnétique dans les liquides. Journal de Physique France 36(10):991–1004
22. Gao J, Gu H, Xu B (2009) Multifunctional magnetic nanoparticles: design, synthesis, and biomedical applications. Acc Chem Res 42(8):1097–1107
23. Gupta AK, Gupta M (2005) Synthesis and surface engineering of iron oxide nanoparticles for biomedical applications. Biomaterials 26(18):3995–4021
24. Reiss G, Hutten A (2005) Magnetic nanoparticles: applications beyond data storage. Nat Mater 4(10):725726
25. Carrillo AI, Serrano E, Luque R, García-Martínez J (2013) Microwave-assisted catalysis by iron oxide nanoparticles on MCM-41: effect of the support morphology. Appl Catal A Gen 453:383–390
26. Moodley P, Scheijen FJE, Niemantsverdriet JW, Thüne PC (2010) Iron oxide nanoparticles on flat oxidic surfaces—Introducing a new model catalyst for Fischer-Tropsch catalysis. Catal Today 154(1–2):142–148
27. Huang S-H, Juang R-S (2011) Biochemical and biomedical applications of multifunctional magnetic nanoparticles: a review. J Nanoparticle Res 13(10):4411–4430
28. Reddy LH, Arias JL, Nicolas J, Couvreur P (2012) Magnetic nanoparticles: design and characterization, toxicity and biocompatibility, pharmaceutical and biomedical applications. Chem Rev 112(11):5818–5878
29. Mahmoudi M, Sant S, Wang B, Laurent S, Sen T (2011) Superparamagnetic iron oxide nanoparticles (SPIONs): development, surface modification and applications in chemotherapy. Adv Drug Del Rev 63:24–46
30. Mersmann A (2001) Crystallization technology handbook, 2nd edn. Marcel Dekker Inc., New York, Basel
31. Massart R (1981) Preparation of aqueous magnetic liquids in alkaline and acidic media. Magnetics IEEE Trans 17(2):1247–1248
32. Sugimoto T, Matijević E (1980) Formation of uniform spherical magnetite particles by crystallization from ferrous hydroxide gels. J Coll Interface Sci 74(1):227–243
33. Babes L, Denizot B, Tanguy G (1999) Synthesis of iron oxide nanoparticles used as MRI contrast agents: a parametric study. J Coll Interface Sci 212(2):474–482
34. Pereira C, Pereira AM, Fernandes C et al (2012) Superparamagnetic MFe2O4 (M = Fe Co, Mn) nanoparticles: tuning the particle size and magnetic properties through a vovel one-step coprecipitation route. Chem Mater 24(8):1496–1504
35. Karaagac O, Kockar H (2012) Effect of synthesis parameters on the properties of superparamagnetic iron oxide nanoparticles. J Superconductivity Novel Magn 25(8): 2777–2781
36. Gupta AK, Curtis ASG (2004) Lactoferrin and ceruloplasmin derivatized superparamagnetic iron oxide nanoparticles for targeting cell surface receptors. Biomaterials 25(15):3029–3040

37. Kim DK, Zhang Y, Voitet W et al (2001) Synthesis and characterization of surfactant-coated superparamagnetic monodispersed iron oxide nanoparticles. J Magn Magn Mater 225(1–2):30–36
38. Tartaj P, Morales MP, Veintemillas-Verdaguer S et al (2006) Handbook of magnetic materials. North-Holland, Elsevier, p 403
39. LaMer VK, Dinegar RH (1950) Theory, production and mechanism of formation of monodispersed hydrosols. J Am Chem Soc 72(11):4847–4854
40. Malik MA, Wani MY, Hashim MA (2011) Microemulsion method: a novel route to synthesize organic and inorganic nanomaterials. 1st nano update. Arabian J Chem 5(4): 397–417
41. Massart R (1981) Preparation of aqueous magnetic liquids in alkaline and acidic media. IEEE Trans Magn 17:1247–1248
42. Massart R, Cabuil V (1987) Effect of some parameters on the formation of colloidal magnetite in alkaline medium: Yield and particle size control. J Chem Phys 84:967–973
43. Jolivet JP, Froidefond C, Pottier A et al (2004) Magnetic iron oxide nanoparticles: synthesis and applications. J Mater Chem 14(21):3281–3288
44. Jolivet JP, Vassiere L, Chaeneac C, Tronc E (1997) Mater Res Soc Symp Proc 432:145
45. Massart R, Roger J, Cabuil V (1995) New trends in chemistry of magnetic colloids: polar and non polar magnetic fluids, emulsions, capsules and vesicles. Braz J Phys 2:135–141
46. Jolivet JP, Belleville P, Tronc E, Livage J (1992) Influence of Fe(II) on the formation of the spinel iron-oxide in alkaline-medium. Clays Clay Miner 40:531–539
47. Qui X (2000) Synthesis and characterization of magnetic nano particles. Chin J Chem 18:834–837
48. Wu K, Kuo P, Yao Y, Tsai EH (2001) Magnetic and optical properties of Fe3O4 nanoparticle ferrofluids prepared by coprecipitation technique. IEEE Trans Magn 37: 2651–2653
49. Tang J, Myers M, Bosnick KA, Brus LE (2003) Magnetite Fe3O4 nanocrystals: spectroscopic observations of aqueous oxidation kinetics. J Phys Chem B 107:7501–7506
50. Sato T, Haneda K, Seki M, Iijima T (1990) Morphology and magnetic properties of ultrafine ZnFe2O4 particles. Appl Phys A 50:13–16
51. Alves CR, Aquino R, Sousa MH et al (2004) Low temperature experimental investigation of finite-size and surface effects in CuFe2O4 nanoparticles of ferrofluids. J Metastable Nanocryst Mater 20:694–699
52. Jolivet JP, Chaneac C, Tronc E (2004) Iron oxide chemistry. From molecular clusters to extended solid networks. Chem Commun 5:481–483
53. Mao Z, Kang E, Wang S et al (2006) Synthesis of magnetite octahedrons from iron powders through a mild hydrothermal method. Mater Res Bull 41:2226–2231
54. Zhu H, Yang D, Zhu L (2007) Hydrothermal growth and characterization of magnetite (Fe3O4) thin films. Surf Coat Technol 201:5870–5874
55. Willard MA, Kurihara LK, Carpenter EE et al (2004) Encyclopedia of nanoscience and nanotechnology. American Scientific Publishers, Stevenson Ranch, p 815252
56. Chen D, Xu R (1998) Hydrothermal synthesis and characterization of nanocrystalline Fe_3O_4 powders. Mater Res Bull 33:1015–1021
57. Zheng YH, Cheng Y, Bao F, Wang YS (2006) Synthesis and magnetic properties of Fe3O4 nanoparticles. Mater Res Bull 41(3):525–529
58. Hyeon T, Lee SS, Park J, Chung Y, Na HB (2001) Synthesis of highly crystalline and monodisperse maghemite nanocrystallites without a size-selection process. J Am Chem Soc 123:12798–12801
59. Sun S, Zeng H, Robinson DB et al (2003) Monodisperse MFe2O4 (M = Fe Co, Mn) nanoparticles. J Am Chem Soc 126:179–273
60. Woo K, Hong J, Ahn JP (2005) Synthesis and surface modification of hydrophobic magnetite to processible magnetite@silica-propylamine. J Magn Magn Mater 293:177–181
61. Park J, Lee E, Hwang NM et al (2005) One-nanometer-scale size-controlled synthesis of monodisperse magnetic iron oxide nanoparticles. Angew Chem Inter Ed 44(19):2873–2877

62. Li Z, Sun Q, Gao M (2004) Preparation of water-soluble magnetite nanocrystals from hydrated ferric salts in 2-pyrrolidone: mechanism leading to Fe3O4. Angew Chem Inter Ed 44(1):123–126
63. Wan J, Cai W, Feng J et al (2007) In situ decoration of carbon nanotubes with nearly monodisperse magnetite nanoparticles in liquid polyols. J Mater Chem 17:1188–1192
64. Jun YW, Huh YM, Choi JS et al (2005) Nanoscale size effect of magnetic nanocrystals and their utilization for cancer diagnosis via magnetic resonance imaging. J Am Chem Soc 127 (16):5732–5733
65. Amara D, Felner I, Nowik I, Margel S (2009) Synthesis and characterization of Fe and FeO4 nanoparticles by thermal decomposition of triiron dodecacarbonyl. Coll Surf A Physicochem Eng Aspects 339:106–110
66. Caruntu D, Remond Y, Chou NH, Jun MJ (2002) Reactivity of 3d transition metal cations in diethylene glycol solutions. Synthesis of transition metal ferrites with the structure of discrete nanoparticles complexed with long-chain carboxylate anions. Inorg Chem 41: 6137–6146
67. Caruntu D, Caruntu G, Yuxi C et al (2004) Synthesis of variable-sized nanocrystals of Fe3O4 with high surface reactivity. Chem Mater 16:5527–5534
68. Li Z, Chen H, Bao H, Gao M (2004) One-pot reaction to synthesize water-soluble magnetite nanocrystals. Chem Mater 16:1391–1393
69. Li Z, Wei L, Gao M, Lei H (2005) One-pot reaction to synthesize biocompatible magnetite nanoparticles. Adv Mater 17:1001–1005
70. Hu F, Wei L, Zhou Z, Ran Y, Li Z, Gao M (2006) Preparation of biocompatible magnetite nanocrystals for in vivo magnetic resonance detection of cancer. Adv Mater 18:2552–2556
71. Adireddy S, Lin C, Palshin V (2009) Size-controlled synthesis of quasi-monodisperse transition-metal ferrite nanocrystals in fatty alcohol solutions. J Phys Chem C 113: 20800–20811
72. Jun Y-W, Lee J-H, Cheon J (2008) Chemical design of nanoparticle probes for high-performance magnetic resonance imaging. Angew Chem Inter Ed 47:5122–5135
73. Gupta AK, Gupta M (2005) Synthesis and surface engineering of iron oxide nanoparticles for biomedical applications. Biomaterials 26:3995–4021
74. Lam UT, Mammucari R, Suzuki K, Foster NR (2008) Processing of iron oxide nanoparticles by supercritical fluids. Ind Eng Chem Res 47(3):599–614
75. Tavakoli A, Sohrabi M, Kargari A (2007) A review of methods for synthesis of nanostructured metals with emphasis on iron compounds. Chem Papers 61(3):151–170
76. Del Monte F, Morales MP, Levy D et al (1997) Formation of γ-Fe_2O_3 isolated nanoparticles in a silica matrix. Langmuir 13:3627–3634
77. Niznansky D, Rehspringer JL, Drillon M (1994) Preparation of magnetic nanoparticles (gamma-Fe2O3) in the silica matrix. IEEE Trans Magn 30:821–823
78. Bentivegna F, Ferré J, Nyvlt M et al (1998) Magnetically textured y-Fe2O3 nanoparticles in a silica gel matrix: structural and magnetic properties. J Appl Phys 83:7776–7786
79. Pileni MP (1993) Reverse micelles as microreactors. J Phys Chem 97(27):6961–6973
80. Lawrence MJ, Rees GD (2000) Microemulsion-based media as novel drug delivery systems. Adv Drug Del Rev 45(1):89–121
81. Fendler JH (1987) Atomic and molecular clusters in membrane mimetic chemistry. Chem Rev 87:877–899
82. Sugimoto T (1987) Preparation of monodispersed colloidal particles. Adv Coll Interface Sci 28:65–108
83. Vidal-Vidal J, Rivas J, López-Quintela MA (2006) Synthesis of monodisperse maghemite nanoparticles by the microemulsion method. Colloid Surf A, pp 44–51
84. Jézéquel D, Guenot J, Jouini N, Fiévet F (1995) Submicrometer zinc-oxide nanoparticles—Elaboration in polyol medium and morphological characteristics. J Mater Res 10:77–83
85. Fievet F, Fievet-Vincent F, Lagier JP et al (1992) Preparation de particules monodisperses de cobalt et de nickel de taille micronique et submicronique. J Phys IV 02(C3):91

86. Tzitzios VK, Petridis D, Zafiropoulou I et al (2005) Synthesis and characterization of L10 FePt nanoparticles from Pt–Fe3O4 core-shell nanoparticle. J Magn Magn Mater 294(2): 95–98
87. Joseyphus RJ, Kodama D, Matsumoto T et al (2007) Role of polyol in the synthesis of Fe particles. J Magn Magn Mater 310(2):2393–2395
88. Cai W, Wan J (2007) Facile synthesis of superparamagnetic magnetite nanoparticles in liquid polyols. J Coll Interface Sci 305:366–370
89. Pascal C, Pascal JL, Favier F et al (1999) Electrochemical synthesis for the control of γ-Fe_2O_3 nanoparticle size. Morphology, microstructure, and magnetic behavior. Chem Mater 11:141–147
90. Veintemillas-Vendaguer S, Morales MP, Bomati-Miguel O et al (2004) Colloidal dispersions of maghemite nanoparticles produced by laser pyrolysis with application as NMR contrast agents. J Phys 37:2054–2059
91. Alexandrescu R, Morjan I, Voicu I et al (2005) Combining resonant/non-resonant processes: nanometer-scale iron-based material preparation via CO_2 laser pyrolysis. Appl Surf Sci 248 (1–4):138–146
92. Bautista MC, Bomati-Miguel O, Moraleset MP et al (2005) Surface characterisation of dextran-coated iron oxide nanoparticles prepared by laser pyrolysis and coprecipitation. J Magn Magn Mater 293:20–27
93. Puntes VF, Krishnan KM, Alivisatos AP (2002) Synthesis of colloidal cobalt nanoparticles with controlled size and shapes. Top Catal 19:145–148
94. Rotstein HG, Tannenbaum R (2002) Cluster coagulation and growth limited by surface interactions with polymers. J Phys Chem B 106:146–151
95. Mukh-Qasem RA, Gedanken A (2005) Sonochemical synthesis of stable hydrosol of Fe3O4 nanoparticles. J Coll Interface Sci 284(2):489–494
96. Kim EH, Lee HS, Kwak BK, Kim BK (2005) Synthesis of ferrofluid with magnetic nanoparticles by sonochemical method for MRI contrast agent. J Magn Magn Mater 289:328–330
97. Cosgrove T (2010). In: Cosgrove T (ed) Colloid science: principles, methods and applications. Wiley, USA
98. Derjaguin B (1940) On the repulsive forces between charged colloid particles and on the theory of slow coagulation and stability of lyophobe sols. Trans Faraday Soc 35:203–215
99. Derjaguin B, Landau L (1993) Theory of the stability of strongly charged lyophobic sols and of the adhesion of strongly charged particles in solutions of electrolytes. Progr Surf Sci 43 (1–4):30–59
100. Derjaguin BV (1993) Some new aspects of and conclusions on theory of stability of colloids and their experimental verification. Progr Surf Sci 43(1–4):115–121
101. Derjaguin BV, Voropayeva TN, Kabanov BN, Titiyevskaya AS (1993) Surface forces and the stability of colloids and disperse systems. Progr Surf Sci 43(1–4):83–105
102. Verwey EJW (1935) The electrical double layer and the stability of lyophobic colloids. Chem Rev 16(3):363415
103. Verwey EJW (1947) Theory of the stability of lyophobic colloids. J Phys Coll Chem 51 (3):631–636
104. Verwe EJW, Overbeek JTG (1955) Theory of the stability of lyophobic colloids. J Coll Sci 10(2):224–225
105. Wu I, Risalvato FG, Ke F-S et al (2012) Electrochemical reduction of carbon dioxide I. Effects of the electrolyte on the selectivity and activity with Sn electrode. J. Electrochem Soc 159(7):F353–F359
106. Leong YK, Ong BC (2003) Critical zeta potential and the Hamaker constant of oxides in water. Powder Technol 134(3):249–254
107. Hogg R, Healy TW, Fuerstenau DW (1966) Mutual coagulation of colloidal dispersions. Trans Faraday Soc 62:1638–1651
108. Boström M, Williams D, Ninham B (2001) Specific ion effects: Why DLVO theory fails for biology and colloid systems. Phys Rev Lett 87(16):168103

109. Parks GA, De Bruyn PL (1962) The zero point of charge of oxide 1. J Phys Chem 66 (6):967973
110. Haines RI, Owen DG, Vandergraaf TT (1987) Technetium-iron oxide reactions under anaerobic conditions: a Fourier transform infrared, FTIR study. Nucl J Can 1(1):32–37
111. Milonjić SK, Kopečni MM, Ilić ZE (1983) The point of zero charge and adsorption properties of natural magnetite. J Radioanal Chem 78(1):15–24
112. Tewari PH, McLean AW (1972) Temperature dependence of point of zero charge of alumina and magnetite. J Coll Inter Sci 40(2):267–272
113. Jolivet JP, Tronc E, Chanéac C (2000) Synthesis of iron oxide- and metal-based nanomaterials. Eur Phys J App Phys 10:167–172
114. Anandarajah A, Chen J (1994) Double-layer repulsive force between two inclined platy particles according to the Gouy-Chapman theory. J Coll Interface Sci 168(1):111–117
115. Baldelli S (2008) Surface structure at the ionic liquid–electrified metal interface. Acc Chem Res 41(3):421–431
116. Bohinc K, Shrestha A, Brumen M, May S (2012) Poisson-Helmholtz-Boltzmann model of the electric double layer: analysis of monovalent ionic mixtures. Phys Rev E 85(3):031130
117. Hu Y (1998) Effects of an inner Helmholtz layer on the dielectric dispersion of colloidal suspensions. Langmuir 14(2):271–276
118. Yates DE, Levine S, Healy TW (1974) Site-binding model of the electrical double layer at the oxide/water interface. J Chem Soc Faraday Trans 1 Phys Chem Cond Phases 70:18071818
119. Usui S (2004) Interaction between dissimilar double layers with like signs under charge regulation on the basis of the Gouy–Chapman–Stern–Grahame model. J Colloid Interface Sci 280(1):113–119
120. Devanathan MAV, Tilak BVKSRA (1965) The structure of the electrical double layer at the metal-solution interface. Chem Rev 65(6):635–684
121. Kuchibhatla S, Karakoti AS, Sea S (2005) Colloidal stability by surface modification. JOM 57(12):52–56
122. Napper DH (1970) Colloid stability. Ind Eng Chem Prod Res Dev 9(4):467477
123. Napper DH, Netschey A (1971) Studies of the steric stabilization of colloidal particles. J Coll Interface Sci 37(3):528–535
124. Napper DH (1977) Steric stabilization. J Coll Interface Sci 58(2):390–407
125. Roca AG, Costo R, Rebolledo AF et al (2009) Progress in the preparation of magnetic nanoparticles for applications in biomedicine. J Phys D Appl Phys 42(22):224002
126. Lee H, Yu MK, Park S, Moon S et al (2007) Thermally cross-linked superparamagnetic iron oxide nanoparticles: synthesis and application as a dual imaging probe for cancer in vivo. J Am Chem Soc 129(42):12739–12745
127. De Palma R, Peeters S, Van Bael MJ et al (2007) Silane ligand exchange to make hydrophobic superparamagnetic nanoparticles water-dispersible. Chem Mater 19(7): 1821–1831
128. Kohler N, Fryxell GE, Zhang M (2004) A bifunctional poly(ethylene glycol) silane immobilized on metallic oxidebased nanoparticles for conjugation with cell targeting agents. J Am Chem Soc 126(23):72067211
129. Larsen EKU, Nielsen T, Wittenborn T et al (2009) Size-dependent accumulation of PEGylated silanecoated magnetic iron oxide nanoparticles in murine tumors. ACS Nano 3 (7):1947–1951
130. Ninjbadgar T, Brougham DF (2011) Epoxy ring opening phase transfer as a general route to water dispersible superparamagnetic Fe_3O_4 nanoparticles and their application as positive MRI contrast agents. Adv Funct Mater 21(24):4769–4775
131. Pinho SLC, Laurent S, Rocha J et al (2011) Relaxometric studies of γ-Fe_2O_3@SiO_2 core shell nanoparticles: when the coating matters. J Phys Chem C 116(3):2285–2291
132. Carpenter EE, Sangregorio C, O'Connor CJ (1999) Effects of shell thickness on blocking temperature of nanocomposites of metal particles with gold shells. IEEE Trans Magn 35 (5):3496–3498

133. Maleki H, Simchi A, Imani M, Costa BFO (2012) Size-controlled synthesis of superparamagnetic iron oxide nanoparticles and their surface coating by gold for biomedical applications. J Magn Magn Mater 324(23):3997–4005
134. Boyer C, Whittaker MR, Bulmus V et al (2010) The design and utility of polymer-stabilized iron-oxide nanoparticles for nanomedicine applications. NPG Asia Mater 2:23–30
135. Forge D, Roch A, Laurent S et al (2008) Optimization of the synthesis of superparamagnetic contrast agents by the design of experiments method. J Phys Chem C 112(49):19178–19185
136. Dias AMGC, Hussain A, Marcos AS, Roque ACA (2011) A biotechnological perspective on the application of iron oxide magnetic colloids modified with polysaccharides. Biotechn Adv 29(1):142–155
137. Chanana M, Mao WD (2009) Using polymers to make up magnetic nanoparticles for biomedicine. J Biomed Nanotechnol 5(6):652–668
138. Yun Tack L, Kyoungja W, Kyu-Sil C (2008) Preparation of water-dispersible and biocompatible iron oxide nanoparticles for MRI agent. IEEE Trans Nanotechnol 7(2):111–114
139. Bautista CM, Bomati-Miguel O, Del Puerto MM et al (2005) Surface characterisation of dextrancoated iron oxide nanoparticles prepared by laser pyrolysis and coprecipitation. J Magn Magn Mater 293(1):20–27
140. Easo SL, Mohanan PV (2013) Dextran stabilized iron oxide nanoparticles: synthesis, characterization and in vitro studies. Carbohydr Polym 92(1):726–732
141. Rosen JE, Chan L, Shieh D-B, Gu FX (2012) Iron oxide nanoparticles for targeted cancer imaging and diagnostics. Nanomed Nanotechnol Biol Med 8(3):275–290
142. Weissleder R, Hahn PF, Stark DD et al (1987) MR imaging of splenic metastases: ferrite-enhanced detection in rats. Am J Roentgenol 149(4):723–726
143. Weissleder R, Stark DD, Engelstad BL et al (1989) Superparamagnetic iron oxide: pharmacokinetics and toxicity. Am J Roentgenol 152(1):167–173
144. Corot C, Robert P, Idée J-M, Port M (2006) Recent advances in iron oxide nanocrystal technology for medical imaging. Adv Drug Del Rev 58(14):1471–1504
145. Josephson L, Tung C-H, Moore A, Weissleder R (1999) High-efficiency intracellular magnetic labeling with novel superparamagnetic-Tat peptide conjugates. Bioconjugate Chem 10(2):186–191
146. McCarthy JR, Weissleder R (2008) Multifunctional magnetic nanoparticles for targeted imaging and therapy. Adv Drug Del Rev 60(11):1241–1251
147. Deng J, He J, Zheng J-S et al (2012) Preparation and application of amino- and dextran-modified superparamagnetic iron oxide nanoparticles. Part Sci Technol 31(3):241–247
148. Duguet E, Vasseur S, Mornet S et al (2006) Towards a versatile platform based on magnetic nanoparticles for in vivo applications. Bull Mater Sci 29(6):581–586
149. Mornet S, Portier J, Duguet E (2005) A method for synthesis and functionalization of ultrasmall superparamagnetic covalent carriers based on maghemite and dextran. J Magn Magn Mater 293(1):127–134
150. Chaleawlert-Umpon S, Mayen V, Manotham K, Pimpha N (2010) Preparation of iron oxide-entrapped chitosan nanoparticles for stem cell labeling. J Biomater Sci Polym Ed 21 (11):1515–1532
151. Szpak A, Kania G, Skórka T et al (2012) Stable aqueous dispersion of superparamagnetic iron oxide nanoparticles protected by charged chitosan derivatives. J Nanoparticle Res 15 (1):1–11
152. Tsai Z-T, Wang J-F, Kuo H-Y et al (2010) In situ preparation of high relaxivity iron oxide nanoparticles by coating with chitosan: a potential MRI contrast agent useful for cell tracking. J Magn Magn Mater 322(2):208–213
153. Gaihre B, Khil MS, Lee DR, Kim HY (2009) Gelatin-coated magnetic iron oxide nanoparticles as carrier system: drug loading and in vitro drug release study. Int J Pharm 365 (1–2):180–189
154. Ma H-L, Qi X-R, Maitani Y, Nagai T (2007) Preparation and characterization of superparamagnetic iron oxide nanoparticles stabilized by alginate. Int J Pharm 333 (1–2):177–186

155. Gao F, Cai Y, Zhou J et al (2010) Pullulan acetate coated magnetite nanoparticles for hyper-thermia: preparation, characterization and in vitro experiments. Nano Res 3(1):23–31
156. Cheng F-Y, Wang SP-H, Su C-H et al (2008) Stabilizer-free poly(lactide-co-glycolide) nanoparticles for multimodal biomedical probes. Biomaterials 29(13):2104–2112
157. Lee S-J, Jeong J-R, Shin S-C et al (2004) Nanoparticles of magnetic ferric oxides encapsulated with poly(D,L latide-co-glycolide) and their applications to magnetic resonance imaging contrast agent. J Magn Magn Mater 272–276:2432–2433 (Part 3(0))
158. Mahmoudi M, Simchi A, Imani M et al (2008) Optimal design and characterization of superparamagnetic iron oxide nanoparticles coated with polyvinyl alcohol for targeted delivery and imaging. J Phys Chem B 112(46):14470–14481
159. Zhou L, He B, Zhang F (2011) Facile one-pot synthesis of iron oxide nanoparticles cross-linked magnetic poly(vinyl alcohol) gel beads for drug delivery. ACS Appl Mater Interfaces 4(1):192–199
160. Garcia I, Tercjak A, Zafeiropoulos NE et al (2007) Generation of core/shell iron oxide magnetic nanoparticles with polystyrene brushes by atom transfer radical polymerization. J Polym Sci Part A Polym Chem 45(20):4744–4750
161. Wang Y, Teng X, Wang J-S, Yang H (2003) Solvent-free atom transfer radical polymerization in the synthesis of Fe_2O_3@polystyrene core–shell nanoparticles. Nano Lett 3(6):789–793
162. Bae S-J, Park J-A, Lee J-J et al (2009) Ultrasmall iron oxide nanoparticles: synthesis, physicochemical, and magnetic properties. Curr Appl Phys 9(1):19–21
163. Lee HY, Lim NH, Seo JA et al (2006) Preparation and magnetic resonance imaging effect of polyvinylpyrrolidone-coated iron oxide nanoparticles. J Biomed Mater Res Part B Appl Biomater 79B(1):142–150
164. Xu Y-Y, Zhou M, Geng H-J et al (2012) A simplified method for synthesis of Fe_3O_4@PAA nanoparticles and its application for the removal of basic dyes. Appl Surf Sci 258(8): 3897–3902
165. Masotti A, Pitta A, Ortaggi G et al (2009) Synthesis and characterization of polyethylenimine-based iron oxide composites as novel contrast agents for MRI. Magn Reson Mater Phys Biol Med 22(2):77–87
166. Wang Z, Liu G, Sun J et al (2012) N-alkyl-polyethylenimine stabilized iron oxide nanoparticles as MRI visible transfection agents. J Nanosci Nanotechnol 12(2):879–886
167. Ge Y, Zhang S, He S et al (2009) Fabrication and characterization of chitosan-poly(acrylic acid) magnetic nanospheres. J Nanosci Nanotechnol 9(2):1287–1290
168. Fauconnier N, Pons JN, Roger J, Bee A (1997) Thiolation of maghemite nanoparticles by dimercaptosuccinic acid. J Coll Interface Sci 194(2):427–433
169. Lattuad M, Hatton TA (2006) Functionalization of monodisperse magnetic nanoparticles. Langmuir 23(4):21582168
170. Maurizi L, Bisht H, Bouyer F, Millot N (2009) Easy route to functionalize iron oxide nanoparticles via long-term stable thiol groups. Langmuir 25(16):8857–8859
171. Miguel-Sancho N, Bomatí-Miguel O, Colom G et al (2011) Development of stable, water-dispersible, and biofunctionalizable superparamagnetic iron oxide nanoparticles. Chem Mater 23(11):2795–2802
172. Răcuciu M, Creangă DE, Airinei A (2006) Citric-acid-coated magnetite nanoparticles for biological applications. Eur Phys J 21(2):117–121
173. Benbenishty-Shamir H, Gilert R, Gotman I et al (2011) Phosphonate-anchored monolayers for antibody binding to magnetic nanoparticles. Langmuir 27(19):12082–12089
174. Daou TJ, Begin-Colin S, Grenèche JM et al (2007) Phosphate adsorption properties of magnetite-based nanoparticles. Chem Mater 19(18):4494–4505
175. Daou TJ, Grenèche JM, Pourroy G et al (2008) Coupling agent effect on magnetic properties of functionalized magnetite-based nanoparticles. Chem Mater 20(18):5869–5875
176. Guerrero G, Mutin PH, Vioux A (2001) Anchoring of phosphonate and phosphinate coupling molecules on titania particles. Chem Mater 13(11):4367–4373

177. Karimi A, Denizot B, Passirani C et al (2013) In vitro and in vivo evaluation of superparamagnetic iron oxide nanoparticles coated by bisphosphonates: the effects of electrical charge and molecule length. Eur J Pharm Sci 49(2):101–108
178. Lalatonne Y, Paris C, Serfaty JM et al (2008) Bis-phosphonates-ultra small superparamagnetic iron oxide nanoparticles: a platform towards diagnosis and therapy. Chem Commun 22:2553–2555
179. Portet D, Denizot B, Rump E et al (2001) Comparative biodistribution of thin-coated iron oxide nanoparticles TCION: effect of different bisphosphonate coatings. Drug Dev Res 54 (4):173–181
180. Park J-A, Lee J-J, Kim I-S et al (2008) Magnetic and MR relaxation properties of avidin–biotin conjugated superparamagnetic nanoparticles. Coll and Surfaces A Physicochem Eng Aspects 313–314:288–291
181. Quan Q, Xie J, Gao H et al (2011) HSA coated iron oxide nanoparticles as drug delivery vehicles for cancer therapy. Mol Pharm 8(5):1669–1676
182. Xie J, Wang J, Niu G et al (2010) Human serum albumin coated iron oxide nanoparticles for efficient cell labeling. Chem Commun 46(3):433–435
183. Gonzales M, Krishnan KM (2007) Phase transfer of highly monodisperse iron oxide nanocrystals with Pluronic F127 for biomedical applications. J Magn Magn Mater 311 (1):59–62
184. Jain TK, Foy SP, Erokwu B et al (2009) Magnetic resonance imaging of multifunctional pluronic stabilized iron-oxide nanoparticles in tumor-bearing mice. Biomaterials 30 (35):6748–6756
185. Jain TK, Morales MA, Sahoo SK et al (2005) Iron oxide nanoparticles for sustained delivery of anticancer agents. Mol Pharm 2(3):194–205
186. Morales MA, Jain TK, Labhasetwar V, Leslie-Pelecky DL (2005) Magnetic studies of iron oxide nanoparticles coated with oleic acid and Pluronic block copolymer. J Appl Phys 97 (10):10Q903–10Q905
187. Qin J, Asempah I, Laurent S et al (2009) Injectable superparamagnetic ferrogels for controlled release of hydrophobic drugs. Adv Mater 21(13):1354–1357
188. Muir BW, Moffat BA, Harbour P et al (2009) Combinatorial discovery of novel amphiphilic polymers for the phase transfer of magnetic nanoparticles. J Phys Chem C 113(38): 16615–16624
189. Park J, Yu MK, Jeong YY et al (2009) Antibiofouling amphiphilic polymer-coated superparamagnetic iron oxide nanoparticles: synthesis, characterization, and use in cancer imaging in vivo. J Mater Chem 19(35):6412–6417
190. Pimpha N, Chaleawlert-Umpon S, Sunintaboon P (2012) Core/shell polymethyl methacrylate/polyethyleneimine particles incorporating large amounts of iron oxide nanoparticles prepared by emulsifier-free emulsion polymerization. Polymer 53(10): 2015–2022
191. Prakash A, Zhu H, Jones CJ et al (2009) Bilayers as phase transfer agents for nanocrystals prepared in nonpolar solvents. ACS Nano 3(8):2139–2146
192. William WY, Emmanuel C, Christie MS et al (2006) Aqueous dispersion of monodisperse magnetic iron oxide nanocrystals through phase transfer. Nanotechnology 17(17): 4483–4487
193. Kim J, Lee JE, Lee J et al (2005) Magnetic fluorescent delivery vehicle using uniform mesoporous silica spheres embedded with monodisperse magnetic and semiconductor nanocrystals. J Am Chem Soc 128(3):688–689
194. Wang X, Chen Y (2008) A new two-phase system for the preparation of nearly monodisperse silver nanoparticles. Mater Lett 62(28):4366–4368
195. Shen L, Laibinis PE, Hatton TA (1998) Bilayer surfactant stabilized magnetic fluids: synthesis and interactions at interfaces. Langmuir 15(2):447–453
196. Wooding A, Kilner M, Lambrick DB (1991) Studies of the double surfactant layer stabilization of water-based magnetic fluids. J Coll Interface Sci 144(1):236–242

197. Deng M, Tu N, Bai F, Wang L (2012) Surface functionalization of hydrophobic nanocrystals with one particle per micelle for bioapplications. Chem Mater 24(13):2592–2597
198. Thanh NTK, Green LAW (2010) Functionalisation of nanoparticles for biomedical applications. Nano Today 5(3):213–230
199. Ingram DR, Kotsmar C, Yoon KY et al (2010) Superparamagnetic nanoclusters coated with oleic acid bilayers for stabilization of emulsions of water and oil at low concentration. J Coll Interface Sci 351(1):225–232
200. Li L, Mak KY, Leung CW et al (2012) Synthesis and characterization of self-assembled monolayer and bilayer carboxyl-group functionalized magnetic nanoparticles. IEEE Trans Magn 48(11):3299–3302
201. Bittova B, Poltierova-Vejpravova J, Roca AG et al (2010) Effects of coating on magnetic properties in iron oxide nanoparticles. J Phys Conf Ser 200(7):072012
202. Haddad PS, Martins TM, D'Souza-Li L et al (2008) Structural and morphological investigation of magnetic nanoparticles based on iron oxides for biomedical applications. Mater Sci Eng C 28(4):489–494
203. Roca AG, Veintemillas-Verdaguer S, Port M et al (2009) Effect of nanoparticle and aggregate size on the relaxometric properties of MR contrast agents based on high quality magnetite nanoparticles. J Phys Chem B 113(19):7033–7039
204. Salas G, Casado C, Teran FJ et al (2012) Controlled synthesis of uniform magnetite nanocrystals with high-quality properties for biomedical applications. J Mater Chem 22 (39):21065–21075
205. Yihang W, Mengjie S, Zhuang X et al (2011) Ultra-small particles of iron oxide as peroxidase for immunohistochemical detection. Nanotechnology 22(22):225703
206. Guardia P, Pérez N, Labarta A, Batlle X (2009) Controlled synthesis of iron oxide nanoparticles over a wide size range. Langmuir 26(8):5843–5847
207. Salgueiriño-Maceira V, Liz-Marzán LM, Farle M (2004) Water-based ferrofluids from Fe_xPt_{1-x} nanoparticles synthesized in organic media. Langmuir 20(16):6946–6950
208. Taboada E, Rodríguez E, Roig A et al (2007) Relaxometric and magnetic characterization of ultrasmall iron oxide nanoparticles with high magnetization. Evaluation as potential T_1 magnetic resonance imaging contrast agents for molecular imaging. Langmuir 23(8): 4583–4588
209. Smolensky ED, Park H-YE, Berquó TS, Pierre VC (2011) Surface functionalization of magnetic iron oxide nanoparticles for MRI applications—Effect of anchoring group and ligand exchange protocol. Contrast Media Mol Imaging 6(4):189–199
210. Na HB, Palui G, Rosenberg JT et al (2011) Multidentate catechol-based polyethylene glycol oligomers provide enhanced stability and biocompatibility to iron oxide nanoparticles. ACS Nano 6(1):389–399
211. Peng S, Wang C, Xie J, Sun S (2006) Synthesis and stabilization of monodisperse Fe nanoparticles. J Am Chem Soc 128(33):10676–10677
212. Xie J, Xu C, Kohler N et al (2007) Controlled PEGylation of monodisperse Fe_3O_4 nanoparticles for reduced non-specific uptake by macrophage cells. Adv Mater 19(20): 3163–3166
213. Huang G, Zhang C, Li S et al (2009) A novel strategy for surface modification of superparamagnetic iron oxide nanoparticles for lung cancer imaging. J Mater Chem 19 (35):6367–6372
214. Kyoungja W, Hong J (2005) Surface modification of hydrophobic iron oxide nanoparticles for clinical applications. IEEE Trans Magn 41(10):4137–4139
215. Fang C, Bhattarai N, Sun C, Zhang M (2009) Functionalized nanoparticles with long-term stability in biological media. Small 5(14):1637–1641
216. Ge J, Hu Y, Biasini M et al (2007) One-step synthesis of highly water-soluble magnetite colloidal nanocrystals. Chem A Eur J 13(25):7153–7161
217. Lattuada M, Hatton TA (2006) Functionalization of monodisperse magnetic nanoparticles. Langmuir 23(4):2158–2168

218. Zhang T, Ge J, Hu Y et al (2007) A general approach for transferring hydrophobic nanocrystals into water. Nano Lett 7(10):3203–3207
219. Tartaj P, González-Carreño T, Serna CJ (2001) Single-step nanoengineering of silica coated maghemite hollow spheres with tunable magnetic properties. Adv Mater 13(21):1620–1624
220. Huang X, Schmucker A, Dyke J et al (2009) Magnetic nanoparticles with functional silanes: evolution of well-defined shells from anhydride containing silane. J Mater Chem 19 (24):4231–4239
221. Bloemen M, Brullot W, Luong T et al (2012) Improved functionalization of oleic acid-coated iron oxide nanoparticles for biomedical applications. J Nanoparticle Res 14 (9):1–10
222. Darbandi M, Lu W, Fang J, Nann T (2006) Silica encapsulation of hydrophobically ligated PbSe nanocrystals. Langmuir 22(9):4371–4375
223. Darbandi M, Urban G, Krüger M (2010) A facile synthesis method to silica coated CdSe/ZnS nanocomposites with tuneable size and optical properties. J Coll Interface Sci 351 (1):30–34
224. Masih D, Frank S, Joachim L et al (2012) Nanoscale size effect on surface spin canting in iron oxide nanoparticles synthesized by the microemulsion method. J Phys D Appl Phys 45 (19):195001
225. Selvan ST, Tan TT, Ying JY (2005) Robust, non-cytotoxic, silica-coated CdSe quantum dots with efficient photoluminescence. Adv Mater 17(13):1620–1625
226. Narita A, Naka K, Chujo Y (2009) Facile control of silica shell layer thickness on hydrophilic iron oxide nanoparticles via reverse micelle method. Coll Surf A Physicochem Eng Aspects 336(1–3):4656
227. Ding H, Zhang Y, Wang S et al (2012) Fe_3O_4@SiO_2 core/shell nanoparticles: the silica coating regulations with a single-core for different core sizes and shell thicknesses. Chem Mater 24(23):4572–4580
228. Kim J, Kim HS, Lee N et al (2008) Multifunctional uniform nanoparticles composed of a magnetite nanocrystal core and a mesoporous silica shell for magnetic resonance and fluorescence imaging and for drug delivery. Angew Chem 120(44):8566–8569
229. Shen R, Camargo PHC, Xia Y, Yang H (2008) Silane-based poly(ethylene glycol) as a primer for surface modification of nonhydrolytically synthesized nanoparticles using the Stöber method. Langmuir 24(19):11189–11195
230. Dai Q, Lam M, Swanson S et al (2010) Monodisperse cobalt ferrite nanomagnets with uniform silica coatings. Langmuir 26(22):17546–17551

Chapter 6
MRI Applications: Classification According to Their Biodistribution

Abstract MRI contrast agents are known for about 30 years. Most of clinical compounds are extracellular agents without tissue specificity. They are excreted by the kidneys (Gd-DTPA, Gd-DOTA, Gd-DTPA-BMA or Gd-HP-DO3A for example). More recently, intracellular agents (Gd-EOB-DTPA, Gd-BOPTA, … undergoing hepatocyte uptake), and blood pool contrast agent (MS-325, binding albumin) have been developed. These Gd complexes have an extended clearance time and allow longer contrast-enhanced imaging sessions. These systems are called "T_1 or positive" agents because they increase the water signal of the tissue areas where they are concentrated. A second kind of contrast agents is made of superparamagnetic iron oxide nanoparticles (USPIO or SPIO). These nanosystems have a high efficiency and are generally "T_2 or negative" agents, inducing a darkening of the region where they accumulate. Such nanoparticles with a diameter of approximately 20–200 nm can be used as contrast agents for liver, lymphatic system (because of macrophage uptake, mainly as negative agent), or blood vessels (because of low extravasation, mainly as positive agent). The different kinds of mechanisms through which they affect the nuclear magnetic relaxation time of the water are briefly described. Nowadays, researches are focused on the development of molecular imaging contrast agents, to target receptors which are overexpressed in pathologies.

The classification of contrast agents according to their distribution in the body may also be considered. [1].

S. Laurent et al., *MRI Contrast Agents*, Nanotheranostics,
DOI 10.1007/978-981-10-2529-7_6

6.1 Non-specific Agents (Interstitial Diffusion of Gadolinium Complexes)

6.1.1 Toxicity of Free Gadolinium and Gd-Complexes

Gadolinium ions have extremely high toxicity. Precipitation of gadolinium chloride at physiological pH results in blockage of the reticuloendothelial system (liver toxicity). On the other hand, the Gd^{3+} ions compete with the calcium at the level of myocardial contractility, the coagulation, the Ca^{2+} dependent enzymes, mitochondrial respiration and neurotransmission. [2].

In order to be injected, the toxicity of gadolinium must be greatly reduced by complexing the Gd^{3+} ion with an organic ligand. Chelates (or ligands) have little effect on the paramagnetic properties of gadolinium as they leave free a coordination site for water molecules.

Complexation with chelate does not involve covalent bonds, a release of the gadolinium ion in vivo is still possible. Six linear or macrocyclic commercial chelates, ionic or nonionic (Fig. 6.1) have r_1 and r_2 relaxivities of the same order of magnitude (Table 6.1) but some differences can be observed in terms of stability, dissociation constants, decomplexation rate or osmolarity.

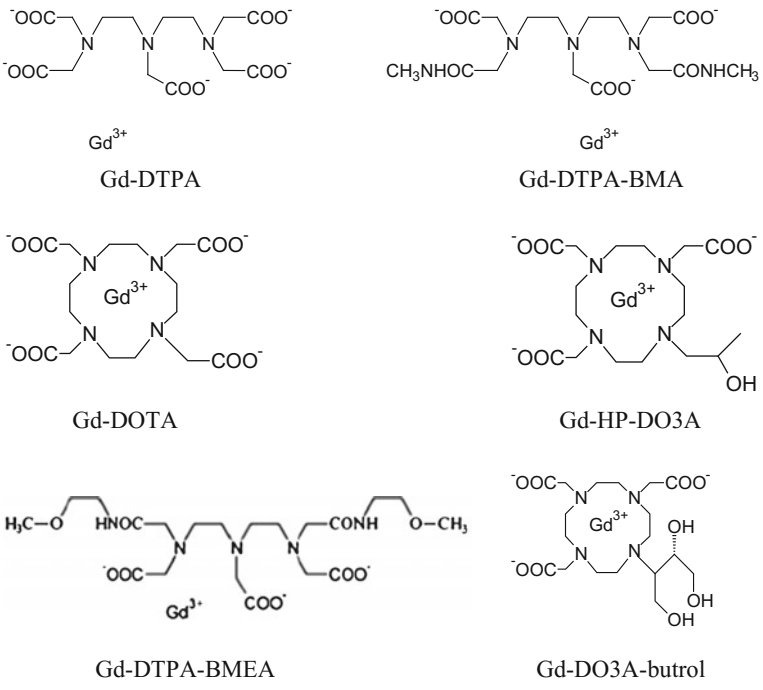

Fig. 6.1 Structure of the non specific clinically-accepted Gd-complexes

Table 6.1 Extracellular contrast agents in clinical use

Contrast agents	Relaxivity (s^{-1} mM^{-1}) at 1.5 T and 37 °C
Gd-DTPA, gadopentetate dimeglumine Magnevist®, Schering AG, Germany	r_1 = 3.3 r_2 = 3.9
Gd-DTPA-BMA, gadodiamide Omniscan®, GE-Healthcare, USA	r_1 = 3.3 r_2 = 3.6
Gd-DTPA-BMEA, gadoversetamide Optimark®, Mallinckrodt, USA	r_1 = 3.8 r_2 = 4.2
Gd-DOTA, gadoterate meglumine Dotarem®, Guerbet, France	r_1 = 2.9 r_2 = 3.2
Gd-HP-DO3A, gadoteridol ProHance®, Bracco, Italy	r_1 = 2.9 r_2 = 3.2
Gd-BT-DO3A, gadobutrol Gadovist®, Schering AG, Germany	r_1 = 3.3 r_2 = 3.9

Gd gadolinium; *DTPA* diethylenetriaminepentaacetic acid

The release of free Gd ion depends on the affinity of the metal for the ligand. It is measured by the selectivity constant and by the thermodynamic constant.

The kinetics of decomplexation is much slower for the macrocyclic complexes (Gd-DOTA, Gd-HP-DO3A, Gd-DO3A-BT) than for the linear compounds (Gd-DTPA, Gd-DTPA-BMA, Gd-DTPA-BMEA). If the residence time in the body is much less than the decomplexation half-life, the compound is completely eliminated even before it could release free Gd ions and the affinity constant becomes less important. In fact, decomplexation kinetics and affinity constant are related. Macrocyclic chelates exhibit both a high affinity constant and very long decomplexation kinetics.

In theory, if a chelate dissociation occurs in vivo, free Gd ions could express their toxicity and free chelate could fix other ions that have a constant in the same order than that of gadolinium affinity. In particular, there may be a chronic chelation of zinc, or acute toxicity by calcium chelation.

The affinity constant for the different calcium chelates is weak in comparison with that of gadolinium, the risk of transmetallation is low. With zinc, the risk is more important [3]. In vitro transmetallation test has also been developed recently [4].

After intravenous injection, Gd-DTPA and Gd-DOTA diffuse rapidly in the extracellular space and are then excreted by the kidney exclusively by glomerular filtration. They do not bind to albumin and do not cross the healthy blood-brain barrier. Their plasma half-life is about 90 min. Pharmacokinetics is very close to that of iodinated contrast media used in radiology. They result in an increase of signal (T_1 effect). The T_2 effect (signal decrease) is observable only in the excretory bladder or renal cavities wherein the compound is highly concentrated.

Figure 6.2 shows another example of MR images obtained after injection of Gd-HP-DO3A. A slice at the level of the heart shows the contrast medium in blood vessels. The clinical safety of these agents is excellent, with less than 1 % minor

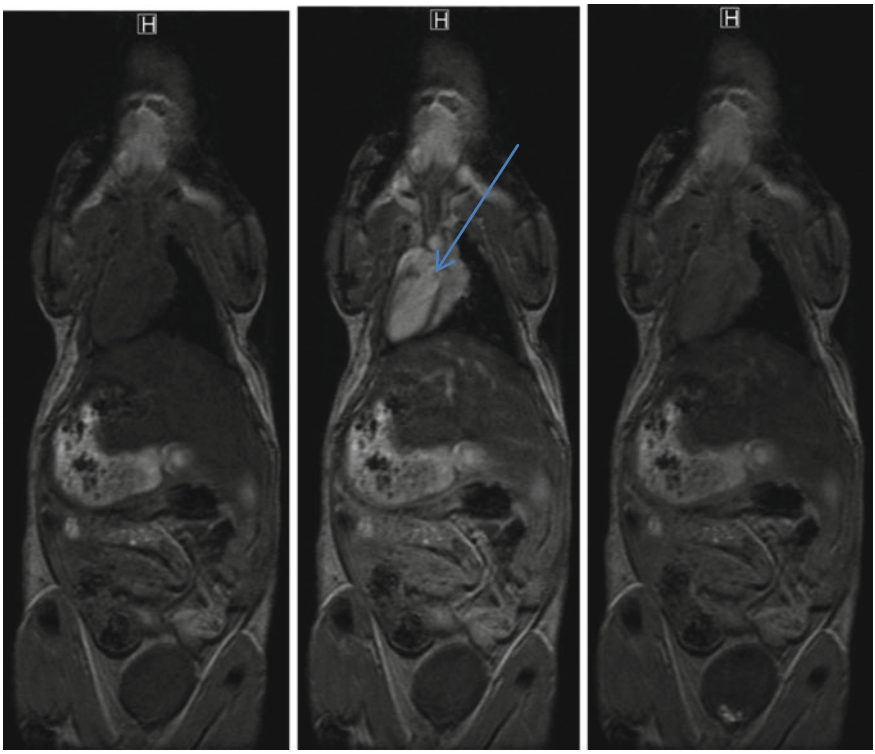

Fig. 6.2 MR images; pre-contrast, one minute, and 5 min after iv injection of Gd-HP-DO3A, gadoteridol (ProHance®) at a dose of 45 micromoles/kg. The presented slice shows the heart (*arrow*) enhanced by the presence of contrast medium in blood vessels of a mouse (with permission of Ref. [6])

effects and exceptional anaphylactoid reactions that do not justify the systematic premedication in allergic patients [5].

6.1.2 NSF Disease [7–14]

Many cases of nephrogenic systemic fibrosis (NSF) (or nephrogenic fibrosing dermopathy, NFD) were observed in patients with renal insufficiency who underwent MRI with intravenous Gd chelates. Nephrogenic systemic fibrosis results in fibrosis of certain tissues such as skin, skeletal muscle, pleura, pericardium and myocardium. This is particularly important in fibrosis of the skin where it can limit movement and causing disability. Renal failure is now considered by many as contraindication for injection of Gd complexes. Several cases of NSF have been reported in association with three contrast agents: Omniscan®, Magnevist® and

Optimark®. A majority of reported cases have been associated with exposure to Omniscan®. No case has been reported in association with macrocyclic Gd complex. The pathophysiology of this disease remains unclear and therefore the link between cause and effect cannot be determined with certainty. However, this link appears possible because researchers have demonstrated the presence of Gd in skin biopsies of patients with NSF disease. The differences in stability between the reported Gd chelates could explain the disease in patients with severe renal impairment and in which the persistence of contrast agent is the longest. The stability of the Gd chelates is linked to their macrocyclic structure.

6.2 Hepatic Agents

The interest of liver contrast agents is to improve liver tissue characterization for better detectability of lesions. There are several types of contrast agents for the liver [15, 16].

6.2.1 Gadolinium Complexes with Biliary Excretion: Gd-EOB-DTPA and Gd-BOPTA

By adding a side chain containing a benzene ring on the Gd-DTPA complex, a more lipophilic compound (Gd-BOPTA and Gd-EOB-DTPA) (Fig. 6.3), which allows specific capture by the liver is obtained [17, 18]. After passage through the hepatocytes, they are excreted by the bile. These paramagnetic agents induce a significant enhancement of the liver by increasing the signal of more than 200 %. Thus an increase in contrast is obtained between a tumor and the healthy liver. Indeed, a tumor lacking the organic anion transporter system which allows for contrast agent uptake will remain hypointense relative to the liver [19, 20]. With

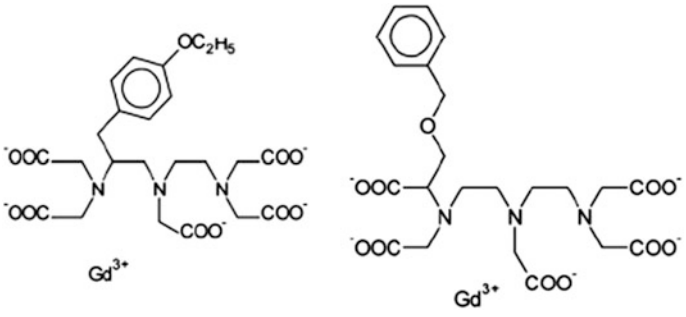

Fig. 6.3 Structure of the Gd-EOB-DTPA and Gd-BOPTA

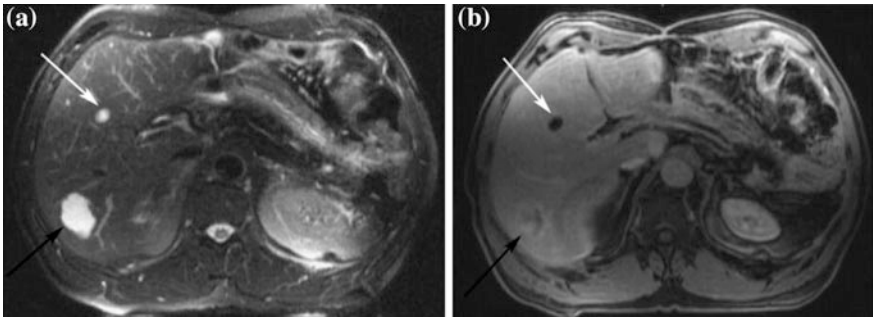

Fig. 6.4 Distinction between metastasis and focal nodular hyperplasia, thanks to a liver contrast agent (Gd-EOB-DTPA) by MRI (T_1-weighted FLASH sequence, fast low angle shot) 3D. During the arterial phase of the contrast agent, two hypervascular lesions are visible (*white arrow*) in a patient with a clinical history of breast cancer (**a**). During the hepatospecific phase of Gd-EOB-DTPA (20 min after injection), MRI showed a "wash-out" of the contrast agent in the area indicated by the *white arrow*, corresponding to metastasis. During this same phase, the region indicated by the *black arrow* has captured the contrast agent homogeneously with a better definition of a central scar characteristic of a focal nodular hyperplasia (**b**). The nature of these lesions was confirmed after surgical resection of metastasis and biopsy of the focal nodular hyperplasia. Figure reproduced with permission of Ref. [27]

Gd-BOPTA, liver enhancement is more prolonged and somewhat lower. Once the compound have been excreted into bile, a very strong enhancement of the biliary tree is obtained which allows to consider application of these contrast agents in MRI cholangiography. Gd-BOPTA and Gd-EOB-DTPA are approved for clinical use. In the imaging of biliary tract, a dose of 10 μmol/kg is sufficient. Beyond appears the T_2 effect induced by the high concentration of the contrast agent.

Gd-BOPTA and Gd-EOB-DTPA allow for the detection of primary or secondary liver tumors [21–24]. With hepatic enhancement extended over two hours, it is possible to collect images from several sequences after injection. Furthermore, these two complexes bind to albumin, which causes an increase in relaxivity and provides an interesting property for their use as contrast agent for angiography [25, 26].

A better characterization of hepatocellular lesions such as hepatocellular adenoma or nodular and focal hyperplasia is also permitted. Enhanced lesions in the arterial phase of Gd-EOB-DTPA are identifiable during its hepatospecific phase: in a patient, a focal and nodular hyperplasia appears clearer than metastasis in T_1-weighted MRI [27] (Fig. 6.4).

6.2.2 *Superparamagnetic Iron Oxide Nanoparticles as Specific Agents of Kupffer Cells*

The main agents based on iron oxide nanoparticles known are AMI-25 (Feridex® or Endorem®) [28], SHU555A (Resovist® or Cliavist®) [29] and AMI-227

(Sinerem®) [30]. These particles are made of crystalline iron oxide core, coated with a dextran derivative. The overall size of the particle is determined by the thickness of the dextran layer. After intravenous injection, particles are captured by cells of the reticuloendothelial (mononuclear phagocytic) system (Kupffer cells in the liver, spleen, lymph nodes, bone marrow, lung macrophages) [31, 32].

SPIO have a relatively short plasma half-life (10–15 min in rats, 20–40 min in humans) with an extremely rapid hepatic uptake. The agent persists in Kupffer cells for about seven days, leaving considerable time for imaging acquisition after administration. Gradually, the product is degraded in lysosomes of Kupffer cells and is integrated into the pool of iron in the body.

USPIO particles are smaller with a longer blood half-life (24 h in humans), which allows them to have contrast properties related to their vascular compartmentalization, thus for the study of blood vessels.

The AMI-25 and AMI-227 have high relaxivities r_1 and r_2 (Table 6.2), which allow them to have two possible enhancement effects: increasing signal (T_1 effect) and lowering signal (T_2 effect).

The T_2 effect is predominant with nanoparticles and direct clinical application is the detection of liver tumors [33, 34]. The particles act on the T_2 relaxation by spin-spin interaction. Moreover, the aggregation of particles within the Kupffer cells will create very intense local heterogeneities of magnetic field inducing a dephasing of the protons and a signal loss. It is a phenomenon called magnetic susceptibility (T_2* effect).

In the zones where normal liver Kupffer cells are present, a signal decrease is observed after injection, while a tumor lacking phagocytic activity does not take up the nanoparticles and its signal remains unchanged (Fig. 6.5). The tumor therefore appears bright in a black liver (negative contrast effect) using a T_2-weighted MRI sequence. Because of their relatively high r_1 relaxivity, the SPIO and USPIO are also able to enhance the MRI signal, especially at low concentration and with T_1-weighted sequences. This effect is easily observable on aqueous dilutions of the particles, but in vivo, other physiological phenomena are superimposed, making it more difficult to demonstrate a positive enhancement. [35].

A study showed a positive signal enhancement of the liver was possible in the first five minutes after AMI-227 injection in rats [36]. In humans, such an observation has also been reported at the end of the AMI-227 slow infusion [37] and the enhancement of hepatic hemangiomas after the Endorem® infusion T_1-weighted [38].

Table 6.2 Relaxivity of iron oxide nanoaprticles (37 °C, 1.5 T)

Nanoparticles	Hydrodynamic diameter	Relaxivity ($s^{-1}mM^{-1}$)
AMI-227, Sinerem®, Combidex® (dextran)	17–30 nm	r_1 = 19.5 r_2 = 87.6
AMI-25, Endorem®, Feridex®, Ferumoxides (dextran)	80–150 nm	r_1 = 9.95 r_2 = 158

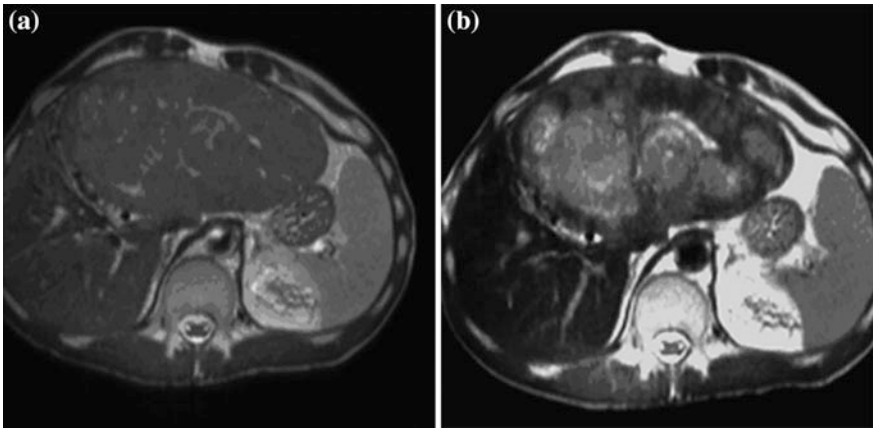

Fig. 6.5 Well differentiated hepatocellular carcinoma in a patient's liver. Axial slice acquired with T_2-weighted turbo spin echo sequence before (**a**) and after (**b**) injection of Endorem®. We can observe in the tumor (**b**) darkened peripheral regions (due to the accumulation of iron oxide nanoparticles in the cells), while the central region remains clear (with permission of Ref. [6])

After Endorem® injection, the liver signal decreases. On a T_1-weighted sequence, the signal of liver becomes close to that of the tumor (most tumors are hypointense on T_1). The contrast is thus decreased. On proton density and T_2-weighted sequences however, the contrast is increased as the lesion appears white in a black liver. The overall image quality is improved and the lesions are more easily discernible. The best sequence after injection seems to be proton density-weighted which is sensitive to the presence of particles and has a sufficiently short TE to obtain a good signal to noise [39] ratio. The injection of Endorem® gives higher sensitivity in the detection of small lesions under 1 cm [40].

6.2.3 Contrast Agents for Lymphatic System

The clinical interest is important: ganglion curettages are made systematically to distinguish inflammatory lymph nodes from metastatic nodes.

Superparamagnetic nanoparticles are captured by different cells of the mononuclear phagocytic system, particularly in lymph nodes. Percentage of nanoparticle captured into the lymph is quite low after intravenous injection, and varies depending on the type of particle. For small particles (AMI-227, Sinerem®) [41], the lymphatic uptake is greater than for AMI-25 (Endorem®) which undergo predominant hepatic uptake.

Several pre-clinical experiments have shown that particles cluster in macrophages of lymph node sinusoids, both in normal or inflammatory lymph nodes with

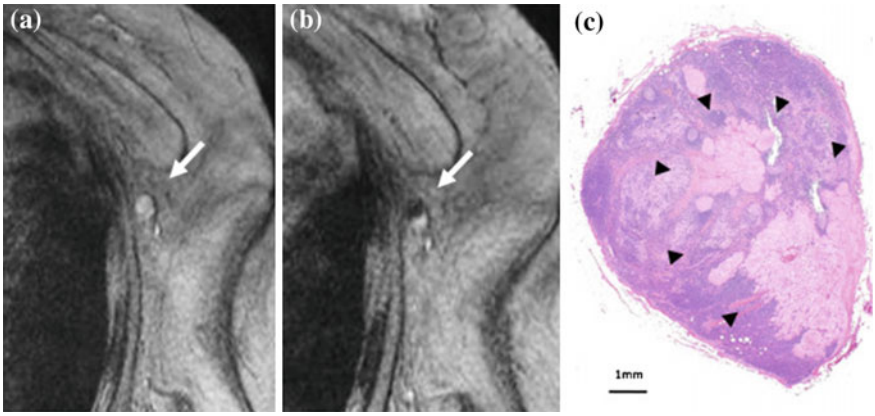

Fig. 6.6 Sentinel lymph node (breast cancer) having a high signal intensity on a portion of more than 50 % after injection of SPIO (T_2* weighted MRI to a magnetic field of 1.5T, gradient echo sequence: TR = 613, TE = 30 ms, 4 mm slice thickness, flip angle 30°, resolution of 1 × 0.65 mm). **a** The axillary lymph node shown by the *arrow* has a high signal intensity before injection of SPIO. **b** Eighteen to twenty-four hours after intradermal injection of SPIO (Resovist®), the node pointed by the arrow is dimmed, but has a hyper-signal zone, diagnosed as malignant. **c** Histology shows the presence of macro-metastasis in the lymph node (*arrowheads*) (Reproduced according to Ref. [45])

T_2 effect as a consequence. In metastatic lymph nodes, tumor is devoid of phagocytic cells and does not capture particles.

The signal may change in tumor-containing node after injection; T_1 effect was found at 1.5T probably due to unclustered particle leakage in the tumor interstitium [42]. Clinical trials in healthy humans (cervical lymph nodes) were also partially completed. The development of such a technique requires: a particle having a high percentage of node capture and imaging technique with high spatial resolution to analyze small nodes [43, 44] (Fig. 6.6).

6.3 Vascular Contrast Agents

Vascular contrast agents have a prolonged time of intravascular persistence allowing imaging of organ perfusion after the first minutes of injection (initial rise of the signal), vascular imaging performed on the plateau phase after initial increase (MRA application), imaging of the capillary permeability of tissues based on the study of contrast agent leakage in the interstitium.

6.3.1 Superparamagnetic Nanoparticles

USPIO nanoparticles (USPIO, AMI-227) have a long plasma half-life (two hours in rats 24 h in humans), a large size and a very high r_1 relaxivity. So they have the properties to be used as contrast agents of the vascular area [44, 46–48]. Using their T_1 or T_2 effect, several experimental studies have shown their application in the imaging of myocardial ischemia [49], renal vasculature [50] and tumor capillary permeability.

6.3.2 Macromolecular Contrast Agents (Albumin-Dextran, Polylysine-Gd-DTPA)

They are composed of a carrier macromolecule (albumin, dextran, polylysine) to which several Gd chelates are covalently attached [51, 52].

6.3.3 Applications

Tumor angiogenesis induced proliferation of hyperpermeable vessels. Indeed, tumors are developing new vessels from existing vasculature. This process of angiogenesis is essential for tumor growth. Tumors can be characterized by measuring perfusion parameters with MRI (reflecting vessel permeability, volume of extra and intravascular compartments). Perfusion imaging is usually performed using a dynamic approach of T_1-weighted imaging after bolus injection of contrast agent (dynamic contrast enhanced MRI). The size of these compounds influences their volume distribution: macromolecular agents do not pass the capillary barrier, have a prolonged blood half-life, and can be used as vascular contrast agents. Contrast agents of average molecular weight (1–60 kDa) and higher molecular weight (>60 kDa) were called blood pool agents due to their prolonged intravascular retention and allow to evaluate the modification tumor vessel permeability. Albumin-$(Gd\text{-}DTPA)_{35}$ is a prototype of contrast agents for the blood compartment (molecular weight 92 kDa). Its use in humans, however, is limited by its immunogenicity. MS-325 (Vasovist®), a Gd chelate reversibly binding to endogenous albumin is currently marketed [53–55]. Particulate contrast agents are another class of blood pool agents. Among them, the USPIO particles (Sinerem®) which have a diameter of 10–50 nm and a molecular weight higher than 100 kDa were particularly studied but never marketed. However, the contrast agents of high molecular weight have the major disadvantage of a very slow kinetic enhancement due to very low rates of extravasation.

Contrast agents of intermediate molecular weight are used to obtain images with good signal to noise ratio in a relatively short time (5–7 min). These agents, such as

Gadomer-17 (invivoContrast) with a molecular weight of 17 kDa and P792 (Vistarem®) with a molecular weight of 6.47 kDa, represent a good compromise between low and high molecular weight agents but cannot be used in human patients [56, 57].

6.4 Conclusions

Nowadays, only Gd chelates are approved and available as MRI contrast agent for clinical use. Approved iron oxide nanoparticles were taken off the market because of lack of sales [58]. However, several types of iron oxide nanoparticles are available for pre-clinical MRI. In contrast media research, compound size as well as their contrast and surface properties can be adapted for optimizing their distribution, circulation time, elimination way and MRI detectability, according to a desired in vivo fate suitable for vascular, tissue, cellular or molecular MRI. Indeed, current research focuses on the development of molecular imaging contrast agents, capable of targeting overexpressed molecular receptors to diagnose or characterize disease and treatment efficiency at an early stage. The main problem is the detection threshold: contrast agents are detectable in the range of millimolar concentrations, which is much higher than the intracellular concentrations of protein or nucleic acid. It is therefore necessary to develop contrast agents with lower detectability threshold. A second difficulty is to find agents that have a good affinity and high specificity for the target. Mimetic peptide sequences (RGD) or polysaccharides (Sialyl Lewis X) have been developed and grafted on Gd complexes or iron oxide nanoparticles. The identification of sequences having a high affinity for molecular targets of diagnostic interest can be performed by the systemic evolution of ligands by exponential enrichment (SELEX) method. The aim of this technique is to identify sequences in a library of random oligonucleotides. This method comprises several steps including the incubation of ribonucleic (RNA) or deoxyribonucleic acid (DNA) with the target of interest, the selection of sequences that have bound to the target, the amplification of these sequences by RT-PCR (reverse transcription-polymerase chain reaction) and their transcription in vitro. These selection steps and amplification must be repeated (about 8–15 times) until the RNA/DNA candidates having the strongest affinity for the target are isolated; these candidates called aptamers. The SELEX method was used to generate aptamers directed against target molecules of widely varying structure and size such as nucleic acids, small organic molecules (e.g., ATP) and more complex targets such as membrane receptors or whole cells.

Many laboratories have chosen the phage display technology to select the right vector. This method utilizes a library of phages bearing combinations of all peptides of a given length (generally between 6 and 15 amino acids). Incubation of this library with the target allows for the selection of candidates showing high affinity for the target. The primary structure of the peptide is determined by sequencing the DNA of selected phages. This technique has already led to the selection of specific

peptides, targeting angiogenesis, apoptosis, or atherosclerotic plaques …. These peptides are then linked to contrast agents, forming "molecular imaging" contrast agents. The first tests look very promising [59–63].

References

1. Schuhmann-Giampieri G (1993) Liver contrast media for magnetic resonance imaging. Interrelations between pharmacokinetics and imaging. Invest Radiol 28:753–761
2. Wray D, Porter C (1993) Calcium channel types at the neuromuscular junction. Ann N Y Acad Sci 681:356–367
3. Cacheris WP, Quay SC, Rocklage SM (1990) The relationship between thermodynamics and the toxicity of gadolinium complexes. Magn Reson Imaging 8:467–481
4. Laurent S, Vander Elst L, Copoix F, Muller RN (2001) Stability of MRI paramagnetic contrast media. A proton relaxometric protocol for transmetallation assessment. Invest Radiol 36:115–122
5. Goldstein HA, Kashanian FK, Blumetti RF, Holyoak WL, Hugo FP, Blumenfield DM (1990) Safety assessment of gadopentetate dimeglumine in US clinical trials. Radiology 174:17–23
6. Laurent S, Boutry S, Vander Elst L, Muller RN (2016) Produit de constraste pour l'IRM (under press)
7. Collidge TA, Thomson PC, Mark PB, Traynor JP, Jardine AG, Morris ST et al (2007) Gadolinium-enhanced MR imaging and nephrogenic systemic fibrosis: retrospective study of a renal replacement therapy cohort. Radiology 245:168–175
8. Sadowski EA, Bennett LK, Chan MR, Wentland AL, Garrett AL, Garrett RW et al (2007) Nephrogenic systemic fibrosis: risk factors and incidence estimation. Radiology 243:148–157
9. Broome DR, Girguis MS, Baron PW, Cottrell AC, Kjellin I, Kirk GA (2007) Gadodiamide-associated nephrogenic systemic fibrosis: why radiologists should be concerned. AJR Am J Roentgenol 188:586–592 (Comment in: AJR Am J Roentgenol 2007; 188: W580, AJR Am J Roentgenol 2007; 188:W582; AJR Am J Roentgenol 2007; 188:W584. AJR Am J Roentgenol 2007; 189:W169)
10. Kuo PH, Kanal E, Abu-Alfa AK, Cowper SE (2007) Gadolinium-based MR contrast agents and nephrogenic systemic fibrosis. Radiology 242:647–649
11. Neuwelt EA, Hamilton BE, Varallyay CG, Rooney WR, Edelman RD, Jacobs PM et al (2009) Ultrasmall superparamagnetic iron oxides (USPIOs): a future alternative magnetic resonance (MR) contrast agent for patients at risk for nephrogenic systemic fibrosis (NSF)? Kidney Int 75:465–474
12. Thomsen HS (2006) Nephrogenic systemic fibrosis: a serious late adverse reaction to gadodiamide. Eur Radiol 16:2619–2621
13. Perez-Rodriguez J, Lai S, Ehst BD, Fine DM, Bluemke DA (2009) Nephrogenic systemic fibrosis: incidence, associations, and effect of risk factor assessment–report of 33 cases. Radiology 250:371–377
14. Bongartz G, Weishaupt D, Mayr M (2008) Nouveaux problèmes avec les produits de contraste dans l'insuffisance rénale: fibrose systémique néphrogène due au gadolinium. Forum Med Suisse 8:116–122
15. Siauve N, Clément O (2007) Apport des produits de contraste en IRM pour le diagnostic et le suivi thérapeutique en cancérologie. Bull Cancer 94:139–146
16. Morana G, Salviato E, Guarise A (2007) Contrast agents for hepatic MRI. Cancer Imaging 7 (Suppl. A):S24–SS7
17. Van Montfoort JE, Stieger B, Meijer DK, Weinmann HJ, Meier PJ, Fattinger KE (1999) Hepatic uptake of the magnetic resonance imaging contrast agent gadoxetate by the organic anion transporting polypeptide Oatp1. J Pharmacol Exp Ther 290:153–157

18. Reimer P, Schneider G, Schima W (2004) Hepatobiliary contrast agents for contrast-enhanced MRI of the liver: properties, clinical development and applications. Eur Radiol 14:559–578
19. Bellin MF, Webb JA, Van Der Molen AJ, Thomsen HS, Morcos SK (2005) Safety of MR liver specific contrast media. Eur Radiol 15:1607–1614
20. Clement O, Muhler A, Vexler V, Kuwatsuru R, Berthezéne Y, Rosenau W et al (1993) Comparison of Gd-EOB-DTPA and Gd-DTPA for contrast enhanced MR imaging of liver tumors. J Magn Reson Imaging 3:71–77
21. Zech CJ, Grazioli L, Breuer J, Reiser MF, Schoenberg SO (2008) Diagnostic performance and description of morphological features of focal nodular hyperplasia in Gd-EOB-DTPA-enhanced liver magnetic resonance imaging: results of a multicenter trial. Invest Radiol 43:504–511
22. Tsuda N, Okada M, Murakami T (2007) Potential of gadolinium-ethoxybenzyl-diethylenetriamine pentaacetic acid (Gd-EOB-DTPA) for differential diagnosis of nonalcoholic steatohepatitis and fatty liver in rats using magnetic resonance imaging. Invest Radiol 42:242–247
23. Döhr O, Hofmeister R, Treher M, Schweinfurth H (2007) Preclinical safety evaluation of Gd-EOB-DTPA (Primovist). Invest Radiol 42:830–841
24. Choi SH, Lee JM, Yu NC, Suh KS, Jang JJ, Kim SH et al (2008) Hepatocellular carcinoma in liver transplantation candidates: detection with gadobenate dimeglumine-enhanced MRI. AJR Am J Roentgenol 191:529–536
25. Kiryu S, Inoue Y, Watanabe M, Izawa K, Shimada M, Tojo A et al (2009) Evaluation of gadoxetate disodium as a contrast agent for mouse liver imaging: comparison with gadobante dimeglumine. Magn Reson Imaging 27:101–107
26. Wyttenbach R, Gianella S, Alerci M, Braghetti A, Cozzi L, Gallino A (2003) Prospective blinded evaluation of Gd-DOTA- versus Gd-BOPTA-enhanced peripheral MR angiography, as compared with digital subtraction angiography. Radiology 227:261–269
27. Ba-Salamah A, Uffmann M, Saini S, Bastati N, Herold C, Schima W (2009) Clinical value of MRI liver-specific contrast agents: A tailored examination for a confident non-invasive diagnosis of focal liver lesions. Eur Radiol 19:342–357
28. Groman EV, Josephson L, Lewis JM (1989) US Patent, 4827945
29. Bremer C, Allkemper T (1999) Bä rmig J., Reimer P. RES-specific imaging of the liver and spleen with iron oxide particles designed for blood pool MR-angiography. J Magn Reson Imaging 10:461–467
30. Jung CW, Jacobs P (1995) Physical and chemical properties of superparamagnetic iron oxide MR contrast agents: ferumoxides, ferumoxtran, ferumoxsil. Magn Reson Imaging 13: 661–674
31. Bangard C, Stippel DL, Berg F, Kasper HU, Hellmich M, Fischer JH et al (2008) Conspicuity of zones of ablation after radiofrequency ablation in porcine livers: comparison of an extracellular and an SPIO contrast agent. J Magn Reson Imaging 28:263–270
32. Ma HL, Xu YF, Qi XR, Maitani Y, Nagai T (2008) Superparamagnetic iron oxide nanoparticles stabilized by alginate: pharmacokinetics, tissue distribution, and applications in detecting liver cancers. Int J Pharm 354:217–226
33. Tanimoto A, Kuribayashi S (2005) Hepatocyte-targeted MR contrast agents: contrast enhanced detection of liver cancer in diffusely damaged liver. Magn Reson Med 4:53–60
34. Yoshikawa T, Mitchell DG, Hirota S, Ohno Y, Oda K, Maeda T et al (2006) Gradient- and spin-echo T2-weighted imaging for SPIO-enhanced detection and characterization of focal liver lesions. J Magn Reson Imaging 23:712–719
35. Frija G, Clement O, De Kerviler E (1994) Overview of contrast enhancement with iron oxides. Invest Radiol 29(suppl2):S75–S77
36. Oswald P, Clement O, Chambon C, Schouman-Claeys E, Frija G (1997) Liver positive enhancement after injection of superparamagnetic nanoparticles: respective role of circulating and uptaken particles. Magn Reson Imaging 15:1025–1031

37. Small WC, Nelson RC, Bernadino ME (1993) Dual contrast enhancement of both T1 and T2-weighted sequences using ultrasmall superparamagnetic iron oxide. Magn Reson Imaging 11:645–654
38. Trillaud H, Grenier N, Degreze P, Louail C, Chambon C, Franconi JM (1993) First pass evaluation of renal perfusion with Turbo Flash MR imaging and superparamagnetic iron oxide particles. J Magn Reson Imaging 3:83–91
39. Yamamoto H, Yamashita Y, Yoshimatsu S, Baba Y, Hatanaka Y, Murakami R et al (1995) Hepatocellular carcinoma in cirrhotic livers: detection with unenhanced and iron oxide-enhanced MR imaging. Radiology 195:106–112
40. Stoupis C, Ros PR, Gauger J, Torres GM (1993) Superparamagnetic iron oxide enhanced MR imaging vs CT arterial portography in detection of liver masses. In: Proceedings of SMRM 12th annual scientific meeting. Society of Magnetic Resonance in Medicine, New York, p 336
41. Pouliquen D, Le jeune JJ, Perdrisot R, Ermiras A, Jallet P (1991) Iron oxide nanoparticules for use as an MRI contrast agent: pharmacokinetics and metabolism. Magn Reson Imaging 9:275–283
42. Guimaraes R, Clement O, Bittoun J, Carnot F, Frija G (1994) MR lymphography with superparamagnetic iron nanoparticles in rats: pathologic basis for contrast enhancement. AJR Am J Roentgenol 162:201–207
43. Baghi M, Mack MG, Wagenblast J, Hambek M, Rieger J, Bisdas S et al (2007) Iron oxide particle-enhanced magnetic resonance imaging for detection of benign lymph nodes in the head and neck: how reliable are the results? Anticancer Res 27(5B):3571–3575
44. Barentsz JO, Fütterer JJ, Takahashi S (2007) Use of ultrasmall superparamagnetic iron oxide in lymph node MR imaging in prostate cancer patients. Eur J Radiol 63:369–372
45. Motomura K, Izumi T, Tateishi S, Sumino H, Noguchi A, Horinouchi T, Nakanishi K (2013) Correlation between the area of high-signal intensity on SPIO-enhanced MR imaging and the pathologic size of sentinel node metastases in breast cancer patients with positive sentinel nodes. BMC Med Imaging 13:32
46. Rockall AG, Sohaib SA, Harisinghani MG, Babar SA, Singh N, Jeyarajah AR et al (2005) Diagnostic performance of nanoparticle-enhanced magnetic resonance imaging in the diagnosis of lymph node metastases in patients with endometrial and cervical cancer. J Clin Oncol 23:2813–2821. Erratum in J Clin Oncol 23:4808
47. Schneider G, Prince MR, Meaney JF, Ho VB (2005) Magnetic resonance angiography—techniques, indications and practical applications. Springer, New York
48. Persigehl T, Matuszewski L, Kessler T, Wall A, Meier N, Ebert W et al (2007) Prediction of antiangiogenic treatment efficacy by iron oxide enhanced parametric magnetic resonance imaging. Invest Radiol 42:791–796
49. Persigehl T, Bieker R, Matuszewski L, Wall A, Kessler T, Kooijman H et al (2007) Antiangiogenic tumor treatment: early noninvasive monitoring with USPIO-enhanced MR imaging in mice. Radiology 244:449–456
50. Canet E, Revel D, Forrat R, Baldy-Porchet C, De Lorgeril M, Sebbag L et al (1993) Superparamagnetic iron oxide particles and positive enhancement for myocardial perfusion studies assessed by subsecond T_1-weighted MRI. Magn Reson Imaging 11:1139–1145
51. Cyran CC, Fu Y, Raatschen HJ, Rogut V, Chaopathomkul B, Shames DM et al (2008) New macromolecular polymeric MRI contrast agents for application in the differentiation of cancer from benign soft tissues. J Magn Reson Imaging 27:581–589
52. Su MY, Mühler A, Lao X, Nalcioglu O (1998) Tumor characterization with dynamic contrast-enhanced MRI using MR contrast agents of various molecular weights. Magn Reson Med 39:259–269
53. Caravan P, Cloutier NJ, Greenfield MT, McDermid SA, Dunham SU, Bulte JW et al (2002) The interaction of MS-325 with human serum albumin and its effect on proton relaxation rates. J Am Chem Soc 124:3152–3162
54. McMurry TJ, Parmelee DJ, Sajiki H, Scott DM, Ouellet HS, Walovitch RC et al (2002) The effect of a phosphodiester linking group on albumin binding. Blood half-life, and relaxivity of

intravascular diethylenetriaminepentaacetato aquo gadolinium(III) MRI contrast agents. J Med Chem 45:3465–3474
55. Farooki A, Narra V, Brown J (2004) Gadofosveset EPIX/schering. Curr Opin Investig Drugs 5:967–976
56. Mandry D, Pedersen M, Odile F et al (2005) Renal functional contrast-enhanced magnetic resonance imaging; Evaluation of a new rapidclearance blood pool agent (P792) in Sprague-Dawley rats. Invest Radiol 40:295–305
57. Baudelet C, Cron GO, Gallez B (2006) Determination of the maturity and functionality of tumor vasculature by MRI: correlation between BOLD-MRI and DCE-MRI using P792 in experimental fibrosarcoma tumors. Magn Reson Med 56:1041–1049
58. Bulte JWM (2009) In vivo MRI cell tracking: clinical studies. AJR Am J Roentgenol 193 (2):314–325
59. Larbanoix L, Burtea C, Laurent S et al (2010) Potential amyloid plaque-specific peptides for the diagnosis of Alzheimer's disease. Neurobiol. Aging Neurobiol. Aging 31(10):1679–1689
60. Burtea C, Laurent S, Mahieu I et al (2011) In vitro biomedical applications of functionalized iron oxide nanoparticles, including those not related to magnetic properties. Contrast Med. Mol. Imaging 6:236–250
61. Larbanoix L, Burtea C, Ansciaux E et al (2011) Design and evaluation of a 6-mer amyloid-beta protein derived phage display library for molecular targeting of amyloid plaques in Alzheimer's disease. Comparison with two cyclic heptapeptides derived from a randomized phage display library. Peptides 32(6):1232–1243
62. Burtea C, Ballet S, Laurent S et al (2012) Development of a magnetic resonance imaging protocol for the characterization of atherosclerotic plaque by using vascular cell adhesion molecule-1 and apoptosis-targeted ultrasmall superparamagnetic iron oxide derivatives. Arterioscler Thromb Vasc Biol 32(6):e36–e48
63. Sclavons C, Boutry S, Laurent S et al (2015) Targeting of cell death and neuroinflammation with peptide-linked iron oxide nanoparticles and Gd-DTPA in a mouse model of Parkinson's disease (accepted)